Design and Study of a Free-Space Quasi-Optical Measurement System
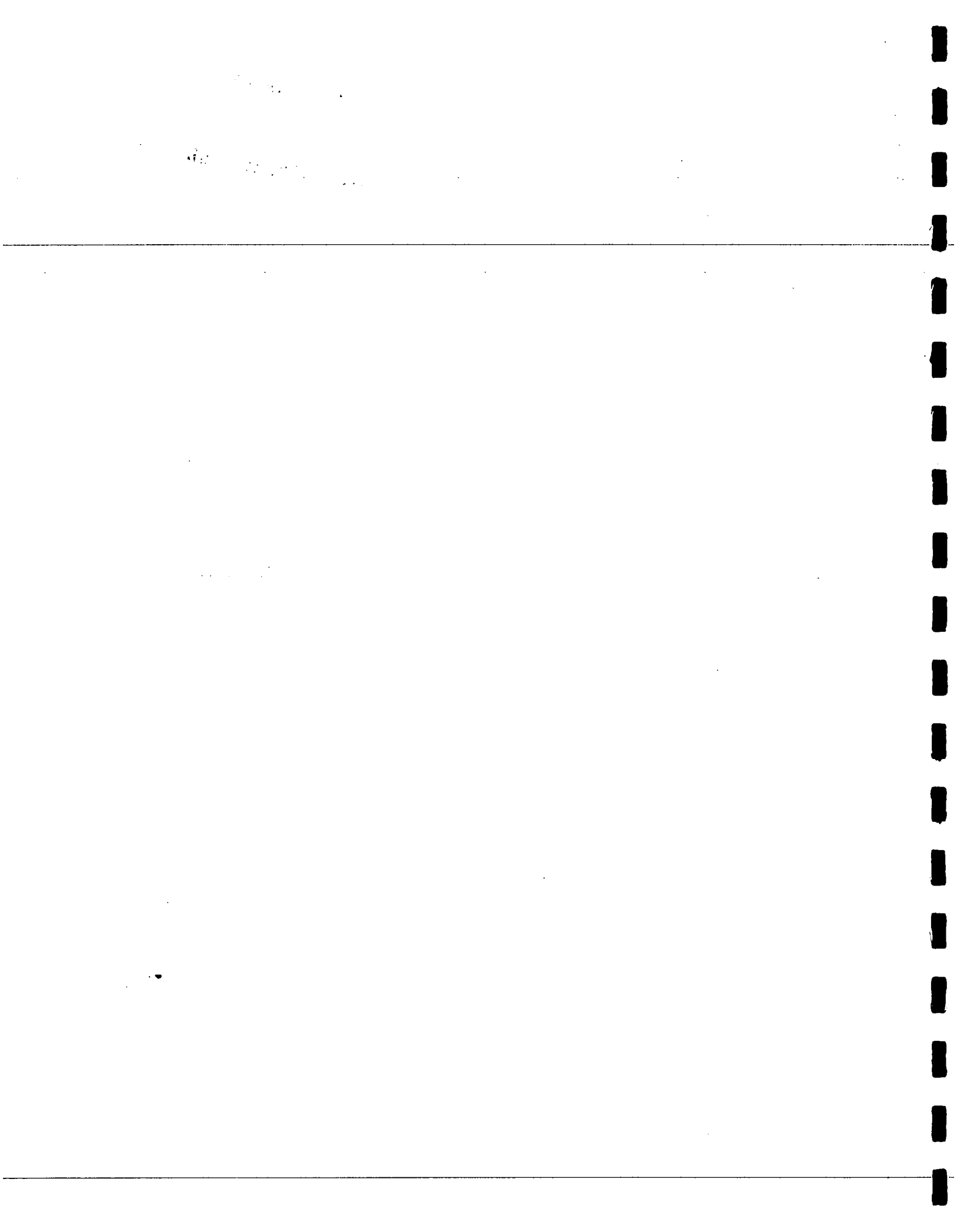
Nicolas Gagnon

CRC

Design and Study of a Free-Space Quasi-Optical Measurement System

Nicolas Gagnon

CRC Report No. CRC-RP-2002-02
Ottawa, July 2002

CAUTION
This information is provided with
the express understanding that
proprietary and patent rights will
be protected

ABSTRACT

This document describes a free-space quasi-optical measurement system designed to characterise dielectric materials at Ka band. The measurement system consists of a pair of colinear horn-fed lenses between which the sample under test is inserted. A study is performed in order to determine the sensitivity of the structure to misalignments, which reveals that care must be taken to ensure constant exact positioning of the components of the measurement system. Reflection and transmission coefficients (S-parameters) of the sample are obtained using a two-port vector network analyser connected to the feed horns. Calibration of the system is performed using a free-space through-reflect-match (TRM) technique, which is preferred over other calibration techniques because it does not require the movement of any component of the system during the calibration process.

Correction terms must be applied to the reflection and transmission coefficients because of errors due to the misplacement of the sample and the calibration procedure. The sample's dielectric constant is then extracted from the corrected reflection and transmission coefficients using one of two different numerical techniques: a root-finding algorithm and a genetic algorithm. Results obtained with both extraction techniques were found to be similar. Moreover, these results are in good agreement with published manufacturer data and with measurements performed by an independent organisation using a resonance technique.

This work demonstrates the feasibility of a low-cost, functional and flexible quasi-optical measurement system for characterising dielectric materials at Ka band.

RÉSUMÉ

Le présent document décrit un système de mesure quasi-optique dans l'espace libre conçu pour caractériser des matériaux diélectriques dans la bande Ka. Le système de mesure est constitué d'une paire de lentilles colinéaires, alimentées par des antennes-cornets, entre lesquelles l'échantillon à caractériser est inséré. Une étude a été réalisée pour déterminer la sensibilité de la structure due aux erreurs d'alignement. Cette étude a démontré qu'un positionnement constant des composantes du système de mesure est nécessaire pour obtenir des résultats adéquats. Les coefficients de réflexion et de transmission (paramètres S) de l'échantillon sont obtenus en connectant les antennes-cornets à chacun des deux ports d'un analyseur de réseau. Le système est calibré en utilisant une technique de calibrage de type TRM (*through-reflect-match*) dans l'espace libre. Cette technique est choisie car, contrairement à d'autres techniques, elle ne nécessite pas le déplacement des composantes du système durant le calibrage.

Des coefficients de correction doivent être appliqués aux paramètres S pour éliminer les erreurs d'alignement et de calibrage. La constante diélectrique est ensuite obtenue à partir des paramètres S corrigés en utilisant un algorithme numérique pour trouver la racine d'une equation ou un algorithme génétique. Les résultats obtenus avec ces deux techniques d'extraction sont similaires. De plus, ces résultats concordent avec les données des manufacturiers et avec des mesures effectués par un organisme indépendant en utilisant une technique de résonance.

Ce travail démontre la faisabilité d'un système de mesure quasi-optique peu coûteux, versatile et fonctionnel pour caractériser des matériaux dans la bande Ka.

FOREWORD

The work presented in this document is based on a Master's thesis[1] submitted at the University of Ottawa in May 2002.

---

[1] N. Gagnon, "Design and Study of a Free-Space Quasi-Optical Measurement System," Master's thesis, School of Information Technology and Engineering, University of Ottawa, Ottawa, Canada, May 2002.

TABLE OF CONTENTS

LIST OF FIGURES

LIST OF TABLES

LIST OF SYMBOLS

a	longest dimension of the aperture of a pyramidal horn
a_l	waveguide longest dimension
b	smallest dimension of the aperture of a pyramidal horn
b_l	waveguide smallest dimension
c	field coupling coefficient
C	length of a pyramidal horn
d	waist-to-aperture distance in a pyramidal horn
d_e	waist-to-aperture distance in a pyramidal horn (E-plane)
d_h	waist-to-aperture distance in a pyramidal horn (H-plane)
D	diameter of a lens
e	natural number
$\mathbf{E}$	electric field (vector)
f	focal length
F_e	fractional power
G	magnitude of the reflection coefficient
H	extension height of a pyramidal horn (in the E-plane)
$\mathbf{H}$	magnetic field (vector)
j	imaginary number
k_0	free-space wave number
K	power coupling factor
L	extension length of a pyramidal horn
m_0	free-electron mass
m_e	electron mass
m_p	hole mass
n	integer
N	dopant density
p	apex-to-aperture distance in a pyramidal horn
p_e	apex-to-aperture distance in a pyramidal horn in the E-plane
p_h	apex-to-aperture distance in a pyramidal horn in the H-plane

q	electronic charge
r	cylindrical coordinate
r_e	radius
R	radius of curvature
S	matrix of scattering parameters (usually in brackets)
S_{11}	forward reflection coefficient
S_{12}	reverse transmission coefficient
S_{21}	forward transmission coefficient
S_{22}	reverse reflection coefficient
t	thickness
T	thickness of a lens
T_e	edge taper
T_S	transmission coefficient
u	complex function defining a propagating wave and/or Gaussian beam distribution
w	beam radius
w_0	beam waist radius
w_{in}	input beam waist radius
w_{out}	output beam waist radius
W	extension width of a pyramidal horn (in the H-plane)
x	rectangular coordinate
y	rectangular coordinate
z	rectangular or cylindrical coordinate
Z_A	wave impedance in free space
Z_S	wave impedance in the slab
α_0	attenuation constant in free space
α_e	flare angle of a pyramidal horn in the E-plane
α_h	flare angle of a pyramidal horn in the H-plane
β_0	phase constant in free space
γ_0	propagation constant in free space
γ_S	propagation constant in the slab
Γ	reflection coefficient at the air-sample interface

Γ_S	reflection coefficient of a slab
δ	axial offset of a sample with respect to the plane wave location
Δ	distance between constant phase surface and beam waist location
Δ_e	distance between constant phase surface and beam waist location in the E-plane
Δ_h	distance between constant phase surface and beam waist location in the H-plane
Δx	transverse offset in x
Δy	transverse offset in y
Δz	axial offset (in z)
$\Delta \theta$	phase shift introduced by a focusing lens
$\Delta \varphi$	phase shift introduced by tilting a beam
ε	permittivity
ε_0	permittivity in free space
ε_p	unperturbed relative permittivity of silicon
ε_r	dielectric constant or relative permittivity
θ	radiation angle
θ_0	asymptotic beam growth angle
θ_{xz}	tilt in the xz plane (yaw)
θ_{yz}	tilt in the yz plane (pitch)
λ_0	free-space wavelength
λ_S	guided wavelength in the slab
μ	permeability
μ_0	permeability in free space
μ_e	electron mobility
μ_h	hole mobility
μ_r	relative permeability
ρ	slant length of a pyramidal horn
ρ_e	slant length of a pyramidal horn in the E-plane
ρ_h	slant length of a pyramidal horn in the H-plane
σ	phase of the transmission coefficient
τ	transmission coefficient in the material sample of finite thickness
τ_e	electron collision time

τ_h hole collision time

φ phase (with subscript)

φ_0 Gaussian beam phase shift

ψ scalar field

ω angular frequency

CHAPTER 1 Introduction

1.1 Background

With the severe congestion of the electromagnetic spectrum at microwave frequencies, communications systems are increasingly being developed at higher frequencies, mainly at millimetre and sub-millimetre wavelengths (above 30 GHz). New broadband communications systems including Local Multipoint Communication Systems (LMCS) [1], Local Multipoint Distribution Services (LMDS) [2, 3] and multimedia satellite services [4] have already been assigned to the Ka band. These systems will be used to provide wireless high-speed internet access, videoconferencing, interactive entertainment and other applications requiring large bandwidth. Since these systems are intended for both mobile and fixed terminals, low-profile antennas are desired. Moreover, some user terminals may also be used for communications with satellites, which will require high-gain antennas and electronic beam-steering capabilities.

Traditionally, conventional reflector antennas have been used for satellite communications as they are low-cost and offer high gain. However, in the case of mobile terminals, such antennas are quite large and do not provide electronic beam-steering capabilities. On the other hand, planar active phased array antennas are low-profile and capable of steering their beam electronically. Their major drawback is that a complex feed network made of a significant number of phase shifters and attenuators is needed to obtain good flexibility, which translates to increased overall cost.

As an alternative to achieving high-gain, low-profile, electronically steerable antennas, optically-induced antennas have been proposed [5-7]. This new concept

1

introduces optical illumination of a low-profile structure, such as a frequency selective surface or a reflectarray. The low-profile structure consists of a semiconductor slab which, when illuminated by an optical source, becomes conductive. By controlling the illumination, the optically-induced conductivity pattern can be modified, and can be used to either shape the radiation pattern of the beam or provide beam steering. The optically-induced array configuration is potentially less complex than an active phased array as it needs fewer components.

1.2 Motivation

The design of planar optically-induced antennas first requires an accurate knowledge of the properties of the materials. In particular, semiconductor materials, such as silicon and gallium arsenide, have to be investigated with and without illumination. Many material characterisation techniques are available, but not all of them allow for optical illumination, contactless measurement and the capability to measure materials with either high- or low-loss. These criteria are crucial in the present situation. Furthermore, the measurement system to be used must operate in the frequency range of interest, offer a reasonable accuracy and be relatively low-cost.

1.3 Thesis Objectives

The main objective of this thesis is to design and fabricate an accurate and versatile measurement system to be used to characterise optically-sensitive materials at Ka band. To achieve this goal, many steps must be completed.

First, a review of the various types of measurement systems is to be performed so that a suitable candidate may be chosen. A free-space transmission/reflection quasi-optical configuration has been selected.

Second, the quasi-optical measurement system is to be designed and fabricated for sample characterisation at Ka band. This entails the proper choice and/or design of quasi-optical components.

Third, the evaluation of the measurement system's performance is to be performed by studying the effects of manufacturing tolerance errors and component misalignment errors.

Fourth, given that any measurement requires prior calibration of the system, an appropriate calibration technique is to be determined. Furthermore, an efficient and stable procedure is to be developed for extracting the dielectric constants from the measured data.

Finally, the accuracy of the measurement setup is to be evaluated by measuring various samples of known dielectric constant.

1.4 Thesis Contribution

The main interest of the proposed measurement system is that it is designed with limited cost due to the use of pyramidal horns and millimetre-precision mechanical equipment.

Investigation of misalignments in such an apparatus has not been reported before. To perform this analysis, a theoretical formulation incorporating occurrence of simultaneous misalignments is developed.

The determination process uses correction terms to compensate for possible misplacement of the sample under test and errors due to the calibration. Additionally, the extraction techniques described in this thesis, which are used to convert recorded data into material parameters, use a numerical approach, including a novel approach based on a genetic algorithm.

1.5 Thesis Organisation

The second chapter reviews the relevant theory of quasi-optics required for the design of the measurement system. This theory is then used in the following chapters for the design and analysis of the measurement system.

The third chapter presents a review of the various types of measurement systems as well as the description and design of the selected candidate (free-space transmission/reflection quasi-optical configuration). In particular, the design of the measurement system components is reported. Furthermore, the measurement technique and calibration process are described.

The fourth chapter focuses on one of the main problems of the measurement system: the misalignment of the components. A theoretical treatment of the occurrence of simultaneous misalignments is given. Experimental and theoretical results are reported.

The fifth chapter presents the determination of the dielectric properties of materials. In particular, this chapter presents the general manipulations to be performed on the recorded data before using it in the extraction process. These manipulations include data smoothing and corrections due to misplacement of the sample and calibration. This

chapter also describes the theory required in order to extract dielectric properties of material, as well as extraction techniques.

The last chapter summarises the work, provides a general conclusion and describes future work to be performed.

CHAPTER 2 Quasi-Optics Theory

2.1 Introduction

This chapter presents quasi-optics theory and the required background to fully understand the design and study of a quasi-optical test bench. Gaussian beams are one of the fundamental elements of quasi-optics. This chapter describes the propagation, launching and transformation of Gaussian beams which are used to design the measurement system. Gaussian beam coupling, which is used in the study of the misalignment of the components of the measurement system, is also presented.

2.2 Quasi-Optics Basics

2.2.1 Definition of Quasi-Optics

Quasi-optics is the study of the free-space propagation of a beam which is fairly well collimated but has transverse dimensions of the order of a wavelength [8]. Because the wavelength is not small with respect to the size of the beam and the system dimensions, diffraction effects have to be considered [8]. From antenna theory, increasing the aperture of the radiating component would make the beam narrower and reduce diffraction; however this would increase the overall size of the system, which is not desired.

At microwave, millimetre wave and sub-millimetre wave frequencies, Maxwell's equations are normally used to describe electromagnetic propagation. At these frequencies, it is difficult to obtain a narrow enough beam so that one can apply geometrical optics and neglect diffraction. This is only possible for a wavelength of about 1 μm, which corresponds to the visible spectrum or light. However, if the beam launched

7

by the radiating device is fairly well collimated and characterised by a Gaussian amplitude distribution, Gaussian optics can be applied [9]. Gaussian optics satisfies Maxwell's equations, in which the beams are solutions to Maxwell's equations under paraxial approximation. This is a very attractive solution since Gaussian optics is simple and elegant compared to Maxwell's equations. Furthermore, Gaussian beams can easily be launched by common radiating devices like feed horns.

2.2.2 Interest of Quasi-Optics

At microwave frequencies and lower, wave-guiding structures are required to contain the energy of a propagating wave, otherwise the amount of diffraction causes the energy to disperse quickly with distance [10]. The guiding structures used at these frequencies, namely coaxial cables, printed transmission lines and waveguides, all contain metal and, in most cases, dielectric materials. As the frequency increases, the surface resistivity of metal and the loss tangent of dielectric materials increase, resulting in higher losses in the system. Therefore, one may take advantage of free space in order to achieve transmission at millimetre and sub-millimetre wavelengths. By propagating a beam having a low dispersion in free space, and using guiding elements such as lenses, a system similar to those used in optics can be designed. For that reason, quasi-optical systems fill a gap between traditional guiding structures at microwave or millimetre wavelengths and optical systems.

2.3 Gaussian Beam Propagation

2.3.1 Paraxial Wave Equation

Any wave propagation problem in a uniform medium can be described using the homogeneous Helmoltz equation [8, 11]. In free space:

$$\nabla^2 \psi + k_0{}^2 \psi = 0 , \tag{2-1}$$

where ψ represents any scalar field or, in other words, any component of **E**, the electric field, or **H**, the magnetic field. k_0 is the free-space wave number and is equal to

$$k_0 = \frac{2\pi}{\lambda_0} , \tag{2-2}$$

where λ_0 is the free-space wavelength. If we assume the wave is propagating in the positive z direction, then ψ can be written (in rectangular coordinates) as

$$\psi = u(x, y, z) \exp(-jk_0 z), \tag{2-3}$$

where u is a complex function that defines the propagating non-plane wave [8] and the exponential term dictates the phase of a plane wave propagating in the z direction [9]. Expressing (2-1) in rectangular coordinates and substituting (2-3) leads to the following expression:

$$\frac{\partial^2 u}{\partial x^2} + \frac{\partial^2 u}{\partial y^2} + \frac{\partial^2 u}{\partial z^2} - 2jk_0 \frac{\partial u}{\partial z} = 0 . \tag{2-4}$$

According to Goldsmith [8], (2-4) can be simplified based on the following assumptions:

- the variation along the direction of propagation of the magnitude of u is small over a distance of about a wavelength;

- the variation along z of the magnitude of u is small compared to the variation along x and y.

9

From the first statement, we have that

$$\left|\frac{\partial^2 u}{\partial z^2}\right| \ll 2k_0 \left|\frac{\partial u}{\partial z}\right|, \tag{2-5}$$

and from the second statement, we have that

$$\left|\frac{\partial^2 u}{\partial z^2}\right| \ll \left|\frac{\partial^2 u}{\partial x^2}\right|, \left|\frac{\partial^2 u}{\partial y^2}\right|. \tag{2-6}$$

Therefore, the third term in (2-4) can be dropped and we obtain

$$\frac{\partial^2 u}{\partial x^2} + \frac{\partial^2 u}{\partial y^2} - 2jk_0 \frac{\partial u}{\partial z} = 0, \tag{2-7}$$

which is the paraxial wave equation. This is an important result since a solution to (2-7) is simpler than a solution to (2-4). If we convert this result into a cylindrical equation and apply axial symmetry, the following expression is obtained:

$$\frac{\partial^2 u}{\partial r^2} + \frac{1}{r}\frac{\partial u}{\partial r} - 2jk_0 \frac{\partial u}{\partial z} = 0. \tag{2-8}$$

2.3.2 Fundamental Gaussian Beam Mode Propagation

It is known [8] that the simplest solution for u in (2-8) is of the form

$$u(r,z) = \left(\frac{2}{\pi w(z)^2}\right)^{0.5} \exp\left(-\frac{r^2}{w(z)^2} - \frac{j\pi r^2}{\lambda_0 R(z)} + j\phi_0(z)\right), \tag{2-9}$$

where w is the beam radius, R is the radius of curvature and φ_0 is the Gaussian beam phase shift:

$$w(z) = w_0 \left[1 + \left(\frac{\lambda_0 z}{\pi w_0^2}\right)^2\right]^{0.5}, \tag{2-10}$$

$$R(z) = z + \frac{1}{z}\left(\frac{\pi w_0^2}{\lambda_0}\right)^2, \qquad\qquad (2\text{-}11)$$

$$\tan\phi_0(z) = \frac{\lambda_0 z}{\pi w_0^2}. \qquad\qquad (2\text{-}12)$$

The beam radius is defined as the transverse dimension where the power drops to $1/e^2$ with respect to the on-axis power. The beam waist radius, w_0, represents the minimal beam radius. The radius of curvature is defined as the radius of an equiphase surface of a spherical propagating wave. The Gaussian beam phase shift is a phase term that only becomes significant if z is small. The behaviours of the beam radius and the radius of curvature are shown in Figure 2.1.

Inserting (2-9) in (2-3), we obtain

$$\psi(r,z) = \left(\frac{2}{\pi w(z)^2}\right)^{0.5} \exp\left(-\frac{r^2}{w(z)^2} - jk_0 z - \frac{j\pi r^2}{\lambda_0 R(z)} + j\phi_0(z)\right). \qquad\qquad (2\text{-}13)$$
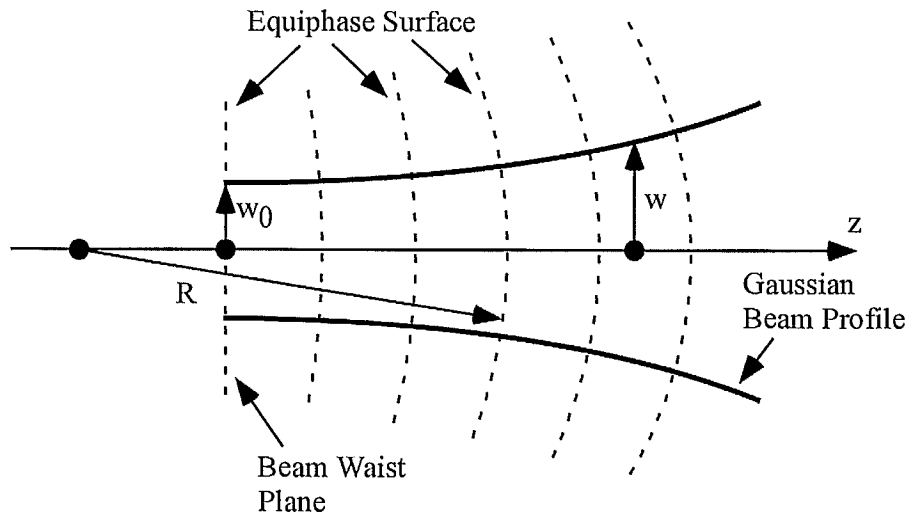
Figure 2.1: Schematic representation of a Gaussian beam propagation.

In (2-13), the first term of the exponential is the Gaussian amplitude distribution, such that:

$$|\psi(r,z)| = |\psi(0,z)| \exp\left(-\frac{r^2}{w(z)^2}\right).$$ (2-14)

For a fixed distance along z:

$$|\psi(r)| = |\psi(0)| \exp\left(-\frac{r^2}{w^2}\right).$$ (2-15)

From (2-15), we find that the transverse distribution is always a Gaussian profile. In this case, only the fundamental mode is represented, which makes the problem simpler. The only term that modifies the distribution is w, the beam radius, which plays the same role as the variance. Referring to (2-13), the second term of the exponential is the phase of a plane wave propagating in the z direction. The third term gives the phase difference between a plane perpendicular to the axis of propagation and the spherical wavefront [9]. The last term is an additional phase term determined by the Gaussian beam phase shift.

Equations (2-10) to (2-15) contain all the necessary information to describe the Gaussian beam propagation. Defining the beam waist location as the distance where the beam radius is minimal, we see that this location occurs at the distance where z is equal to zero. At the same location, the radius of curvature reaches its maximum value as it approaches infinity. Figure 2.2 shows the beam radius as a function of the distance plotted using (2-10) for three different values of beam waist radius. Figure 2.3 shows the radius of curvature as a function of the distance plotted using (2-11), for the three different values of beam waist radius.

Figures 2.4 to 2.12 present the propagation of Gaussian beams for both phase and amplitude as obtained from analytical results. Figure 2.4, Figure 2.5 and Figure 2.6
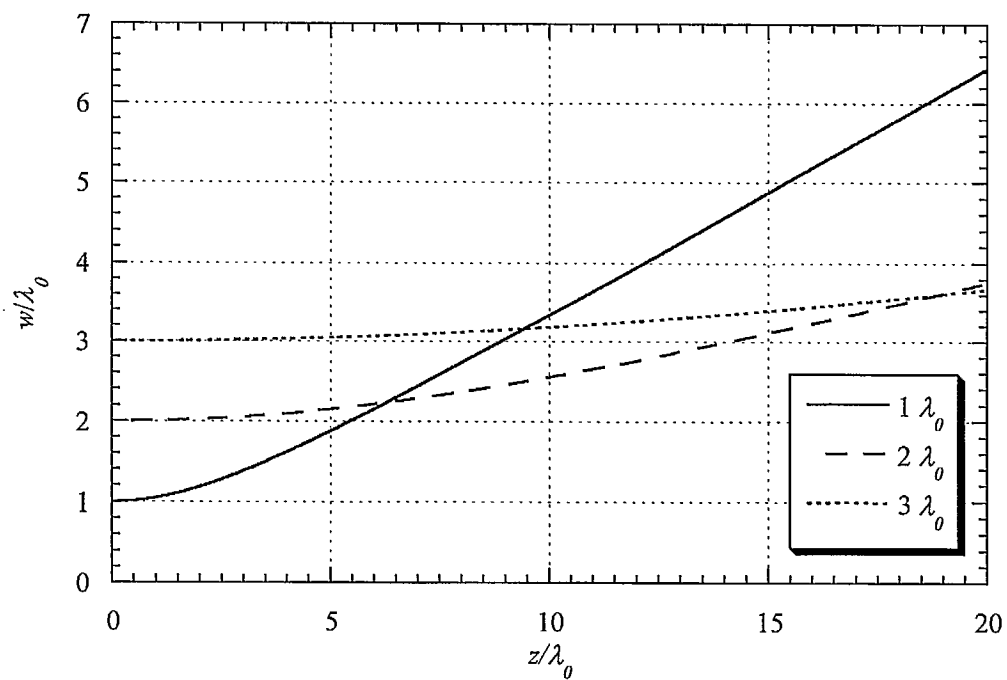
Figure 2.2: Beam radius as a function of distance for different values of beam waist radius.
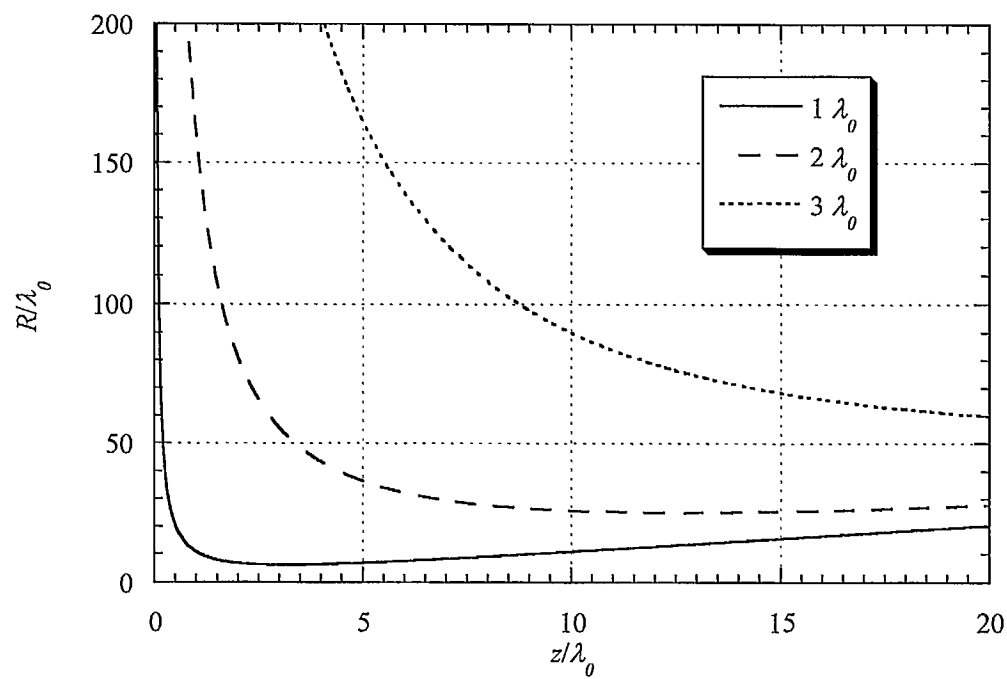
Figure 2.3: Radius of curvature as a function of distance for different values of beam waist radius.

13

respectively show a three-dimensional view of the amplitude, a planar view of the amplitude and a planar view of the phase for a Gaussian beam with a beam waist radius of 1 wavelength. Similarly, Figure 2.7, Figure 2.8 and Figure 2.9 also show a three-dimensional view of the amplitude, a planar view of the amplitude and a planar view of the phase, respectively, for a Gaussian beam with a beam waist radius of 2 wavelengths. Finally, Figure 2.10, Figure 2.11 and Figure 2.12 respectively show a three-dimensional view of the amplitude, a planar view of the amplitude and a planar view of the phase for a Gaussian beam with a beam waist radius of 3 wavelengths.

In Figures 2.4 to 2.12, the amplitude provides information about the beam radius whereas the phase provides information about the radius of curvature. The results obtained are in agreement with Figures 2.2 and 2.3. From all these figures, the following conclusions can be made:

- beams with a smaller beam waist radius diverge more rapidly and are characterised by a wider beam at large distance;

- beams with a smaller beam waist radius have a faster decrease in amplitude;

- beams with a larger beam waist radius offer a more planar wave propagation.

2.3.3 Limitations of Gaussian Beam Propagation

The theory presented in the previous sections does not take into account two important limitations on the propagation model of Gaussian beams. The first limitation is the one that dictates the range of validity of the paraxial equation. In other words, one would like to know if (2-5) and (2-6) can be applied so that (2-7) or (2-8) are valid. As
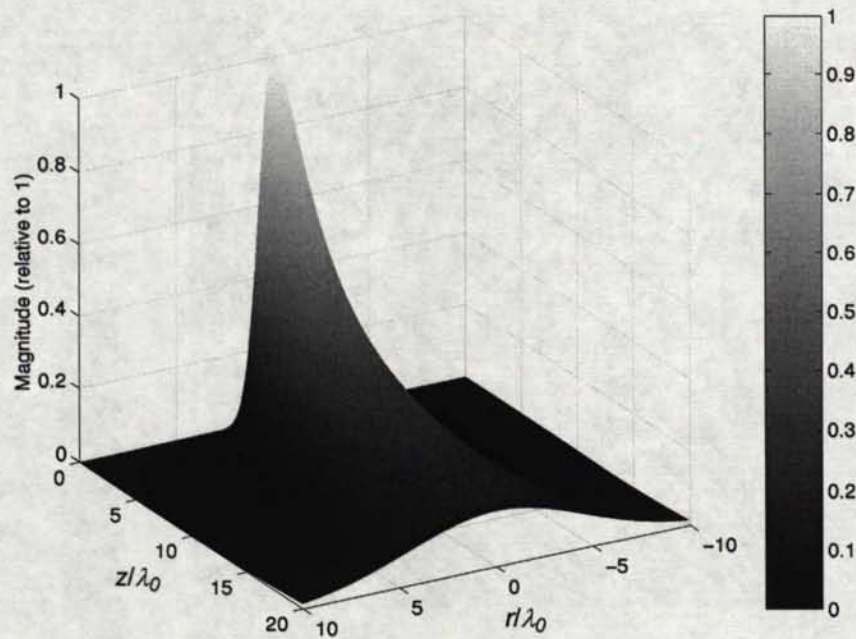
Figure 2.4: Three-dimensional view of the amplitude of a propagating Gaussian beam with beam waist radius of 1 wavelength.
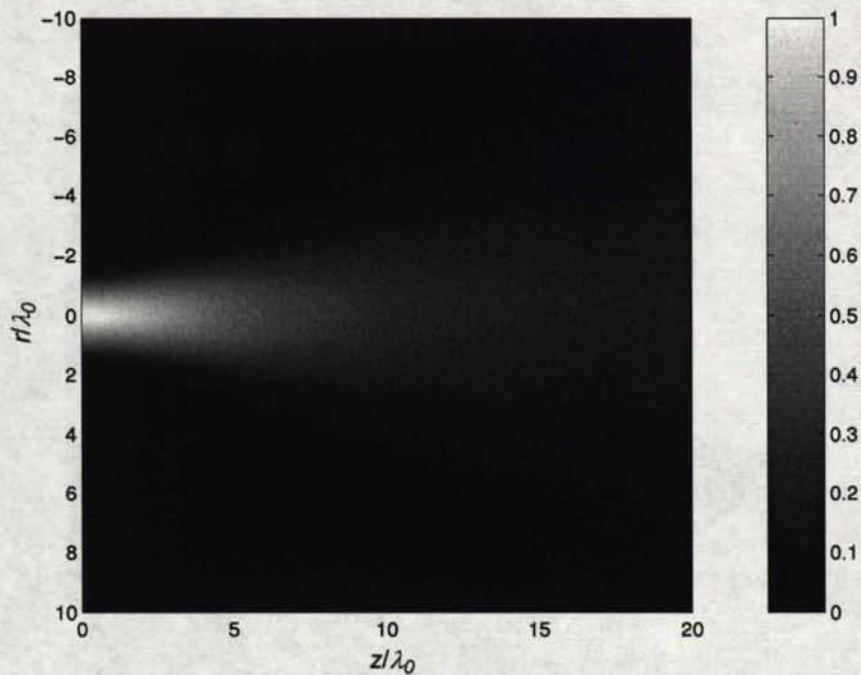
Figure 2.5: Planar view of the amplitude of a propagating Gaussian beam with beam waist radius of 1 wavelength.

15
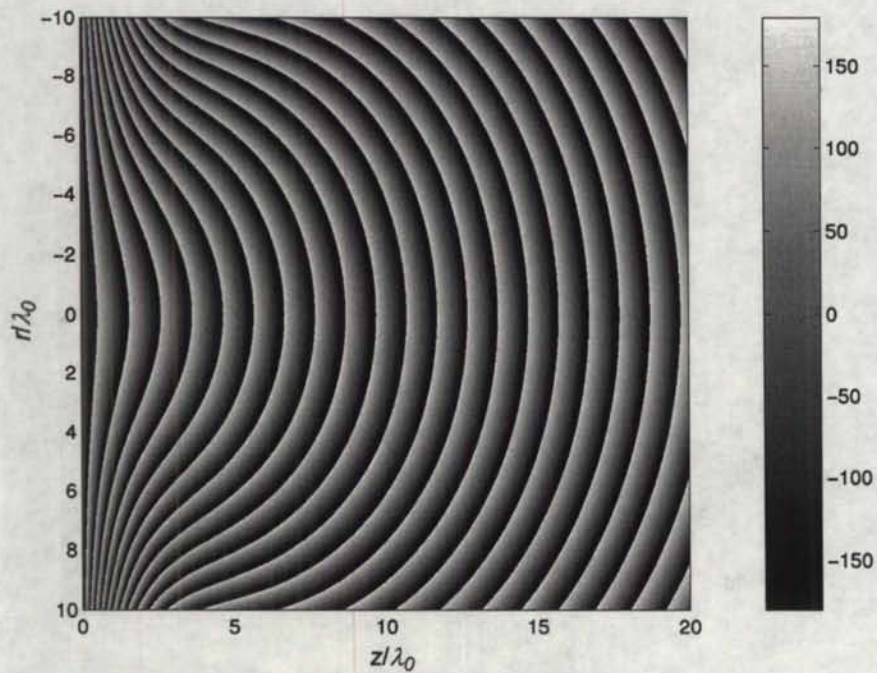
Figure 2.6: Planar view of the phase of a propagating Gaussian beam with beam waist radius of 1 wavelength.
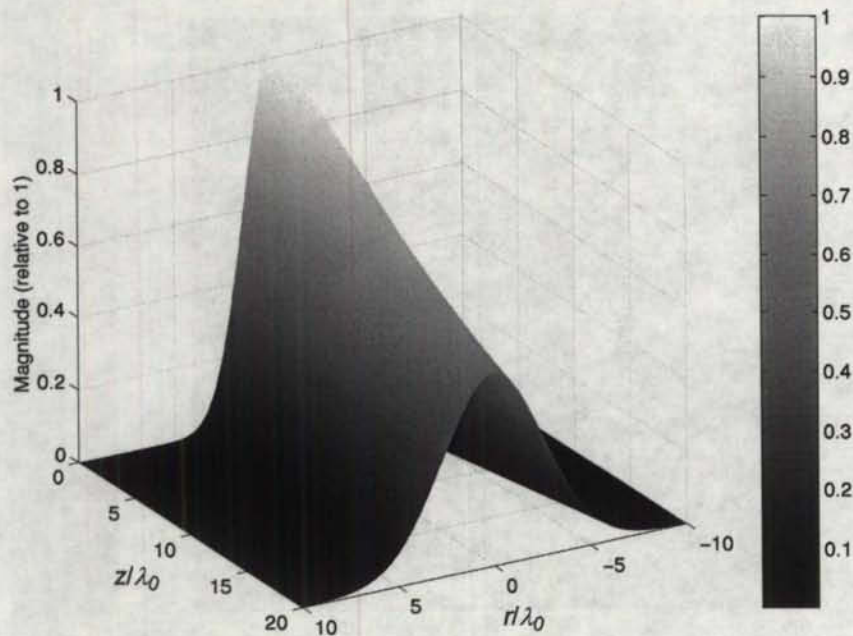
Figure 2.7: Three-dimensional view of the amplitude of a propagating Gaussian beam with beam waist radius of 2 wavelengths.
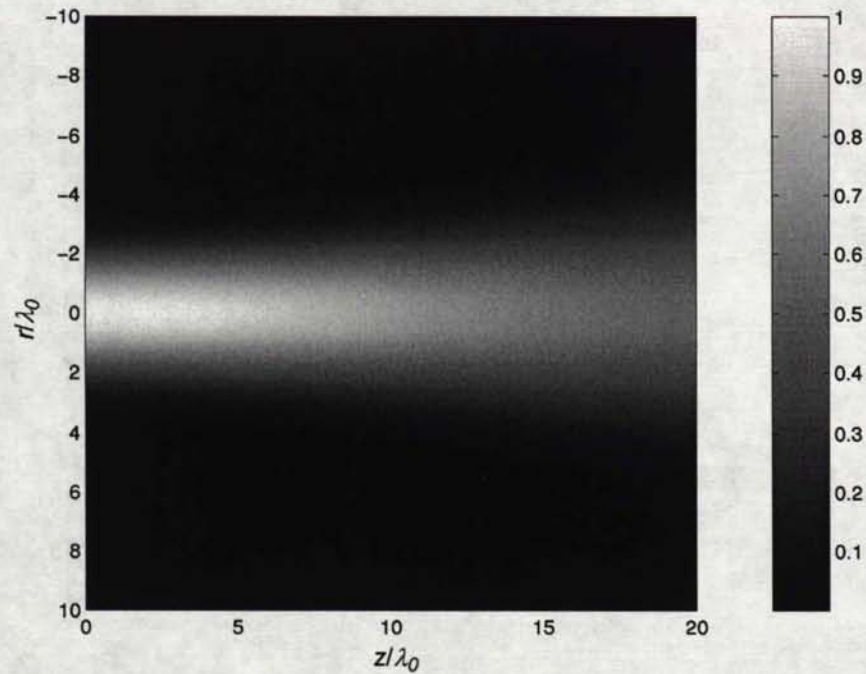
Figure 2.8: Planar view of the amplitude of a propagating Gaussian beam with beam waist radius of 2 wavelengths.
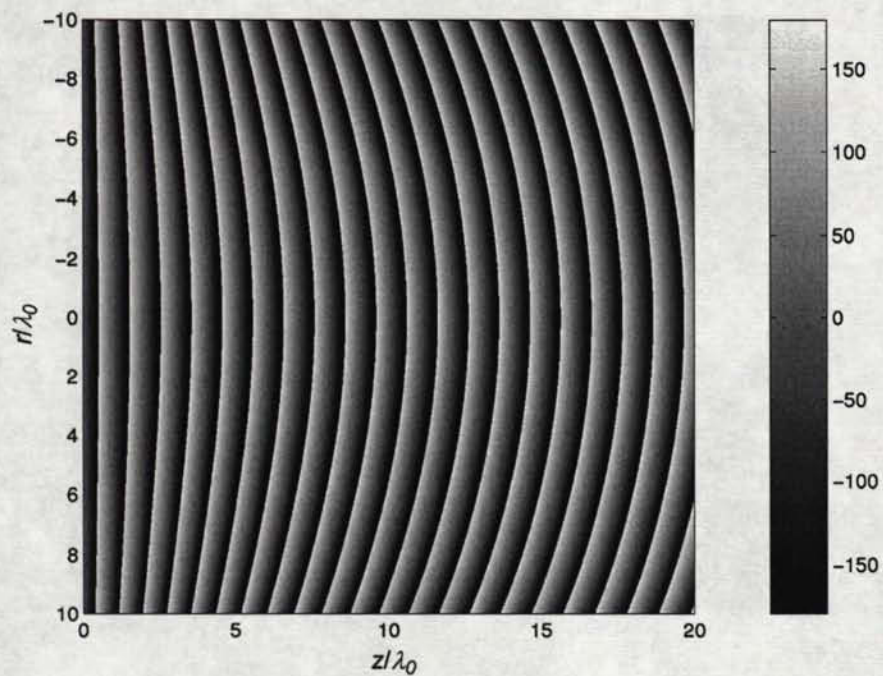
Figure 2.9: Planar view of the phase of a propagating Gaussian beam with beam waist radius of 2 wavelengths.
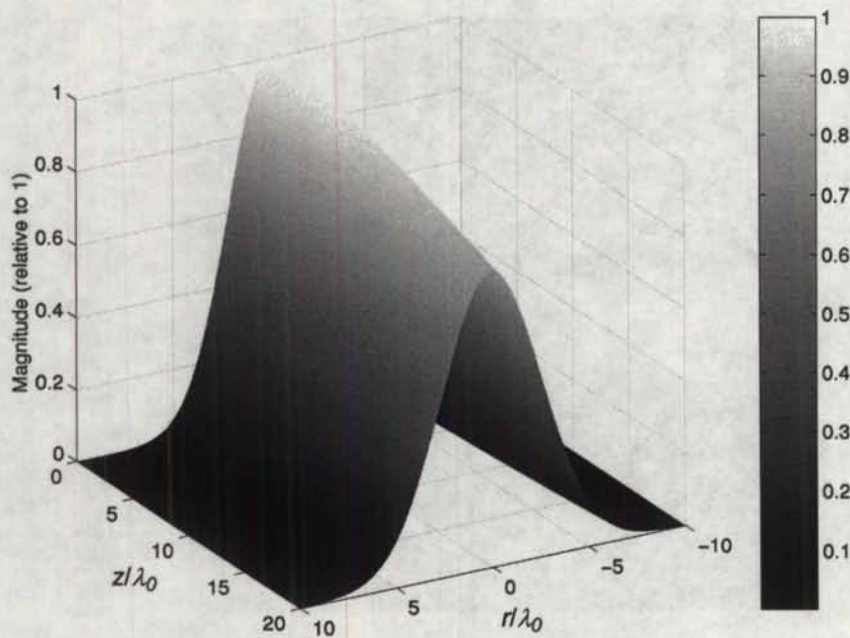
Figure 2.10: Three-dimensional view of the amplitude of a propagating Gaussian beam with beam waist radius of 3 wavelengths.
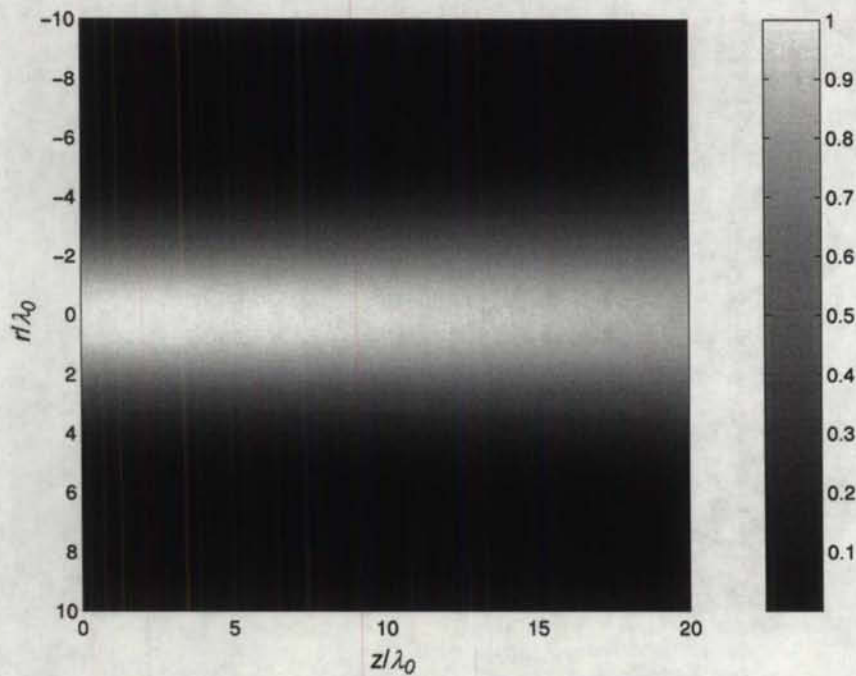
Figure 2.11: Planar view of the amplitude of a propagating Gaussian beam with beam waist radius of 3 wavelengths.
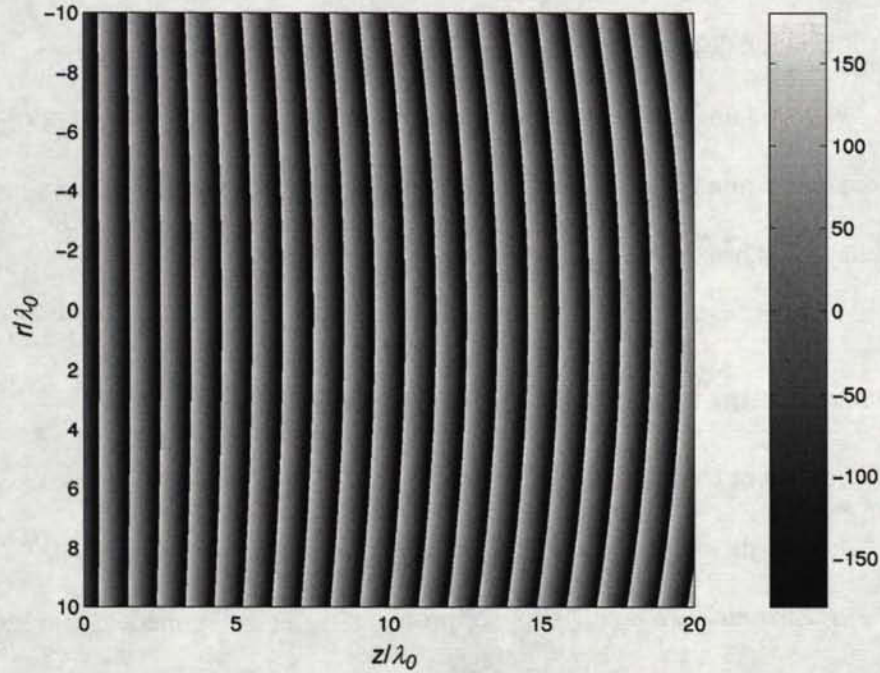
Figure 2.12: Planar view of the phase of a propagating Gaussian beam with beam waist radius of 3 wavelengths.

mentioned in section 2.3.1, the propagating beam has to be fairly well collimated in order to obtain the paraxial wave equation. The satisfying criterion would then be the width of the beam, i.e. the beam radius. As shown in section 2.3.2, a large beam waist corresponds to a collimated beam while a small beam waist corresponds to a divergent beam. Many studies have been conducted in order to determine the minimum beam width for which the paraxial equation is still valid [12-14]. It is generally accepted that the beam waist has to be at least as large as a wavelength in order to apply the paraxial equation [12].

The second limitation concerns the higher-order modes of the propagating beam. Most common launchers radiate beams characterised by the fundamental Gaussian mode plus higher-order modes. In this case, the propagating beams are referred to Gauss-Hermite beams in rectangular coordinates and Gauss-Laguerre beams in cylindrical

coordinates [8], which are also solutions to (2-7) and (2-8), respectively. The purity of the beam depends on the design of the radiating element. Even if a pure fundamental Gaussian mode is not easy to launch since higher-order modes will always be present, a fundamental Gaussian mode is commonly assumed because it still provides an accurate solution in most of the problems and because it is much easier to apply.

2.4 Gaussian Beam Launching and Transformation

2.4.1 Gaussian Beam Launchers

In the analysis of Gaussian beam propagation, the fundamental mode is often the only mode considered. A much simpler problem is then obtained at the expense of relatively small errors. Not every radiating element has the capability of propagating only the fundamental Gaussian beam. The most common radiating elements that produce fundamental Gaussian radiation patterns are waveguide horns. Among them, the corrugated feed horns are the most effective fundamental Gaussian beam radiators if they are properly designed. However, these antennas are complex, heavy, bulky and require precise manufacturing tolerances.

As an alternative, simple and common rectangular feed horns were used instead of corrugated horns. Figure 2.13 shows a representation of a rectangular feed horn. With a rectangular waveguide feed the beam widths in the H-plane and in the E-plane are related to the length a and b (as shown in Figure 2.13), respectively. A symmetric pattern can be obtained by simply applying the following equation [10]:

$$\frac{b}{a} = 0.73 . \qquad (2\text{-}16)$$
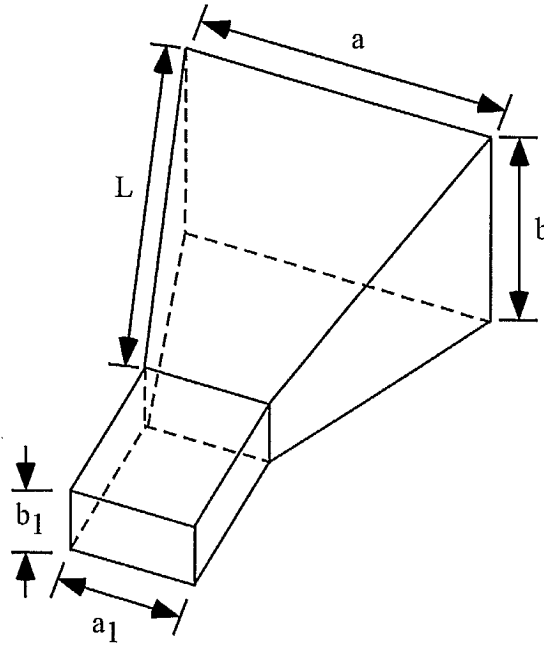
Figure 2.13: Representation of a rectangular feed horn.

Furthermore, the beam waist radius can be approximated using the following equation [10]:

$$w_0 \cong 0.32a \text{ or } w_0 \cong 0.44b. \tag{2-17}$$

There are other types of feeding elements for quasi-optical systems than corrugated and rectangular horns. Other common antennas include conical feed horns, and slotline antennas operating in the end-fire mode. The latter are of interest because of their low fabrication cost. A complete list of Gaussian beam radiators has been prepared by Goldsmith and is presented in [8, 10].

2.4.2 Gaussian Beam Parameter Determination

For a Gaussian beam feed, the size and location of the beam waist is a critical parameter. As mentioned in section 2.3.2, the beam radius and the radius of curvature are

two important parameters of a propagating Gaussian beam. These two parameters are described by (2-10) and (2-11). Knowledge of the beam radius or the radius of curvature at two different positions is necessary in order to find the accurate location and size of the beam waist. Obviously, (2-17) gives an approximation of the beam waist radius with respect to the size of a rectangular feed horn, but this is not an accurate measurement even though it can be used as a guide.

The best approach is to measure the radiating element in a near-field measurement system at two different distances. From these measurements, the beam radius can be determined as the distance where the beam power drops to $1/e^2$, or −8.686 dB. Knowing the relative distance between the two sets of measurements, the location of the beam waist and its radius can be found using (2-10). However, this type of measurement is not always possible and other solutions have to be found.

Another approach is to measure the far-field radiation pattern of the antenna. This is a more common type of measurement, from which the radiating power is measured as a function of angle. As mentioned in [8], the $1/e^2$ radius of the power of the beam can be expressed as

$$\tan \theta = \frac{w(z)}{z}. \tag{2-18}$$

In far-field measurements, the distance z is assumed infinite. Furthermore, defining θ_0 as the asymptotic beam growth angle, or the angle where the power drops to $1/e^2$ or −8.686 dB relative to the on-axis power, and replacing w in (2-18) by (2-10), we obtain

$$\tan \theta_0 = \lim_{z \to \infty} \frac{w_0 \left[1 + \left(\frac{\lambda_0 z}{\pi w_0^2} \right)^2 \right]^{0.5}}{z} = \frac{\lambda_0}{\pi w_0}. \tag{2-19}$$

From the radiation patterns, θ_0 is measured, therefore w_0 is obtained.

Since the beam waist location is still unknown, another source of information is required. For feed horns, a good assumption is that the field distribution at the aperture is spherical with radius of curvature R equal to the slant length ρ of the horn [8], as illustrated in Figure 2.14. Therefore, there are two known parameters at two different distances: the beam waist radius (obtained from far-field measurements) and the radius of curvature at the output of the feed horn. The position of the radius of curvature is physically known so that it can provide information on the location of the beam waist.

Inverse formulas presented in [8] allow to find any missing parameter of the Gaussian beam from two known parameters. In this case:

$$z = \frac{R}{2}\left\{1 \pm \left[1 - \left(\frac{2\pi w_0^2}{\lambda_0 R}\right)^2\right]^{0.5}\right\},$$

(2-20)

where w_0 and λ_0 are known, R is equal to ρ, the slant length, and z is the distance between the constant phase surface and the beam waist location, represented by Δ, as shown in Figure 2.14. Therefore, (2-20) can be rewritten as:

$$\Delta = \frac{\rho}{2}\left\{1 \pm \left[1 - \left(\frac{2\pi w_0^2}{\lambda_0 \rho}\right)^2\right]^{0.5}\right\}.$$

(2-21)

To obtain the distance between the aperture plane and the beam waist location, d, which is more useful information, the following equation is derived from Figure 2.14:

$$\Delta - d = \rho - p.$$

(2-22)

Isolating for d in (2-22):

$$d = \Delta + p - \rho.$$

(2-23)
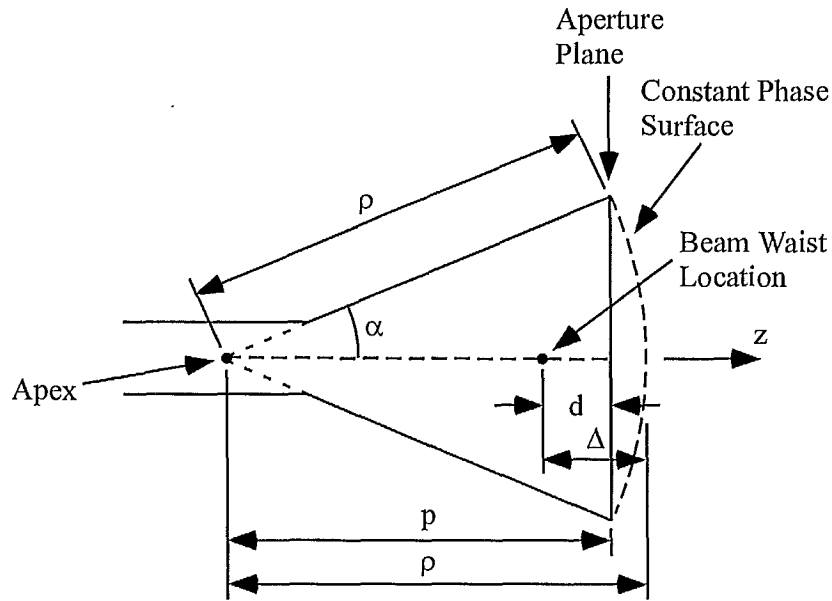
Figure 2.14: Representation of some parameters of a feed horn.

For pyramidal horns, the slant length, ρ, will be different depending on the plane. For that reason, the beam waist location is different in the E-plane and H-plane. Therefore, the beam waist location will have to be chosen in order to satisfy both planes.

2.4.3 Transformation by a Focusing Lens

In the design of the quasi-optical test bench, a focusing lens is used to modify the Gaussian beam. An ideal lens does not modify the amplitude distribution of a propagating beam; it simply acts as a phase transformer by introducing a phase shift $\Delta\theta$ defined as [10]:

$$\Delta\theta = \frac{\pi r^2}{\lambda_0 f},$$

(2-24)

where f is the focal length of the lens. The phase transformation changes the radius of curvature of the beam, which has the effect of focusing the beam or, in other words, creating a new beam waist [10]. Figure 2.15 shows a propagating Gaussian beam being

modified by a quasi-optical lens. The distance parameters listed in this figure are described in [15].

The relationship between the input beam waist radius, w_{in}, the output beam waist radius, w_{out}, and the focal length can be derived using the ray transfer matrices [8]. The relationship depends on the location of the input and output beam waists. A special case is obtained if the distance between the input beam waist and lens input plane is equal to the focal length of the lens, as shown in Figure 2.15. In such a configuration, the distance between the output beam waist and the lens input plane is also equal to the focal length. The thin lens expression that describes this beam transformation is:

$$f = \frac{\pi w_{in} w_{out}}{\lambda_0}.$$

(2-25)
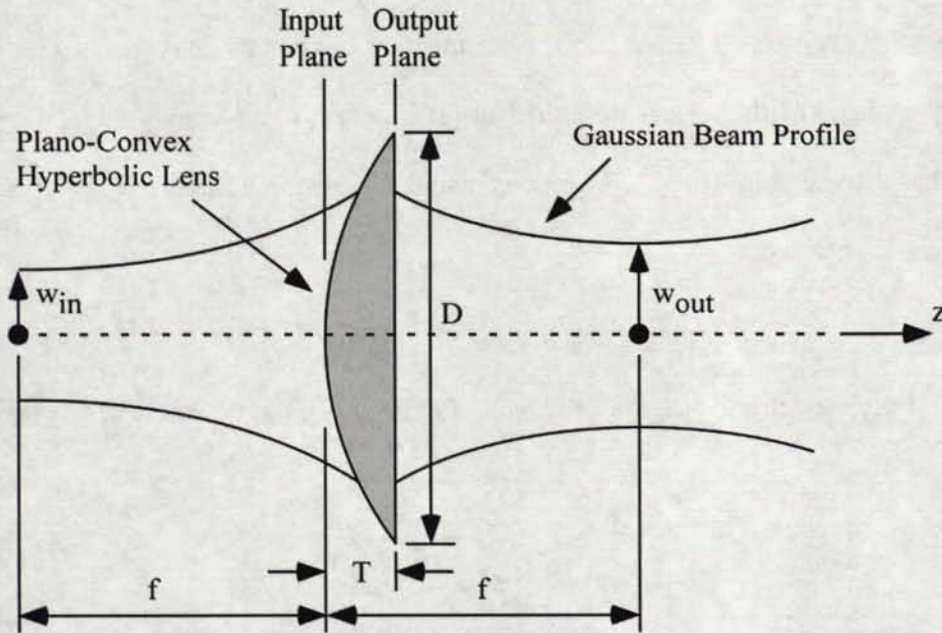
Figure 2.15: Representation of a Gaussian beam being modified by a focusing lens.

Another important parameter of the lens is the lens diameter D, as shown in Figure 2.15. A large enough diameter is desired in order to intercept a large fraction of the power. The edge taper and the fractional power are used to obtain the amount of power intercepted by the lens. The edge taper, T_e, is defined as the relative power density at radius r_e [8]:

$$T_e(r_e) = \exp\left[-2\left(\frac{r_e}{w}\right)^2\right],$$ (2-26)

which is derived from (2-15). In dB, (2-26) simplifies to

$$T_e(dB) = 8.686\left(\frac{r_e}{w}\right)^2.$$ (2-27)

We can also define the fractional power, F_e, as the density function of the edge taper:

$$F_e(r_e) = 1 - T_e(r_e),$$ (2-28)

which describes how much power of the fundamental Gaussian mode is within a radius r_e.

The shape of the lens is described in [16]. For a plano-convex lens, the curved surface has a hyperbolic shape. By proper manipulation, the three-dimensional equation for the lens is obtained:

$$x^2 + y^2 = (\varepsilon_r - 1)z^2 + 2f\left(\sqrt{\varepsilon_r} - 1\right)z,$$ (2-29)

where ε_r is the dielectric constant of the lens. From (2-29), the thickness of the lens, T, is found:

$$T = \left(\frac{1}{\sqrt{\varepsilon_r} + 1}\right)\left(\sqrt{f^2 + \frac{D^2}{4}\frac{\sqrt{\varepsilon_r} + 1}{\sqrt{\varepsilon_r} - 1}} - f\right).$$ (2-30)

2.5 Gaussian Beam Coupling

Gaussian beam coupling analysis can be used to determine how much power is being transferred between two Gaussian beams. To simplify the analysis, the beams are considered to be only one-dimensional. A Gaussian beam defined in the x direction is obtained from (2-9) as

$$u(x) = \left(\frac{2}{\pi w_x^2}\right)^{0.25} \exp\left(-\frac{x^2}{w_x^2} - j\frac{\pi x^2}{\lambda_0 R_x}\right), \tag{2-31}$$

where the Gaussian beam phase shift is neglected because its effect on the overall coupling mechanism is insignificant. The subscript x simply identifies the dimension in which the beam is defined. As a result, the field coupling coefficient in one dimension between two Gaussian beams, say u_a propagating in the positive z direction and u_b propagating in the negative z direction, is [8]:

$$c_{ab}^{1x} = \int_{-\infty}^{\infty} u_a^*(x) u_b(x) dx. \tag{2-32}$$

Inserting (2-31) into (2-32):

$$c_{ab}^{1x} = \int_{-\infty}^{\infty} \left[\left(\frac{2}{\pi w_{xa}^2}\right)^{0.25} \exp\left(-\frac{x^2}{w_{xa}^2} + j\frac{\pi x^2}{\lambda_0 R_{xa}}\right)\right]\left[\left(\frac{2}{\pi w_{xb}^2}\right)^{0.25} \exp\left(-\frac{x^2}{w_{xb}^2} - j\frac{\pi x^2}{\lambda_0 R_{xb}}\right)\right] dx,$$

$$c_{ab}^{1x} = \left(\frac{2}{\pi w_{xa} w_{xb}}\right)^{0.5} \int_{-\infty}^{\infty} \exp\left[-\left(\frac{1}{w_{xa}^2} + \frac{1}{w_{xb}^2} + j\frac{\pi}{\lambda_0}\left(\frac{1}{R_{xb}} - \frac{1}{R_{xa}}\right)\right)x^2\right] dx. \tag{2-33}$$

Knowing that

$$\int_{-\infty}^{\infty} \exp(-ax^2) dx = \left(\frac{\pi}{a}\right)^{0.5},$$

(2-33) gives the following result:

$$c_{ab}^{1x} = \left(\frac{2}{\pi w_{xa} w_{xb}} \right)^{0.5} \left(\frac{\pi}{\left(\frac{1}{w_{xa}^2} + \frac{1}{w_{xb}^2} + j\frac{\pi}{\lambda_0}\left(\frac{1}{R_{xb}} - \frac{1}{R_{xa}} \right) \right)} \right)^{0.5} ,$$

$$c_{ab}^{1x} = \left[\frac{2}{\left(\frac{w_{xb}}{w_{xa}} + \frac{w_{xa}}{w_{xb}} \right) + j\frac{\pi w_{xa} w_{xb}}{\lambda_0}\left(\frac{1}{R_{xb}} - \frac{1}{R_{xa}} \right)} \right]^{0.5} . \qquad (2\text{-}34)$$

A representation of Gaussian beam coupling in x is shown in Figure 2.16. Finally, the exact same analysis can be conducted in y, which will lead to a similar result.

The power coupling factor between the two beams is defined as

$$K_{ab} = \left| c_{ab}^{1x} \cdot c_{ab}^{1y} \right|^2 . \qquad (2\text{-}35)$$
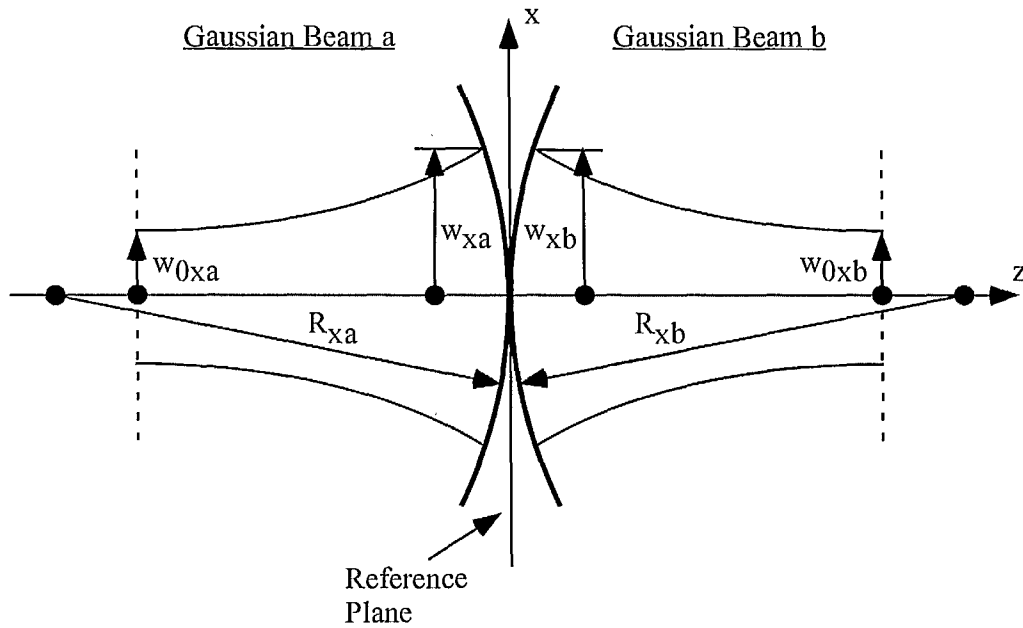
Figure 2.16: One-dimensional Gaussian beam coupling.

28

The power coupling factor is an important parameter that states how much power is transferred between two beams. Its value varies between 0 and 1, where unity corresponds to the zero loss condition.

CHAPTER 3 Quasi-Optical Measurement System Description and Design

3.1 Introduction

This chapter presents a review of the various types of measurement systems that can be used to characterise materials. The quasi-optical transmission/reflection measurement system is found to be the best candidate, and the complete design of the various components of this setup are described. The measurement technique and calibration process are also reported.

3.2 Comparison of Measurement Systems and Techniques for Material Characterisation

The choice of a measurement system depends on many factors: cost, flexibility, frequency of interest, accuracy required, shape of the sample, physical modification of the sample, etc. This section presents various measurement techniques and how the quasi-optical measurement system best suits our current needs.

3.2.1 Characterisation Techniques

The characterisation techniques used to measure materials can be separated into three main categories: reflection techniques, transmission/reflection techniques and resonance techniques. The first two techniques consist of measuring the S-parameters of the sample, from which the dielectric parameters can be extracted. The reflection

techniques require that the sample under test is backed with metal and only the reflection coefficient is recorded [17, 18] whereas the transmission/reflection techniques measure both transmission and reflection coefficients [19, 20] (the quasi-optical test bench to be developed is a reflection/transmission measurement system). Resonance techniques normally consist of introducing a slab of dielectric material into a resonator. The dielectric properties of the material are then obtained from the resonance frequency and the width of the resonance peak [21, 22].

Reflection and transmission/reflection techniques have the advantage of being broadband techniques, whereas resonance techniques only provide the information near the resonance frequency. Therefore, resonance techniques are not suited for materials that are characterised by a large variation of the permittivity over frequency, water being an example.

Transmission/reflection techniques have been found quite inaccurate in measuring the loss tangent of low-loss materials (loss tangent less than 0.005) and medium-loss materials (loss tangent between 0.005 and 0.1) [19]. Results obtained using reflection techniques revealed that this approach is suited for high-loss and medium-loss materials, but it is not accurate for low-loss materials [17]. Resonance techniques are usually very sensitive, which makes them good for measuring low-loss materials and medium-loss materials with loss tangents up to about 0.05 [21]. However, their performance degrades rapidly as the loss tangent increases above 0.05 since the resonance may become indistinguishable. For this work, as mentioned in Chapter 1, one of the uses for the measurement setup is to measure semiconductor materials when exposed to optical illumination. This causes an increase in conductivity, thereby increasing the losses in the

material. For this reason, resonance techniques are not appropriate for measuring these semiconductors. Since reflection techniques require metal backing, optical illumination would not be possible from behind the sample and the metal layer could limit the accuracy of the measurement if the semiconductor thickness is smaller than the skin depth. Therefore, reflection techniques are not the best choice either.

Finally, transmission/reflection techniques allow the measurement of any type of material, including magnetic and anisotropic materials [23]. This is usually not the case for the two other techniques, although some complex resonance techniques allow the determination of magnetic properties. Furthermore, even if this technique is not as accurate as the others for measuring the loss tangent, it is not an essential feature for the continuation of the project since the intended usage of this system is for the measurement of optically-induced materials, which would be quite lossy. Moreover, for low-loss materials, knowledge of the loss tangent is not as important as the dielectric constant since below a certain range the loss tangent value is normally not significant. These reasons led to the choice of the transmission/reflection technique.

3.2.2 Types of Transmission/Reflection Techniques

Different types of transmission media can be used in the determination of material properties. The most important types are: waveguide, coaxial, transmission lines and free-space. The quasi-optical test bench is a free-space measurement system. In the present case, the frequency of interest is 30 GHz. As frequency increases, losses inside many transmission media increase and phase measurement becomes inaccurate. This is the case for coaxial cables and most printed lines.

Waveguides are known to be efficient at high frequencies. However, using waveguide technology requires high-precision machining of the sample under test, which has to be inserted into the waveguide. Positioning of the sample is also critical, especially at high frequency since the dimensions of the waveguide are small, making alignment more difficult. All these issues lead to increased process cost. Furthermore, optical illumination inside a waveguide would be a complicated task to achieve.

A free-space measurement technique is not affected by these drawbacks. Free-space measurements allow contactless and non-destructive characterisation, which makes possible physical modification of the sample under test, such as variation of its temperature or optical illumination. The sample preparation is relatively simple when compared to alternative methods. Finally, the measurement system is flexible as it can be used to measure quasi-optical components as well as materials [24].

The free-space transmission/reflection or quasi-optical test bench has some disadvantages. As mentioned in the previous section, it is not as accurate as other techniques for measuring the loss tangent of low-loss materials. Misalignments are also critical to the accuracy of the system. Chapter 4 is devoted to the misalignment issue. Misalignments can also be responsible for other problems, like having a non-plane wave at the surface of the sample. Accuracy of the measurement is also reduced because of the standing wave or multiple reflections between the two feed horns. Other source of errors in the measurement include diffraction, finite size of the sample and reflection from the environment [23]. Table 3.1 presents the major advantages and disadvantages of the quasi-optical measurement system.

Table 3.1: Advantages and disadvantages of the free-space measurement system.

Advantages	Disadvantages
Contactless and non-destructive	Misalignments
Simple sample preparation	Standing wave
Broadband measurement	Diffraction
High-frequency	Inaccurate loss tangent for low-
Measurement flexibility	and medium-loss materials

3.3 Topology of the Quasi-Optical Test Bench

The measurement system is designed to obtain the amplitude and phase of the reflection and transmission coefficients of a thin planar sample of material. This data is then used to determine the dielectric properties of the sample. In order to obtain this data, a two-port measurement system is necessary. A popular free-space two-port configuration for material measurement is shown in Figure 3.1. A similar configuration was previously reported in [19, 20, 24, 25].
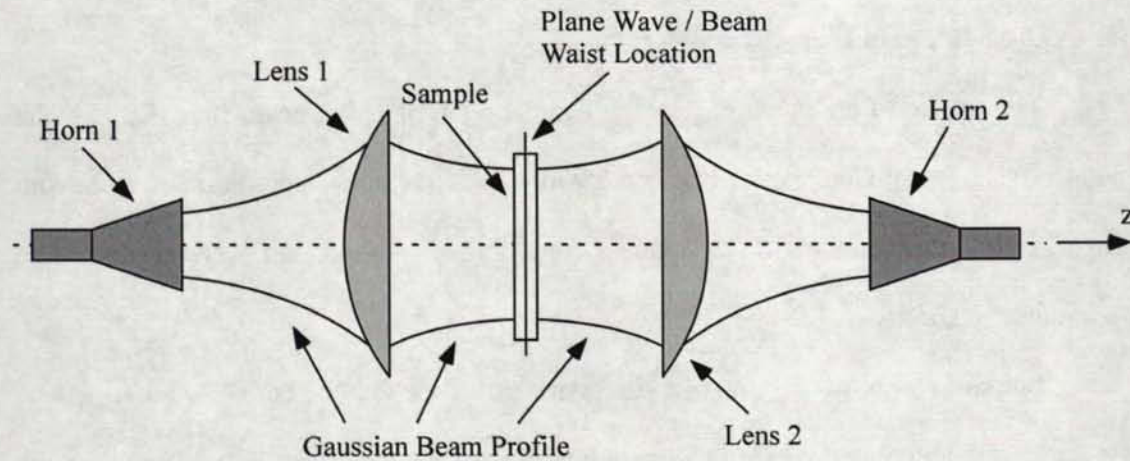
Figure 3.1: Quasi-optical test bench.

The quasi-optical test bench uses two antennas, typically feed horns, to launch Gaussian beams. The Gaussian beams are then refocused with hyperbolic lenses. Refocusing the beams also has the advantage of creating a Gaussian plane wave midway between the two lenses. The sample under test is placed at this location, which allows the use of plane wave theory in order to extract the material properties, as will be shown in Chapter 5. Furthermore, the quasi-optical test bench is designed to be symmetrical, i.e. the components on each side of the sample under test are identical and the distance between the components is the same.

3.4 Component Design

This section presents the design of the constitutive components of the quasi-optical apparatus. More specifically, the choice and characterisation of a launching device and a focusing lens are presented. Finally, the complete setup is studied as a unit.

3.4.1 Gaussian Beam Launcher

The choice of an antenna capable of radiating a Gaussian beam is critical. If the radiated beam is not Gaussian or if it is too wide, Gaussian optics approximations may no longer apply. As mentioned in Chapter 2, the launching components were chosen to be pyramidal feed horns.

For simplicity, we are interested in symmetrical beams for both E- and H-planes. This allows for the use of rotationally symmetric lenses, which can be inserted into the setup without the need of rotational alignment along the x and y axes. Table 3.2 presents the dimensions of the feed horn used (see Figure 2.13 for more details). Such dimensions

guarantee symmetrical beams and large enough beam waist radius to allow application of the paraxial wave equation. For these dimensions, the ratio b over a is

$$\frac{b}{a} = \frac{25}{35} \approx 0.714 . \qquad (3\text{-}1)$$

According to (2-16), we can state that the propagating beam launched by this feed horn is symmetrical. From (2-17), these dimensions result in a beam waist radius of about

$$w_0 \cong 0.32(35mm) \approx 11.2mm \text{ or } w_0 \cong 0.44(25mm) \approx 11mm . \qquad (3\text{-}2)$$

For a measurement system designed to operate at 30 GHz, the free-space wavelength is 10 mm; therefore, the values of the beam waist radius obtained in (3-2) show that it is larger than a wavelength, and the paraxial approximation can be applied.

To verify the symmetry of the beam and to evaluate with more accuracy the beam waist radius, the far-field radiation patterns of the feed horns were measured. Figure 3.2 shows the measured radiation patterns for both feed horns at 30 GHz. In addition, a Gaussian beam pattern is included in the radiation patterns in order to compare with the feed horn patterns. From the radiation patterns, it is observed that E-plane and H-plane radiation can be considered symmetrical from 0° up to about ±20°. Moreover, the asymptotic beam growth angle (which corresponds to the angle where the power drops to $1/e^2$ or −8.686 dB) is found to be approximately 16°. From (2-19), using a wavelength of

Table 3.2: Measured dimensions of rectangular feed horn.

Dimension	Symbol	Value (mm)
Longest dimension of the aperture	a	35
Smallest dimension of the aperture	b	25
Extension length	L	77
Waveguide longest dimension	a_1	7.112
Waveguide smallest dimension	b_1	3.556

(a)

(b)
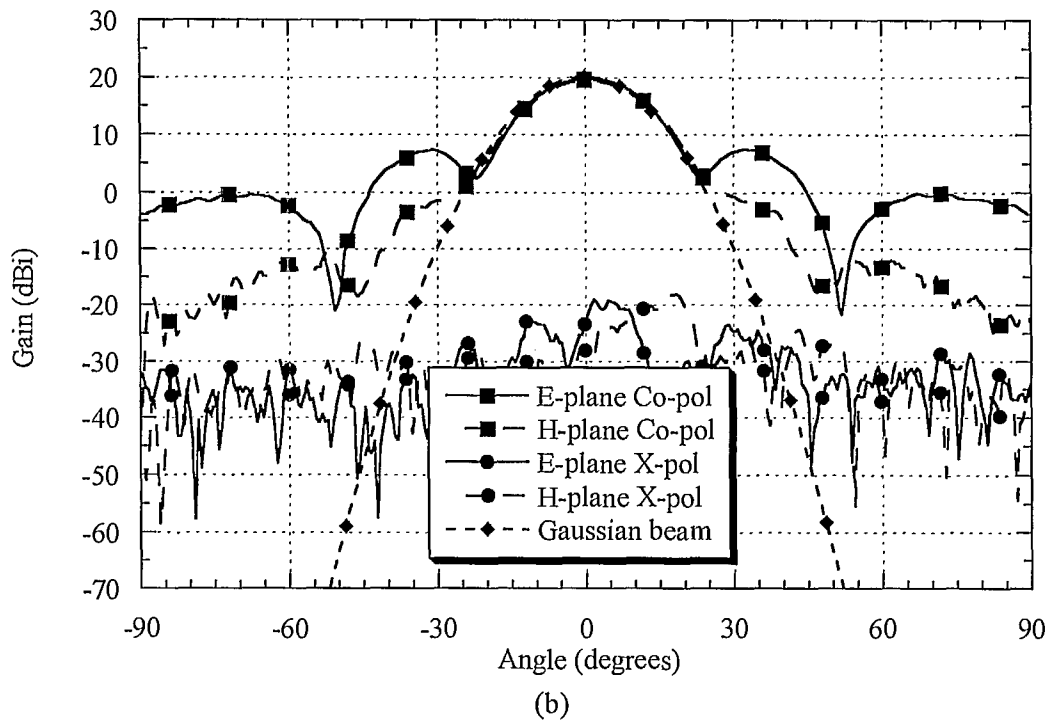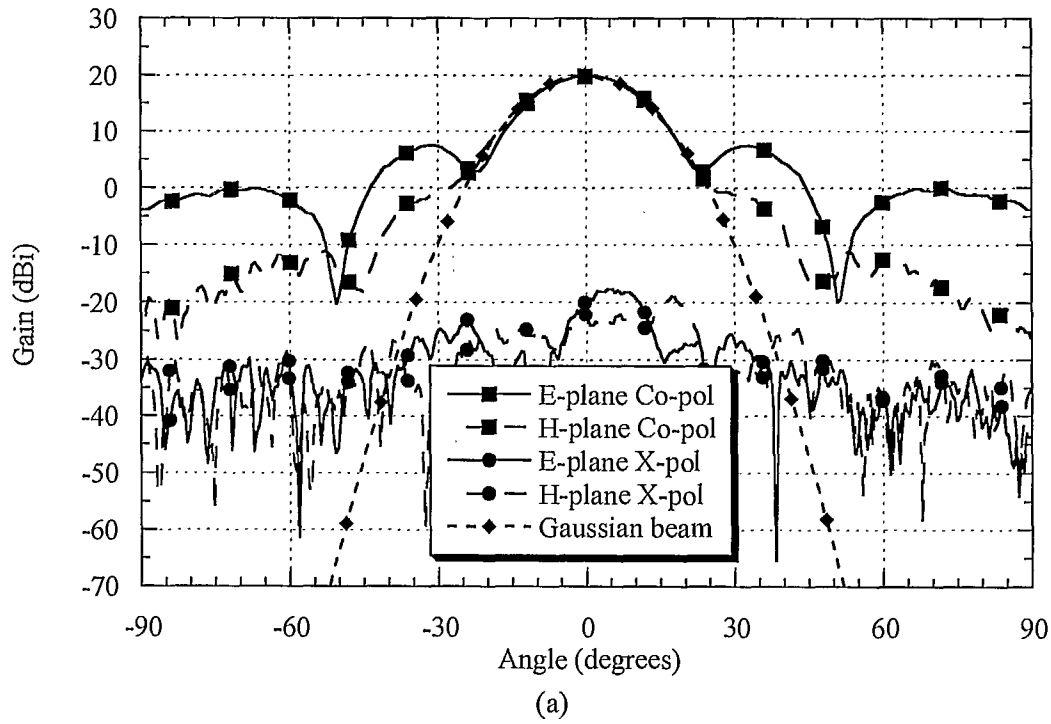
Figure 3.2: Far-field radiation patterns and Gaussian beam profile of beam waist radius 1.1 cm for (a) feed horn at port 1; (b) feed horn at port 2.

10 mm, a beam waist radius of 11.1 mm is found, which is in agreement with the approximate results in (3-2). Furthermore, the Gaussian beam in Figure 3.2 is obtained with a beam waist radius equal to 11 mm and reveals that the E-plane and H-plane co-pol radiation patterns are fairly Gaussian up to about ±20°.

We are now interested in the location of the beam waist with respect to the aperture of the horn. Appendix A develops all the required formulas to be applied in order to find the apex-to-aperture distance and the slant length. Table 3.3 presents the results of the apex-to-aperture distance and the slant length in both E- and H-plane. In addition, (2-21) and (2-23) are used to calculate the beam waist location with respect to the aperture plane. In the E-plane:

$$\Delta_e = \frac{\rho_e}{2}\left\{1\pm\left[1-\left(\frac{2\pi w_0^2}{\lambda_0 \rho_e}\right)^2\right]^{0.5}\right\} = \frac{88.28mm}{2}\left\{1\pm\left[1-\left(\frac{2\pi(11mm)^2}{(10mm)(88.28mm)}\right)^2\right]^{0.5}\right\} = 21.70mm,$$

(3-3)

$$d_e = 21.70mm + 87.39mm - 88.28mm = 20.81mm.$$

(3-4)

In the H-plane:

$$\Delta_h = \frac{\rho_h}{2}\left\{1\pm\left[1-\left(\frac{2\pi w_0^2}{\lambda_0 \rho_h}\right)^2\right]^{0.5}\right\} = \frac{95.69mm}{2}\left\{1\pm\left[1-\left(\frac{2\pi(11mm)^2}{(10mm)(95.69mm)}\right)^2\right]^{0.5}\right\} = 18.79mm,$$

(3-5)

$$d_h = 18.79mm + 94.08mm - 95.69mm = 17.18mm.$$

(3-6)

Table 3.3: Calculated values for a rectangular feed horn.

Dimension	Symbol	Value (mm)
Apex-to-aperture distance in the E-plane	p_e	87.39
Apex-to-aperture distance in the H-plane	p_h	94.08
Slant length in the E-plane	ρ_e	88.28
Slant length in the H-plane	ρ_h	95.69

Table 3.4: Quasi-optical parameters of the pyramidal horn.

Parameter	Symbol	Value (mm)
Beam waist radius or Input beam waist radius	w_0 or w_{in}	11
Waist-to-aperture distance	d	19

The effective beam waist location is chosen to be about the average of the two values found above:

$$d \cong \frac{d_e + d_h}{2} = \frac{20.81mm + 17.18mm}{2} \approx 19mm. \tag{3-7}$$

Table 3.4 shows the quasi-optical parameters of the pyramidal horn.

3.4.2 Focusing Lenses and Lens Design

The lens is designed to satisfy the following requirements:

— the focal length is chosen in order to focus the beam to an appropriate size;

— the focal length is chosen to offer a large enough separation between the components of the test bench;

— the diameter is chosen so that a large fraction of the power is intercepted.

The lenses used were designed using a Plexiglas material. The diameter of the lens was 89.27 mm, the thickness was 14.94 mm and the focal length was designed to be 93 mm. Knowing that Plexiglas has a refractive index of 1.6, which corresponds to a dielectric constant of 2.56 [8], the equation of the lens, as given by (2-29), is:

$$x^2 + y^2 = 1.56z^2 + (111.6mm)z. \tag{3-8}$$

Table 3.5 summarises the parameters of the lens.

Table 3.5: Parameters of the Plexiglas focusing lens.

Parameter	Symbol	Value
Focal length (mm)	f	93
Diameter (mm)	D	89.27
Thickness (mm)	T	14.94
Dielectric constant	ε_r	2.56

As will be discussed in section 3.4.3, the size of the sample under test is limited to a diameter of 75mm. This will have a considerable effect on the choice of the output beam waist as it must be shorter than this size in order to avoid any undesired diffraction at the edge of the sample. Using (2-28), it can be shown [25] that 98.89% of the power is intercepted if the radius of the sample is 1.5 times larger than the output beam waist radius, or that 99.97% of the power is intercepted if it is 2 times larger. For a focal length of 93 mm and assuming the input beam waist is 11 mm, the output beam waist radius at 30 GHz is obtained using (2-25):

$$w_{out} = \frac{\lambda_0 f}{\pi w_{in}} = \frac{(10mm)(93mm)}{\pi(11mm)} = 26.91mm. \tag{3-9}$$

With such a value of output beam waist radius and a sample of radius equal to 37.5 mm, the fraction of the power intercepted is given by (2-28):

$$F_e = 1 - \exp\left[-2\left(\frac{r_e}{w}\right)^2\right] = 1 - \exp\left[-2\left(\frac{37.5mm}{26.91mm}\right)^2\right] = 97.94\%. \tag{3-10}$$

The diameter of the lens can give us the value of the edge taper at the lens location. In order to find this value, the beam radius must be known at the input surface of the lens. This is determined using (2-10):

$$w(z = f) = w_0\left[1 + \left(\frac{\lambda_0 f}{\pi w_0^2}\right)^2\right]^{0.5} = 11mm\left[1 + \left(\frac{(10mm)(93mm)}{\pi(11mm)^2}\right)^2\right]^{0.5} = 29.07mm. \tag{3-11}$$

Knowing the value of the diameter of the lens, the edge taper can be found using (2-27):

$$T_e(dB) = 8.686\left(\frac{89.27mm/2}{29.07mm}\right)^2 = 20.5 dB. \tag{3-12}$$

Therefore, more than 99% of the power is intercepted by the lens.

The ratio of the focal length over the diameter of the lens provides useful information on the validity of the thin lens approximation. For large ratios of f/D, as it is the case in optics since propagating beams are usually fairly well collimated, the thin lens approximation holds. However, for small f/D ratios, i.e. for $f/D = 1$, the thin lens approximation is not valid and the thickness of the lens must be considered. In this case, the f/D ratio is 1.042, which is fairly small. Therefore, some parameters like the output beam waist may have to be corrected later on.

The other important parameter is the width of the beam intercepted by the lens. Figure 3.3 shows the width of the beam intercepted by the lens. The intercepted angle is calculated from this figure. The value obtained should be close to the Gaussian approximation, as shown in Figure 3.2. With the appropriate values, we find that:

$$\theta = \arctan\left(\frac{D/2}{f+T}\right) = \arctan\left(\frac{89.27mm}{2(93.00mm + 14.94mm)}\right) = 22.47°, \tag{3-13}$$

which is close enough to the estimated value of 20° to conclude that the intercepted beam is fairly Gaussian.

3.4.3 Sample Under Test

The sample under test is placed at the output beam waist location, where a plane wave exists. The size of the output beam waist radius must be smaller than the sample
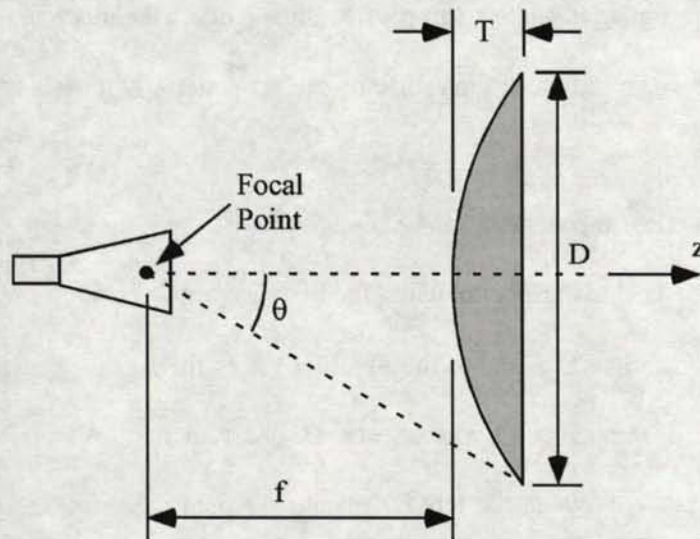
Figure 3.3: Width of the propagating beam intercepted by the lens.

under test, typically between 1.5 and 2 times. From (3-9), knowing that the samples to be measured are circular disks with diameter of 75 mm, the ratio of the sample radius over the output beam waist radius is found to be 1.39, which is close enough to the required values. From (3-10), it was found that almost 98% of the power is intercepted by the sample. The size of the samples was dictated by the silicon wafers available for the future experiments with optical illumination. The thickness of the samples is typically between 0.25 mm and 3 mm.

3.4.4 Component Positioning

The separation between the various components of the quasi-optical test bench is critical. As discussed in section 2.4.3, it was decided to have the distance between the input beam waist and the input plane of the lens equal to the focal length of the lens. Thus, the distance between the output beam waist and the input plane of the lens is also equal to

the focal length of the lens. The sample under test is then placed at the output beam waist. Therefore, a plane wave is obtained at the sample location since a beam waist always corresponds to a point where the radius of curvature of the propagating Gaussian beam is infinite.

Figure 3.4 shows the theoretical dimensions of the measurement system. Theoretically, maximum power transfer occurs when the distance between the output beam waist and the input plane of the lens is equal to the focal length of the lens. Therefore, the separation between the horn and the lens was chosen in order to maximise the power transfer. Similarly, the distance between the lenses was chosen using the same technique, while keeping the distance between the horn and lens constant. The experimental dimensions of the setup are close to the theoretical ones.
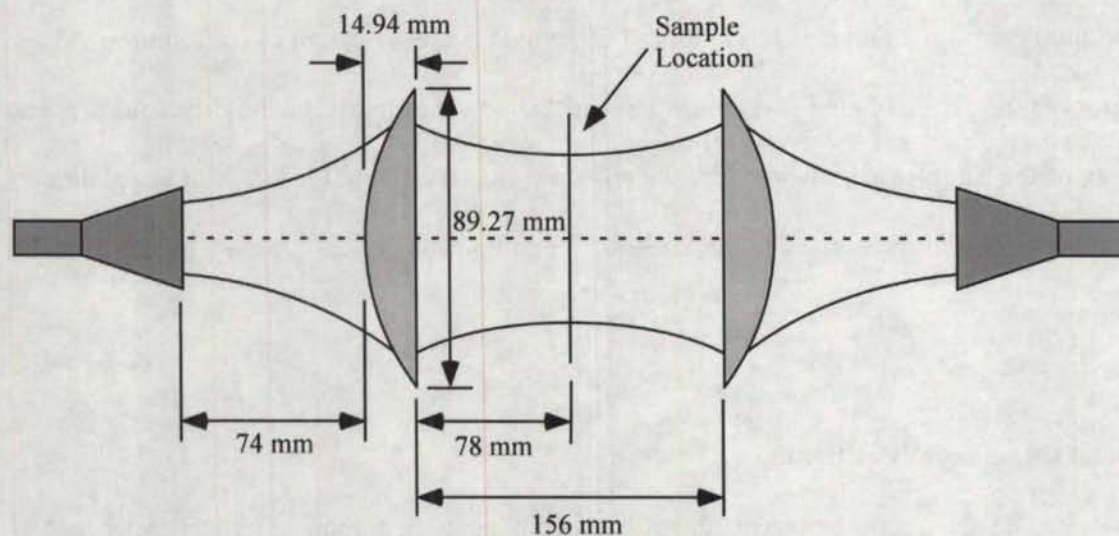
Figure 3.4: Dimensions of the measurement system.

3.5 Measurement Technique and Calibration

3.5.1 Measurement Technique

In order to determine the dielectric constant of a sample under test, the magnitude and phase of the reflection and transmission coefficients of the sample must be determined. Determining the transmission coefficient requires a two-port measurement, thus a vector network analyser was used. The ports of the analyser were connected to the horn antennas of the quasi-optical test bench as shown in Figure 3.5. Pictures of the measurement system are presented in Figure 3.6.

3.5.2 Types of Calibration Techniques

Measurements performed with a network analyser require calibration in order to compensate for the systematic errors of the instrument. Calibration is performed by measuring standards and is used to characterise and correct the systematic errors.
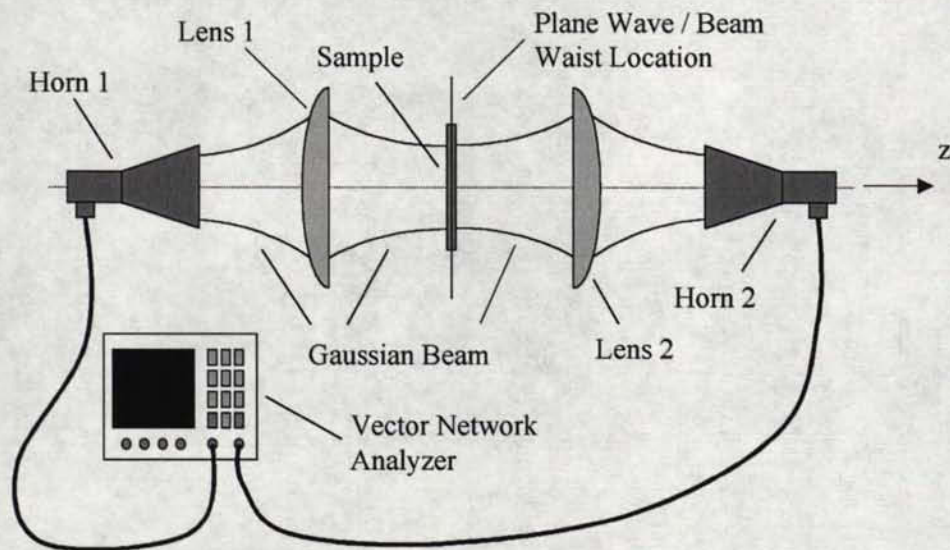
Figure 3.5: Quasi-optical measurement system.
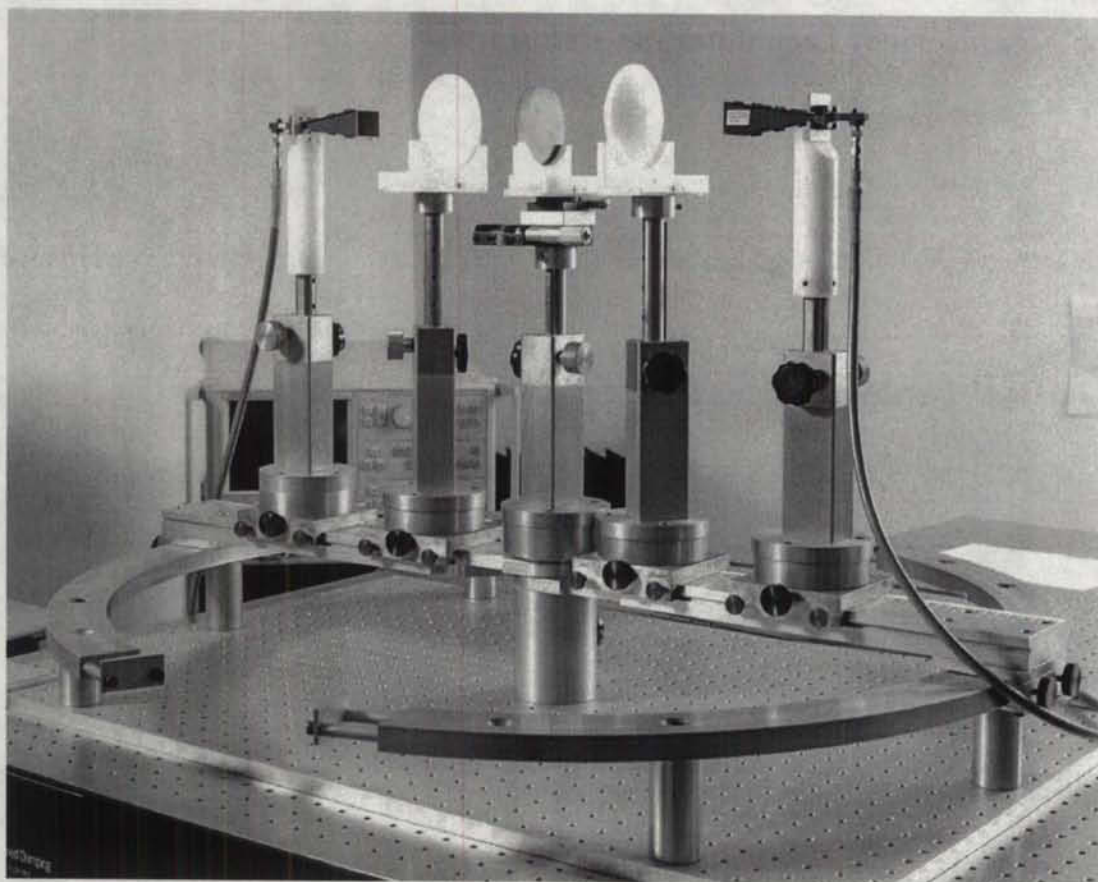
(a)
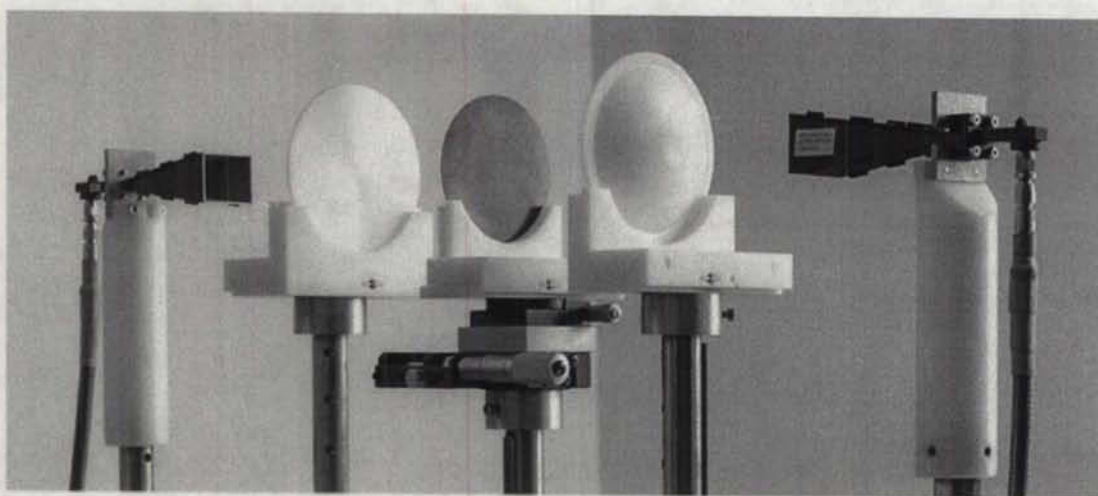
(b)

Figure 3.6: Pictures of the quasi-optical measurement system (a) Overall view; (b) RF components.

Calibration processes can be separated in two main groups: standard calibration and self-calibration. The standard calibration technique is also known as short-open-load-through (SOLT) calibration. It is the most common type of calibration, however it offers less accuracy because more standards have to be measured and, as the frequency increases, the short and open standards are difficult to define because of the increasing effect of parasitic inductances and capacitances [26]. Self-calibration techniques use a different approach based on the information obtained from transmission lines rather than discrete standards [27]. The advantage over the SOLT method is that less standards are used.

Different types of self-calibration exists, but essentially they can be summarised as through-reflect-line (TRL) calibration and through-reflect-match (TRM) calibration. TRL calibration requires two different lengths of transmission lines (through and line) and a high-reflection standard (reflect), normally an open-circuit line, but a short-circuit line is also possible. The difference between the two lengths of line must be around a quarter wavelength, therefore the TRL is bandwidth limited [27]. The bandwidth can be extended if necessary by using more than two lengths of line. In many applications, like on-wafer probe systems [26], the equipment used to measure devices does not allow movement of the ports, which makes the TRL calibration unsuitable. TRM calibration uses a single line (through) and a reflective standard (reflect), but the major difference over TRL is the use of a match standard, which has the benefit of not limiting the bandwidth and allowing fixed locations of the ports.

In the current measurement system, the free-space quasi-optical link has to be calibrated. Most of the free-space measurement systems reported [19, 20, 24, 25] are calibrated using a TRL method. The main reason appears to be that SOLT calibration is

47

difficult to perform in free space since the open standard has to be created artificially using periodic structure technology, in which case the standard is very narrowband.

Using TRL calibration means one of the horn-fed lenses has to be moved by a distance of about a quarter wavelength. This is not a viable approach in the current measurement system, where the location of the components can be measured with a precision of only about 1 mm which, at 30 GHz, represents a tenth of a wavelength. This uncertainty in position would result in large phase errors and would lead to an incorrect calibration. Thus, the TRM calibration method is used for this quasi-optical measurement system since the method does not require any of the components to be repositioned during the calibration process.

3.5.3 TRM Calibration

The TRM calibration requires three standards. For each standard, four parameters can be recorded:

- forward reflection coefficient, S_{11};

- forward transmission coefficient, S_{21};

- reverse transmission coefficient, S_{12};

- reverse reflection coefficient, S_{22}.

Therefore, the total number of parameters from the standards in the calibration process is 12. This yields a system of 12 equations to be solved. However, the error model for self-calibration problems is usually described as two two-port error adapters connected on each side of the device under test [28]. This means each error adapter contains four parameters, for a total of eight parameters. Thus, only eight equations are required to solve the system

of equations, so that eight parameters of the standards are sufficient to fully calibrate the system. The resulting self-calibration eight-term error model contains as much information as a standard-calibration 10-term error model [29], i.e. a standard-calibration with excluded isolation. In other words, the standard-calibration 10-term model can be derived from the self-calibration error model.

For one of the standards, it was shown that all four parameters must be known [28]. This is usually done for the through standard as it is the simplest of all. For the others, only the reflection coefficients (S_{11} and S_{22}) are recorded. One of the standards is a reference to the characteristic impedance, therefore the reflection coefficients must be low [28]. In this case, a match standard is used. The last standard must present a high impedance mismatch, so a highly reflective device is used [28].

Many calibration algorithms have been proposed for TRM calibration. In particular, it was shown [28] that only seven parameters could be used rather than eight to calibrate the system because of the correlation between the two error adapters. For the calibration of the quasi-optical measurement system, the algorithms used are those of the network analyser [30] and require eight parameters to be measured.

3.5.4 Calibration Standards and Procedure

Since self-calibration techniques are normally used for planar circuits, the planar standards have to be transformed into free-space standards. The through standard simply corresponds to free-space transmission. The reflect standard is realised using a polished aluminium plate of diameter equal to the diameter of the samples to be tested and thickness equal to 1.34 mm. Aluminium was preferred over other metals because it is highly

conductivity, low-cost, easy to machine and commonly unaffected by oxide. The thickness of the plate is accounted for in the calibration process. The match standard is made of cone-shaped microwave absorbing material from Resin Systems Corporation. The cones have a length of 45 mm and they are backed by a flat sheet of absorbing material of thickness equal to 13 mm. Again, the diameter of this standard is the same as the one of the samples to be measured. Figure 3.7 shows the standards used in the TRM calibration.

To verify the quality of the standards used, their performance was measured at 30 GHz. First, the return loss of a simple horn-fed lens was measured to be 18.5 dB. Second, the other horn-fed lens was placed so that the measurement system is formed (see

(a)

(b)

t

(c)
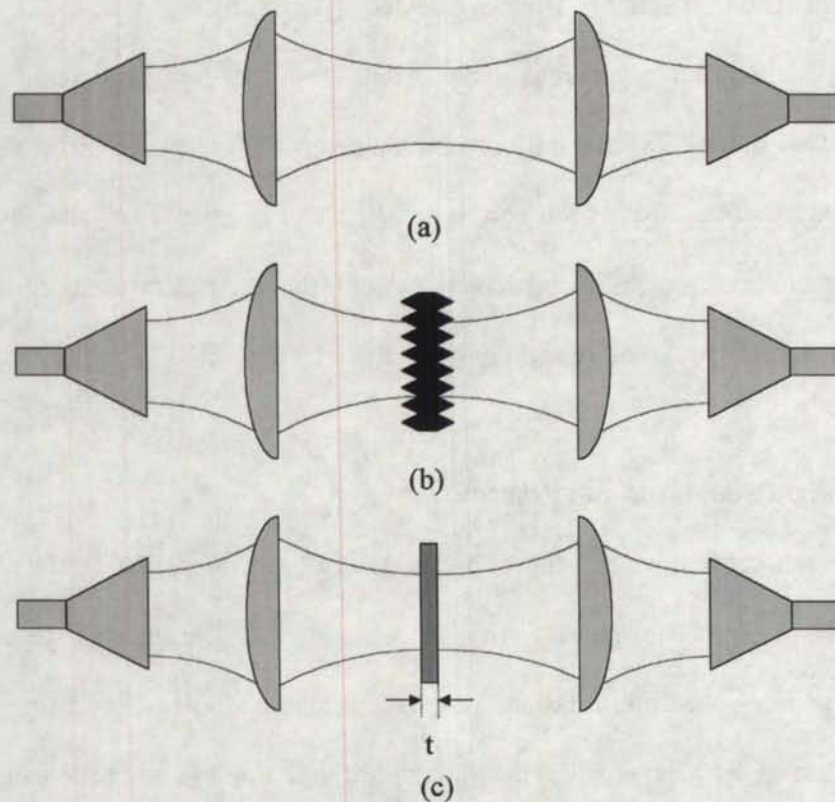
Figure 3.7: Calibration standards (a) Through: no standard applied; (b) Match: absorber cones; (c) Reflect: metal plate.

Figure 3.7a), in which case the return loss was found to be 13.3 dB, which is still acceptable as it does not degrade the match considerably. Third, when the match standard was applied (see Figure 3.7b), the return loss was 18.1 dB. This shows that the match standard is efficient as the return loss obtained is almost identical to the result for the single horn-fed lens. Finally, when inserting the metal plate (see Figure 3.7c), a return loss of 3.7 dB was obtained, which corresponds to a satisfyingly high mismatch to conclude that the aluminium plate is a good reflect standard.

The transmission coefficient of each standard with calibration at the input of the horn antennas was also measured. The through standard showed a transmission coefficient of −3.7 dB, which indicates that almost half the power launched by one of the feed horn is received at the other end. This is a satisfyingly high value, which is similar to the reflection coefficient when the reflect standard is applied. Moreover, the transmission coefficient for the reflect and match standards is below −30 dB, which is quite low and shows that not much power is transmitted when these standards are applied.

Table 3.6 summarises the previous results. In addition, results of the standards obtained after TRM calibration of the measurement system are also presented. These results reveal a dynamic range better than 50 dB for the reflection coefficients and 29 dB for the transmission coefficient.

Table 3.6: Calibration standards results.

Calibration Standard	Standard calibration at horn input		Free-space TRM calibration	
	Reflection (S_{11})	Transmission (S_{21})	Reflection (S_{11})	Transmission (S_{21})
Through	-13.3 dB	-3.7 dB	< -50 dB	~ 0 dB
Reflect	-3.7 dB	-33.5 dB	-0.3 dB	-29 dB
Match	-18.1 dB	-37.2 dB	< -50 dB	-34 dB
One port	-18.5 dB	-	-	-

51

CHAPTER 4 Misalignments in Quasi-Optical Measurement System

4.1 Introduction

In setting up a quasi-optical test bench, accuracy of alignment is an important issue since small misalignments can result in an appreciable loss of power, which might lead to inaccurate results. This chapter presents a study of misalignment in the quasi-optical test bench which expands upon the work published in [31]. One of the main objectives is to investigate the degree of sensitivity of each component of the setup. The analysis is based on the Gaussian beam coupling formulation presented in Chapter 2.

4.2 Structural Design

Precision equipment designed for optical applications, providing alignment accuracy of the order of micrometres, is available. Since the test bench is designed to operate in the millimetre wave frequency band, the structural design should be a compromise between the structural complexity, which has cost implications, and the tolerable misalignment level. As a low cost and flexible alternative, the quasi-optical test bench was initially fabricated with a mechanical precision of the order of millimetres.

However, such a precision may not be sufficient for some components of the measurement system. Therefore, it is necessary to know which components are most sensitive to misalignments and where the structure should be enhanced to maintain an acceptable level of performance. Also, no strict precaution is needed for less critical

misalignments such that complexity and cost are reduced. In other words, the objective is to design the test bench to minimise misalignment errors that can most degrade its performance.

4.3 Study of Misalignments

4.3.1 Types of Misalignments

The study of misalignments involved the analysis of three types of misalignments: tilt, axial and transverse offset. Figure 4.1 shows these different types of misalignments for a component of the test bench assuming propagation in the z direction. These misalignments are:

− Δx: transverse offset in x;

− Δy: transverse offset in y;

− Δz: axial offset (in z);

− θ_{xz}: tilt in xz plane (yaw);

− θ_{yz}: tilt in yz plane (pitch).

The tilt in the xy plane (roll) is not considered since it is not related to the Gaussian beam coupling, but rather to the polarisation mismatch. Furthermore, this tilt is negligible in the setup.

4.3.2 Occurrence of Simultaneous Misalignments

The Gaussian beam analysis presented in this section is based on previously published material [8, 31, 32]. The objective of this section is to develop knowledge on the combination of multiple misalignments of different types occurring at the same time.
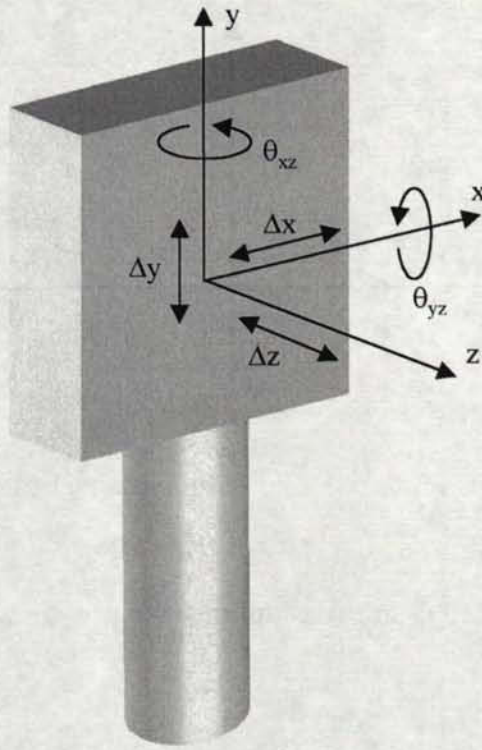
Figure 4.1: Possible misalignments of a component of the quasi-optical test bench.

A one-dimensional Gaussian beam distribution as defined by (2-31) is first considered. Along x, two types of misalignments are possible: transverse offset, Δx, and tilt, θ_{xz}. The transverse offset affects directly the variable x; the tilt introduces a distance shift in the direction of propagation, which can be converted into a phase shift [33]. Figure 4.2 shows the tilt of two coupling Gaussian beam. From this figure,

$$z = x \sin \theta_{xz},$$ (4-1)

and the phase shift introduced is

$$\Delta \phi = k_0 z = \frac{2\pi}{\lambda_0} z.$$ (4-2)
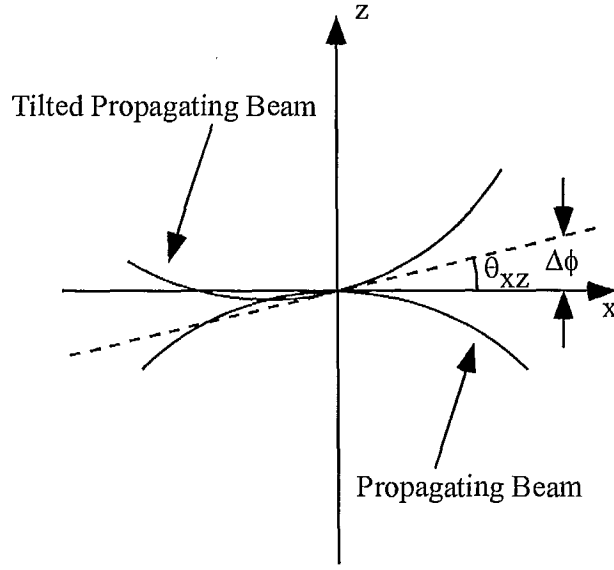
Figure 4.2: Tilt of two coupling beams in the xz plane.

Substituting (4-1) into (4-2):

$$\Delta\phi = \frac{2\pi}{\lambda_0} x \sin\theta_{xz} , \qquad (4\text{-}3)$$

and for small angles:

$$\Delta\phi \cong \frac{2\pi}{\lambda_0} x \theta_{xz} . \qquad (4\text{-}4)$$

Therefore, (2-31), assuming misalignments, can be rewritten as

$$u(x) = \left(\frac{2}{\pi w_x^{\,2}}\right)^{0.25} \exp\left(-\frac{(x-\Delta x)^2}{w_x^{\,2}} - j\frac{\pi(x-\Delta x)^2}{\lambda_0 R_x}\right) \exp\left(-j\frac{2\pi}{\lambda_0}x\theta_{xz}\right), \qquad (4\text{-}5)$$

and we can apply (2-32) to obtain the field coupling coefficient:

$$c_{ab}^{1x} = \int_{-\infty}^{\infty}\left\{\left[\left(\frac{2}{\pi w_{xa}^{\,2}}\right)^{0.25} \exp\left(-\frac{(x-\Delta x_a)^2}{w_{xa}^{\,2}} + j\frac{\pi(x-\Delta x_a)^2}{\lambda_0 R_{xa}} + j\frac{2\pi}{\lambda_0}x\theta_{xza}\right)\right]\right.$$

$$\cdot \left[\left(\frac{2}{\pi w_{xb}^{\ 2}} \right)^{0.25} \exp \left(-\frac{(x - \Delta x_b)^2}{w_{xb}^{\ 2}} - j \frac{\pi (x - \Delta x_b)^2}{\lambda_0 R_{xb}} - j \frac{2\pi}{\lambda_0} x \theta_{xzb} \right) \right] \right\} dx . \qquad (4\text{-}6)$$

Reorganising (4-6):

$$c_{ab}^{1x} = \left(\frac{2}{\pi w_{xa} w_{xb}} \right)^{0.5} \int_{-\infty}^{\infty} \exp \left\{ -x^2 \left[\frac{1}{w_{xa}^{\ 2}} + \frac{1}{w_{xb}^{\ 2}} + j \frac{\pi}{\lambda_0} \left(\frac{1}{R_{xb}} - \frac{1}{R_{xa}} \right) \right] \right.$$

$$+ 2x \left[\left(\frac{\Delta x_a}{w_{xa}^{\ 2}} + \frac{\Delta x_b}{w_{xb}^{\ 2}} \right) - j \frac{\pi}{\lambda_0} \left(\frac{\Delta x_a}{R_{xa}} - \frac{\Delta x_b}{R_{xb}} + \theta_{xzb} - \theta_{xza} \right) \right]$$

$$- \left[\left(\frac{\Delta x_a^{\ 2}}{w_{xa}^{\ 2}} + \frac{\Delta x_b^{\ 2}}{w_{xb}^{\ 2}} \right) - j \frac{\pi}{\lambda_0} \left(\frac{\Delta x_a^{\ 2}}{R_{xa}} - \frac{\Delta x_b^{\ 2}}{R_{xb}} \right) \right] \right\} dx . \qquad (4\text{-}7)$$

Knowing that [33]:

$$\int_{-\infty}^{\infty} \exp \left(-ax^2 - 2bx - c \right) dx = \left(\frac{\pi}{a} \right)^{0.5} \exp \left(\frac{b^2}{a} - c \right),$$

the solution of (4-7) leads to the following result:

$$c_{ab}^{1x} = \left[\frac{2}{\left(\frac{w_{xb}}{w_{xa}} + \frac{w_{xa}}{w_{xb}} \right) + j \frac{\pi w_{xa} w_{xb}}{\lambda_0} \left(\frac{1}{R_{xb}} - \frac{1}{R_{xa}} \right)} \right]^{0.5}$$

$$\cdot \exp \left\{ \frac{\left[\left(\frac{\Delta x_a}{w_{xa}^{\ 2}} + \frac{\Delta x_b}{w_{xb}^{\ 2}} \right) - j \frac{\pi}{\lambda_0} \left(\left(\frac{\Delta x_a}{R_{xa}} - \frac{\Delta x_b}{R_{xb}} \right) + \left(\theta_{xzb} - \theta_{xza} \right) \right) \right]^2}{\left(\frac{1}{w_{xa}^{\ 2}} + \frac{1}{w_{xb}^{\ 2}} \right) + j \frac{\pi}{\lambda_0} \left(\frac{1}{R_{xb}} - \frac{1}{R_{xa}} \right)} \right\}$$

$$\cdot \exp \left[-\left(\frac{\Delta x_a^{\ 2}}{w_{xa}^{\ 2}} + \frac{\Delta x_b^{\ 2}}{w_{xb}^{\ 2}} \right) + j \frac{\pi}{\lambda_0} \left(\frac{\Delta x_a^{\ 2}}{R_{xa}} - \frac{\Delta x_b^{\ 2}}{R_{xb}} \right) \right] . \qquad (4\text{-}8)$$

Equation (4-8) is a very important result that dictates the occurrence of simultaneous misalignments. The same derivation can be performed in y, which will produce a similar result. If no misalignments are present, only the term in front of the exponential remains and the same result as (2-34) is obtained.

Note that even though the axial offset Δz does not appear directly in the coupling equation, it is accounted for through the parameters of each beam, i.e. w and R. Those two parameters are functions of distance z, as shown by equations (2-10) and (2-11), so that if that distance is varied through the axial offset Δz, the beam radius and radius of curvature are modified accordingly to take into account this variation in the calculation of the power coupling factor.

4.4 Results

Results were simulated with Mathcad [34], in which all five types of misalignment shown in Figure 4.1 can be varied for all four components of the test bench, leading to the total power coupling factor as the final result. The parameters of the feed horns and focusing lenses can also be varied so that Mathcad can be used for any two-port quasi-optical test bench with the same configuration.

The power coupling factor calculation is performed between any two adjacent components of the test bench, i.e. between horn 1 and lens 1; lens 1 and lens 2; and lens 2 and horn 2. This leads to three intermediate power coupling factors, which are then multiplied to give the total power coupling factor for the entire test bench:

$$K = K_{horn1,lens1} K_{lens1,lens2} K_{lens2,horn2} . \tag{4-9}$$

Knowing that the test bench is symmetrical, a given misalignment in horn 1 gives the same total power coupling factor K as if it occurred on horn 2. The same applies for lens 1 and lens 2. Also, since the beam waist radius is symmetrical, similar misalignments in the x and y directions create the same power coupling factor in both dimensions.

In order to compare the simulated results with experimental results, measurements were obtained using a microwave source connected at one of the feed horns while a power meter was connected to the other. Misalignments were then introduced in the test bench and the resulting power variation was measured.

Experimental and theoretical results for certain misalignments are given in Figures 4.3 to 4.8: Figure 4.3 presents the transverse offset of a horn; Figure 4.4 presents the transverse offset of a lens; Figure 4.5 presents the tilt of a horn; Figure 4.6 presents the tilt of a lens; Figure 4.7 presents the axial offset between a horn and a lens and; Figure 4.8 presents the axial offset between the lenses. Furthermore, each figure shows an illustration of the corresponding misalignment.

The theoretical results (labelled *theoretical*) were determined using the parameters of the beam reported in Chapter 3, which are summarised in Table 4.1. However, it was found that these results do not agree as expected with the experimental results for some misalignments: in the case of transverse offsets (see Figures 4.3 and 4.4), the difference between experimental results and theory can be as high as 1 dB.

Table 4.1: Beam parameters of the horn-lens arrangement.

Parameter	Symbol	Value (mm)
Input beam waist radius	w_{in}	11
Output beam waist radius	w_{out}	26.91
Focal length	f	93
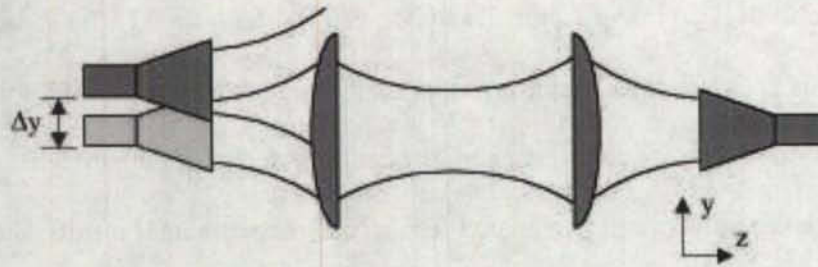
(a)
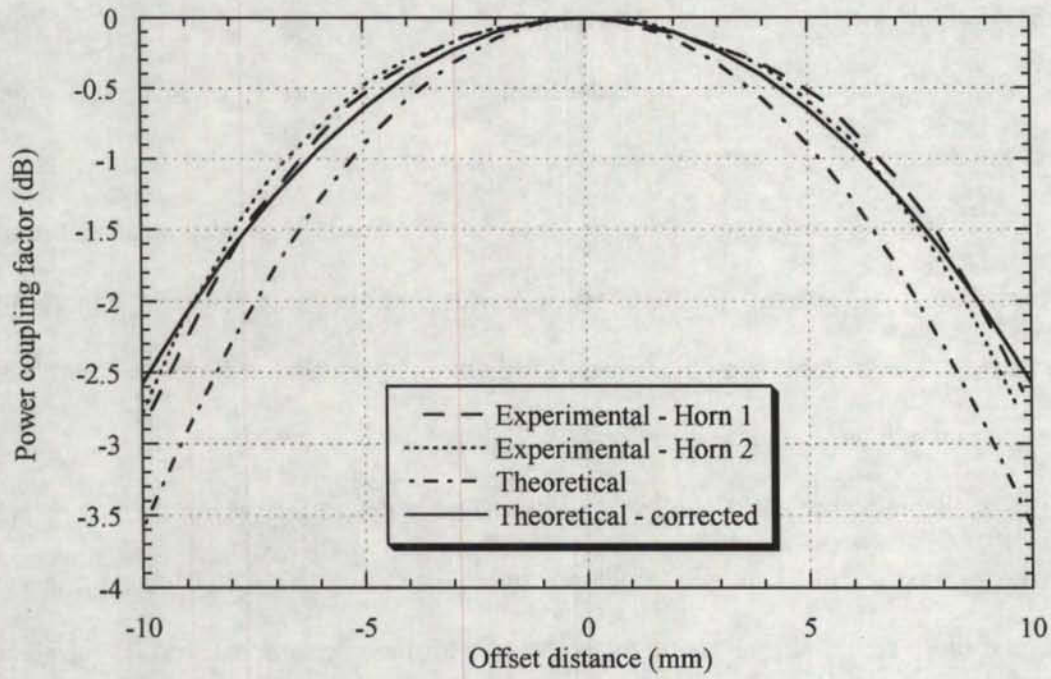
(b)

Figure 4.3: Transverse offset of horn in *y* (a) misalignment illustration; (b) total power coupling factor versus offset distance.
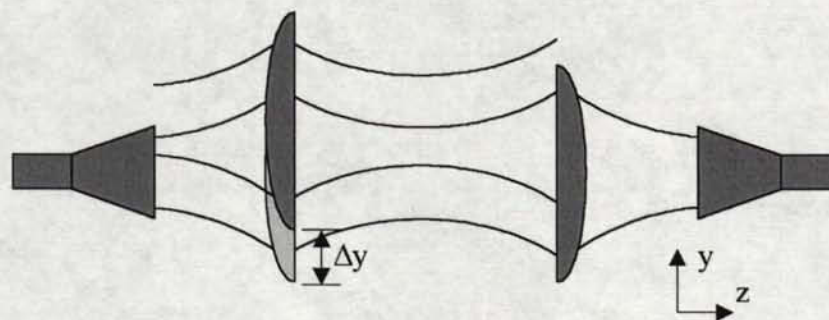
(a)
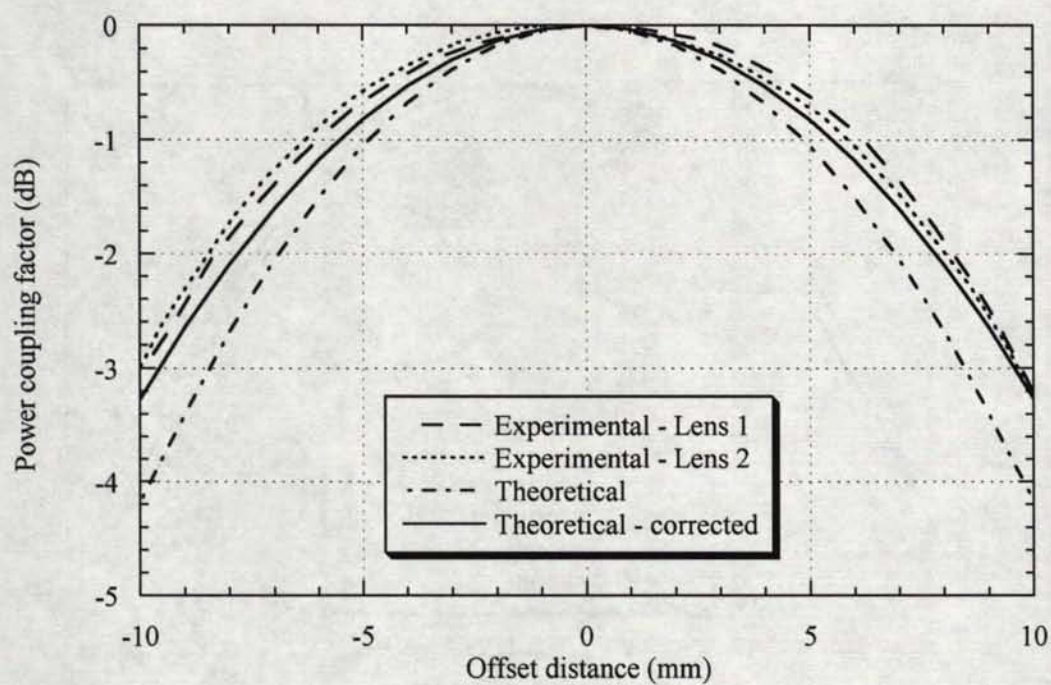
(b)

Figure 4.4: Transverse offset of lens in *y* (a) misalignment illustration; (b) total power coupling factor versus offset distance.
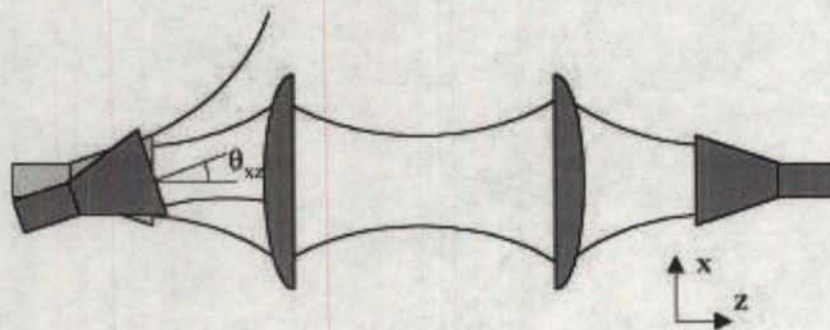
(a)
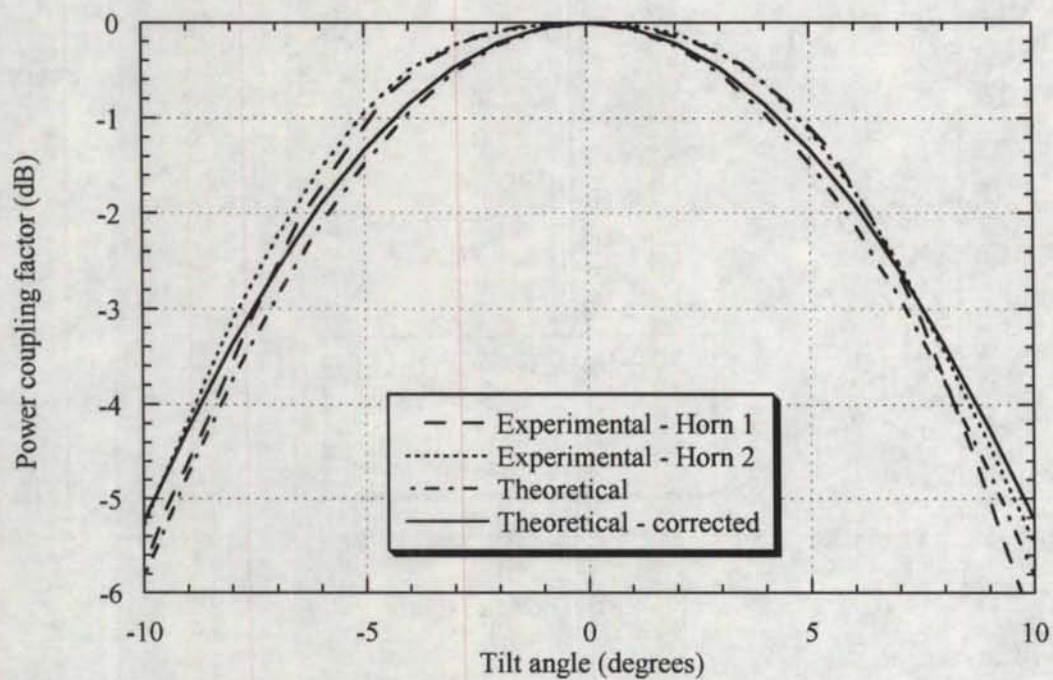
(b)

Figure 4.5: Tilt of horn in *xz* plane (a) misalignment illustration; (b) total power coupling factor versus tilt angle.
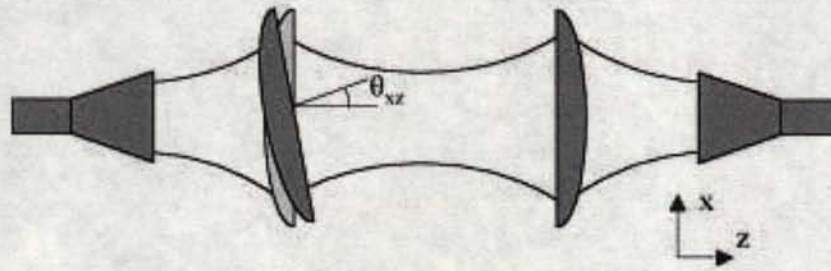
(a)
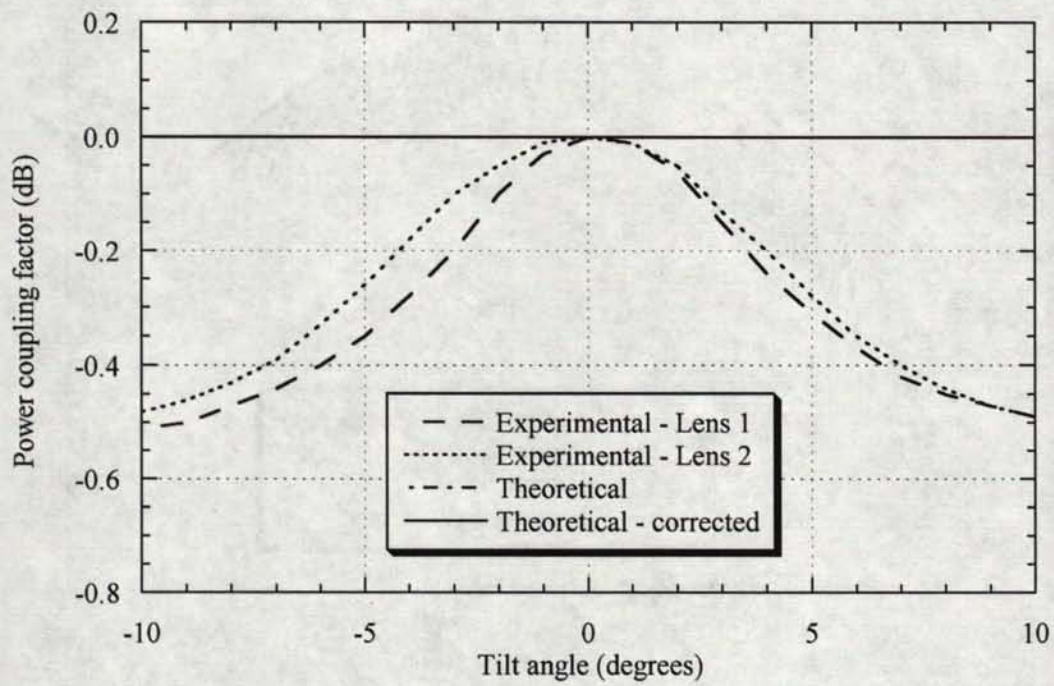
(b)

Figure 4.6: Tilt of lens in *xz* plane (a) misalignment illustration; (b) total power coupling factor versus tilt angle.
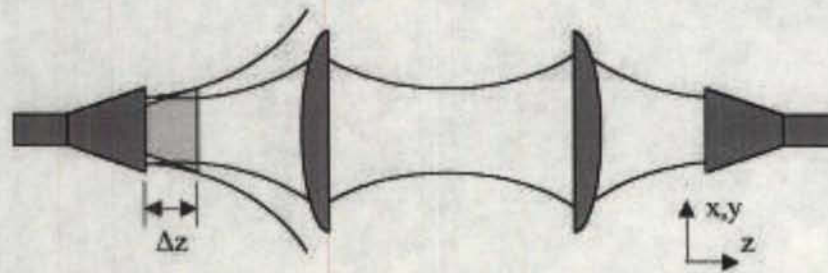
(a)
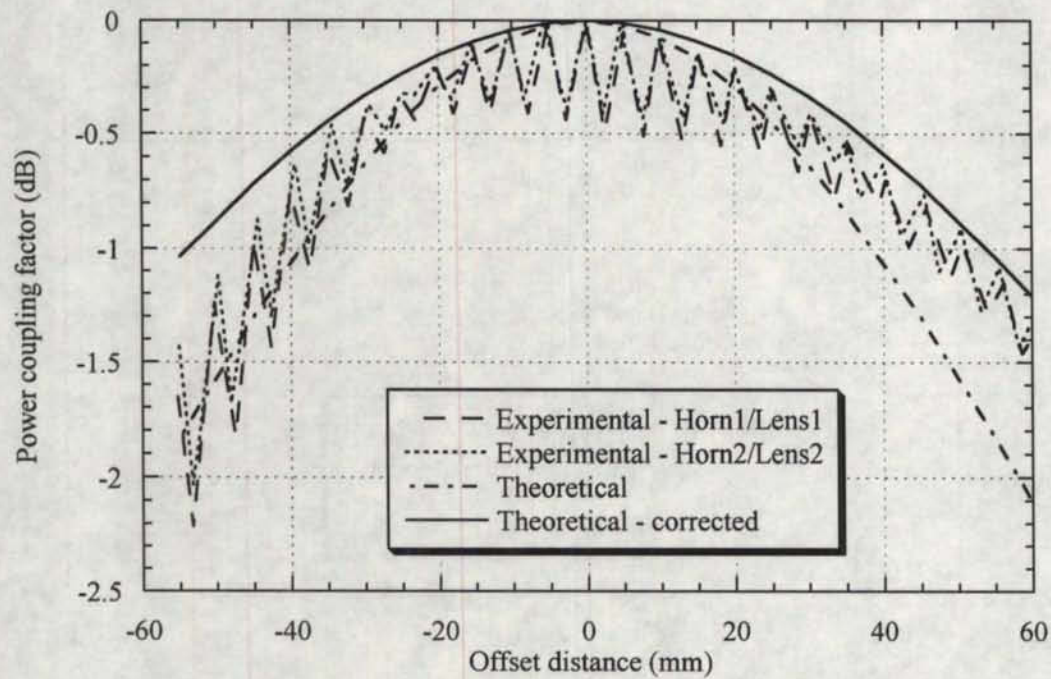
(b)

Figure 4.7: Axial offset between horn and lens (a) misalignment illustration; (b) total power coupling factor versus offset distance.
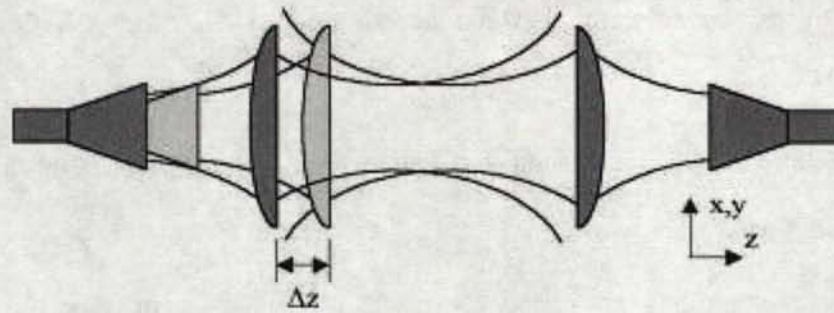
(a)
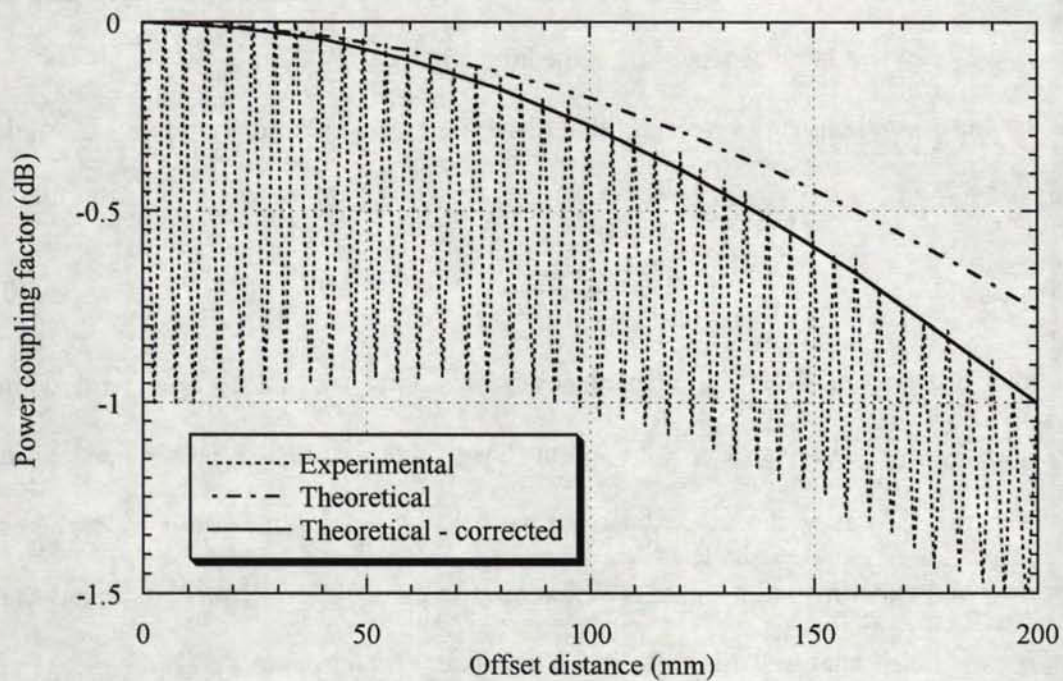
(b)

Figure 4.8: Axial offset between lenses (a) misalignment illustration; (b) total power coupling factor versus offset distance.

In an attempt to improve agreement between theory and experimentation, the parameters of the beam were modified according to [15]. In [15], the following observations are made:

− the Gaussian beam method using thin lens or thick lens models is not accurate for lenses with f/D ratios around 1;

− the thin lens approximation breaks down when the input beam waist is located at a distance smaller than $1.5\,D$ from the lens;

− the beam size of a horn with a fundamental Gaussian beam is about 20% larger than the measured beam at large distances from the horn aperture.

The first and second observations imply that (2-25) is no longer valid, therefore we should write:

$$f \cong \frac{\pi w_{in} w_{out}}{\lambda}. \qquad (4\text{-}10)$$

The third observation reveals a discrepancy between theory and measurement while applying (2-19). The value of the input beam radius waist was obtained from measurement. However, the third statement says that, for the same beam waist radius, theoretical and experimental beams are different at large distances. Since the theoretical beam is used in the analysis, this value is not accurate. Therefore, to match the measured beam with the fundamental beam, the value of the input beam waist radius should be increased by 20%. This will have the effect of decreasing the fundamental beam at large distance by the same amount, which will match the theoretical and experimental values at large distances. We then obtain a new value of input beam waist radius of 13 mm instead of 11 mm. From (4-10), increasing the input beam waist radius will have the effect of

Table 4.2: Corrected beam parameters of the horn-lens arrangement.

Parameter	Symbol	Value (mm)
Input beam waist radius	w_{in}	13
Output beam waist radius	w_{out}	25
Focal length	f	93

reducing the output beam waist radius, but not by the same amount. The value of the output beam waist is then set to 25 mm. Note that the focal length of the lens is unchanged from the design value, as observed in [35]. These beam parameters, referred to as corrected beam parameters, are presented in Table 4.2. The theoretical results obtained with the corrected beam parameters (labeled *theoretical - corrected*) are also plotted in Figures 4.3 to 4.8.

4.5 Discussion

Analysis of Figures 4.3 to 4.8 reveals that the corrected beam parameters result in a better agreement with measured values than the uncorrected ones, as was expected. In each case, the misalignment introduced for opposite components is nearly identical, which confirms the symmetry of the test bench.

The transverse offset of either the horn or the lens was found to be about the same. Typically, a loss of 3 dB or less was observed for an offset of 10 mm. The tilt of a horn was found to be a very sensitive parameter, where a loss of 5 dB to 6 dB was observed at an angle of 10°. Theoretically, using the thin lens approximation or ideal components, the tilt of a lens should not introduce any loss in the system. Experimentally, a loss of about 0.5 dB was observed at about 10°, which can be explained by the fact that the effective area of the lens is reduced.

The axial offset between horn and lens leads to ripples in the experimental patterns. The theoretical equations do not take into account this phenomenon, which is explained by a simple standing wave present between the horn and lens due to wave impedance mismatch at the surface of the lens. The standing wave is caused by reflection of the power, which combines in-phase or out-of-phase, and creates ripples. According to standing wave theory, the ripples should be of period equal to half a wavelength, in this case 5 mm, which is what we observe here. As the horn is moved away from the lens (positive offset), the experimental curves follow well the corrected theoretical curve. However, as the horn is moved closer to the lens (negative offset), the experimental curves decrease more rapidly than the corrected theoretical curve. This is explained by the fact that less power is transmitted through the lens and more power is reflected as the horn gets closer to the lens. The axial offset between the two lenses presents the same kind of ripples, which again are caused by a standing wave. This time, the standing wave is due to wave reflection between lenses. In both case of axial offset, the fundamental power loss is not significant, but because of the presence of the standing wave, power variation as high as 1 dB can be observed for relatively small misalignments.

This analysis has revealed that care must be taken to ensure the same exact positioning of all the components of the system during an entire measurement session. In some cases, especially for axial misalignments, major power variations as high as 1 dB can occur by moving some components by only a quarter wavelength, i.e. 2.5 mm (see Figure 4.8). However, if the measurement system is calibrated with slight misalignments and if those misalignments remain constant during the entire measurement process, the errors should be insignificant since the misalignments are accounted for by the calibration

process. Therefore, the component precision of the test bench structure seems to be acceptable and, in order to reduce the overall cost, no modifications were made.

In conclusion, a more complete study of the misalignments in a quasi-optical test bench could be conducted, taking into account efficient thick lens modeling and multimode Gaussian beam analysis. However, it is believed that such an analysis would be extremely complex and unnecessary if one is only interested in a general behavior of misalignments. A simple Gaussian optics, single mode analysis is sufficient to give a good estimate.

CHAPTER 5 Dielectric Material Properties Determination

5.1 Introduction

A complete procedure for determining the dielectric constant of materials from S-parameters measured with the calibrated quasi-optical measurement system is presented in this chapter. Two correction terms are introduced to compensate for errors caused by the lateral misplacement of the sample and by the calibration procedure. Algebraic and numerical extraction techniques are presented. This chapter provides details about the work published in [36].

5.2 Preliminary Measurements

Using the previously described apparatus, S-parameters of a few samples were measured. The measured samples were low-permittivity materials with thickness between 0.5 mm and 3 mm. It was observed that many ripples of large amplitude are present when measuring from 28 GHz to 32 GHz. This is not a surprise since such ripples, which are caused by a standing wave between the lenses, have already been observed when changing the lens separation in Chapter 4 (axial offset). In this case, the separation between the lenses is not changed, however introducing a sample of dielectric constant greater than one has the effect of changing the overall electrical length between the lenses, which is similar to changing the distance between the lenses. Unfortunately, there is no easy means to compensate for such ripples because it is a broadband measurement, i.e. the electrical length varies with the frequency.

The amplitude of the ripples can easily be lowered if the wave impedance mismatch at the lens interface is reduced. One way to reduce the wave impedance mismatch is to use lenses with lower dielectric constant. Typically, the lens dielectric constant is preferred to be between 2 and 3, because a lower dielectric constant (1-2) requires fairly thick lenses and high dielectric constant (higher than 3) increases the mismatch.

Figures 5.1 and 5.2 present the magnitude and phase of the reflection and transmission coefficients for a sheet of GML 1000 with dielectric constant of 3.05 and thickness of 0.508 mm. In these figures, large ripples are present in both magnitude and phase of reflection and transmission coefficients for Plexiglas lenses. The magnitude of the ripples can be as high as 2 dB for the reflection coefficient and almost 1 dB high for the transmission coefficient, whereas the phase drift is almost 20° for the reflection coefficient and 5° for the transmission coefficient.

The Plexiglas lenses used have a dielectric constant around 2.56. In order to reduce the wave impedance mismatch at the lens interface, new lenses with lower dielectric constant were fabricated. The material used was Tivar 1000 with a typical dielectric constant of 2.3. The design of these lenses is presented in Appendix B. Table 5.1 summarises the parameters of the Tivar lens.

Table 5.1: Parameters of the Tivar focusing lens.

Parameter	Symbol	Value
Focal length (mm)	f	90.00
Diameter (mm)	D	77.65
Thickness (mm)	T	13.62
Dielectric constant	ε_r	2.3
Edge taper (dB)	T_e	20
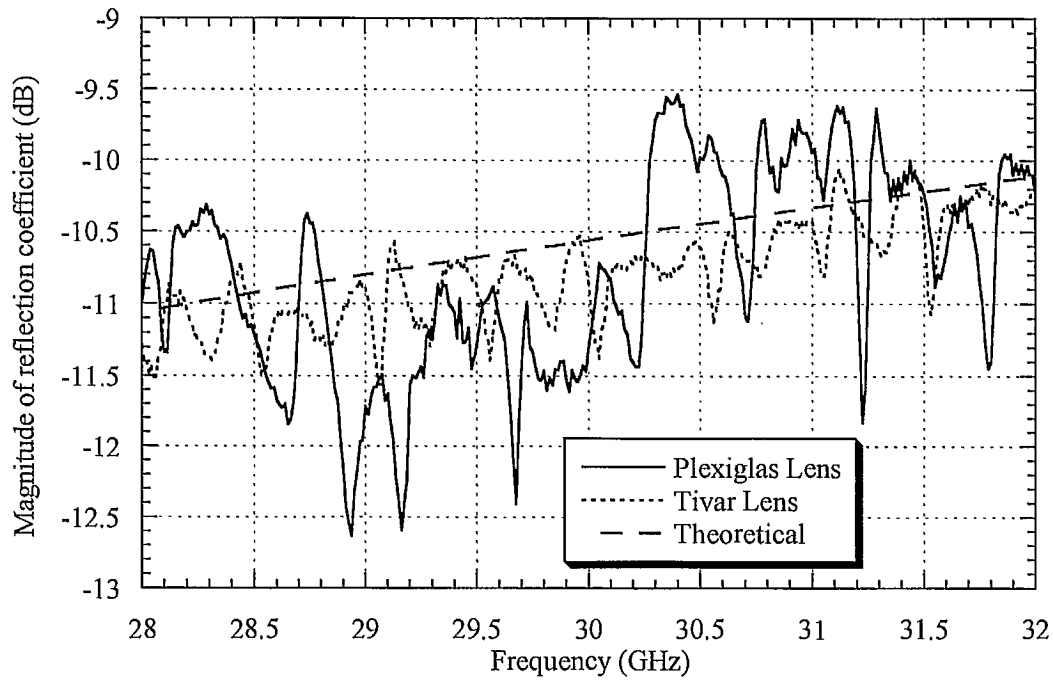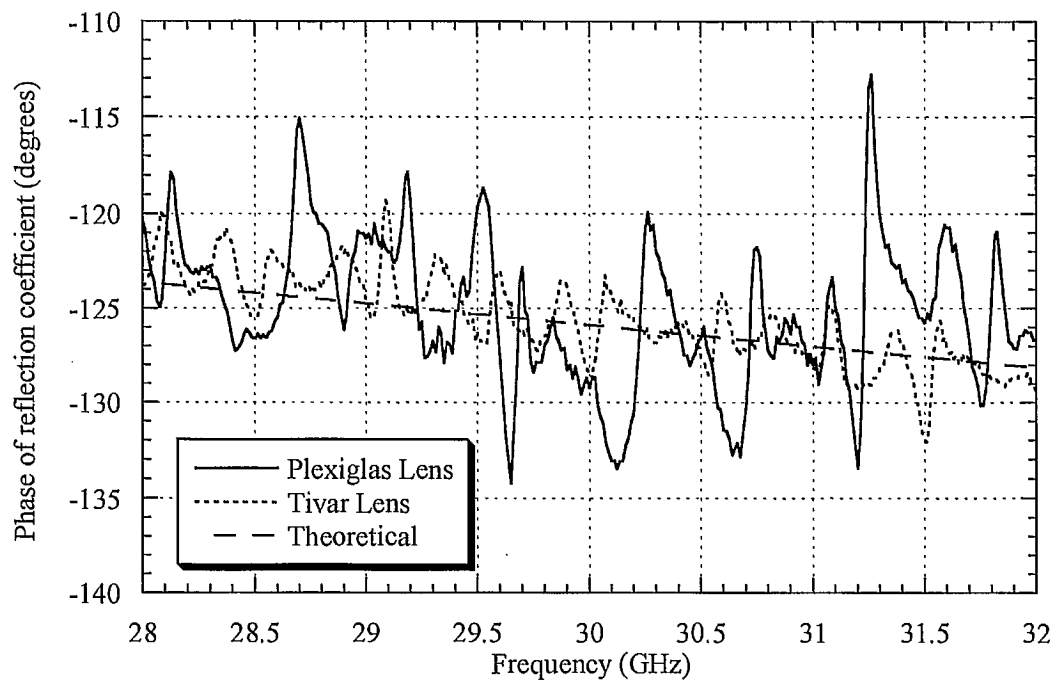
Figure 5.1: Comparison of reflection coefficient of 0.508-mm GML 1000 using Tivar lens and Plexiglas lens (a) magnitude; (b) phase.
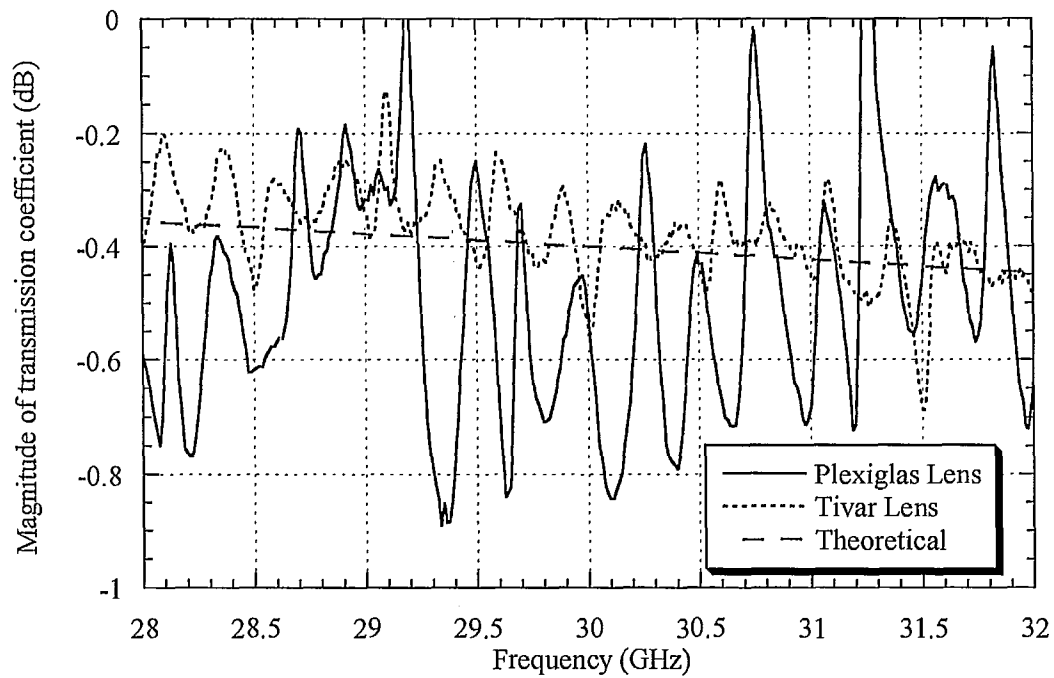
(a)
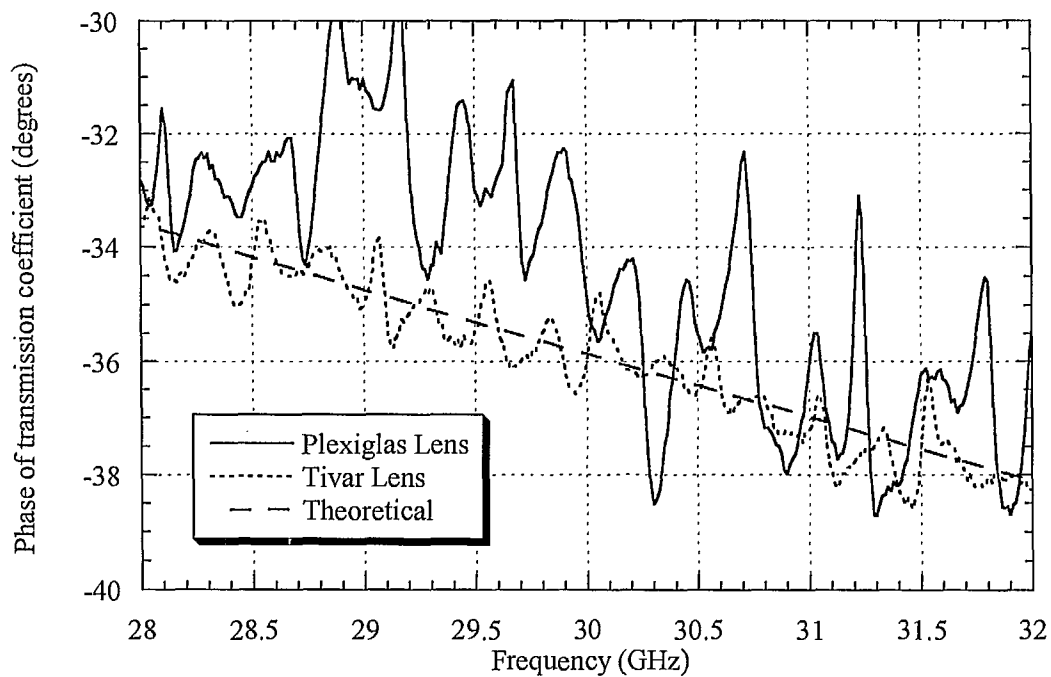
(b)

Figure 5.2: Comparison of transmission coefficient of 0.508-mm GML 1000 using Tivar lens and Plexiglas lens (a) magnitude; (b) phase.

With the Tivar lenses, Figures 5.1 and 5.2 show that the amplitude of the ripples is lower in every case. The magnitude of the ripples is less than 1 dB for the reflection coefficient and less than 0.3 dB for the transmission coefficient. In the case of the phases, the drift angle is about 5° for the reflection coefficient and about 2° for the transmission coefficient.

Finally, note that, in order to provide comparison between measurements taken with the two different lenses, the correction terms presented in section 5.4.2 and section 5.4.3 have been applied in the results of Figures 5.1 and 5.2.

5.3 Normal Plane Wave on Dielectric Slab

In order to characterise materials using the free-space approach, the S-parameters of the sample under test are required. As discussed in Chapter 3, the quasi-optical test bench is designed to create a Gaussian plane wave at the sample location, which allows plane wave theory to be used in the calculations. In this section, the S-matrix of a sheet of material is derived.

The S-parameters of a sample are represented in Figure 5.3, which are:

- forward reflection coefficient, S_{11};

- forward transmission coefficient, S_{21};

- reverse transmission coefficient, S_{12};

- reverse reflection coefficient, S_{22}.

While measuring passive elements such as a bulk slab of material with a symmetrical measurement system, the scattering matrix should be reciprocal:

$$S_{11} = S_{22} \text{ and } S_{21} = S_{21}.$$ (5-1)
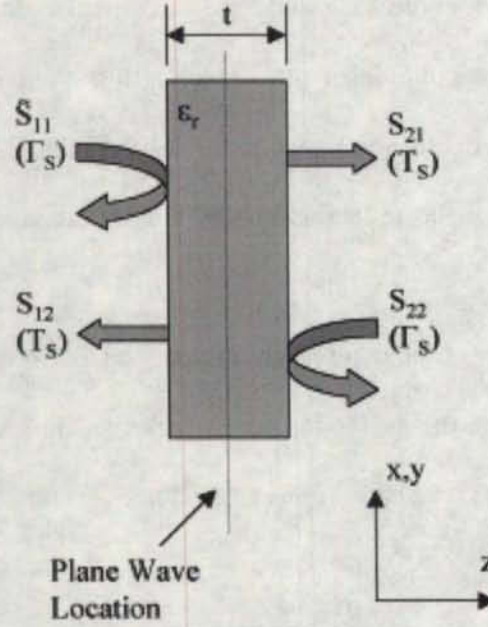
Figure 5.3: S-parameters of a slab of dielectric material.

Therefore, the S-matrix can be written as

$$[S] = \begin{bmatrix} \Gamma_S & T_S \\ T_S & \Gamma_S \end{bmatrix} = \begin{bmatrix} |\Gamma_S|\exp(j\phi_{\Gamma_S}) & |T_S|\exp(j\phi_{T_S}) \\ |T_S|\exp(j\phi_{T_S}) & |\Gamma_S|\exp(j\phi_{\Gamma_S}) \end{bmatrix}, \tag{5-2}$$

where

$$S_{11} = S_{22} = \Gamma_S, \tag{5-3}$$

$$S_{21} = S_{12} = T_S, \tag{5-4}$$

in which case Γ_S and T_S are the reflection and transmission coefficients, respectively. In (5-2), S_{11} and S_{22} are set equal to a value Γ_S; similarly S_{21} and S_{12} are set equal to a value T_S. In addition, both Γ_S and T_S are separated into magnitude and phase components.

Theoretically, both reflection and transmission coefficients are functions of the thickness, complex permittivity and complex permeability of the material. A straight-forward derivation [37] leads to the following results:

$$\Gamma_S = \frac{\Gamma(1-\tau^2)}{1-\Gamma^2\tau^2} \, , \tag{5-5}$$

$$T_S = \frac{\tau(1-\Gamma^2)}{1-\Gamma^2\tau^2} \, , \tag{5-6}$$

where

$$\Gamma = \frac{Z_S - Z_A}{Z_S + Z_A} \, , \tag{5-7}$$

$$\tau = \exp(-\gamma_S t). \tag{5-8}$$

In (5-7), Γ is the reflection coefficient at the air-sample interface, Z_S is the wave impedance in the slab, and Z_A is the wave impedance in free space. In (5-8), τ is the transmission coefficient in the material sample over a distance equal to its thickness, γ_S is the propagation constant in the sample under test, and t is its thickness. Z_S, Z_A and γ_S are defined as follows:

$$Z_S = \sqrt{\frac{\mu}{\varepsilon}} \, , \tag{5-9}$$

$$Z_A = \sqrt{\frac{\mu_0}{\varepsilon_0}} \, , \tag{5-10}$$

$$\gamma_S = j\omega\sqrt{\mu\varepsilon} \, , \tag{5-11}$$

where

$$\varepsilon = \varepsilon_0 \varepsilon_r \, , \tag{5-12}$$

$$\mu = \mu_0 \mu_r \, , \tag{5-13}$$

and ω is the angular frequency. From (5-9) and (5-10), (5-7) simplifies to

$$\Gamma = \frac{\sqrt{\mu_r} - \sqrt{\varepsilon_r}}{\sqrt{\mu_r} + \sqrt{\varepsilon_r}}. \tag{5-14}$$

5.4 Data Smoothing and Correction Techniques

Before applying the extraction process, some processing has to be performed to the recorded S-parameters. This section presents the three processes to be applied, which are data smoothing and two correction terms.

5.4.1 Data Smoothing

As shown in Figures 5.1 and 5.2, many ripples with significant amplitude are present in the S-parameters because of the multiple reflections between the lenses and the sample under test. This is a problem because such reflections alter the S-parameters of the sample under test. To overcome this problem, one would need to perform in-deep modelling of the measurement system in order to compensate for the multiple reflections between the lenses. However, this is a complicated task.

To reduce the ripples amplitude, time-domain gating has been used [17, 19, 23]. Time-domain gating is implemented by performing the inverse Fourier transform of the frequency-domain S-parameters, such that time-domain S-parameters are obtained. Then, a filter in time is applied and S-parameters are re-transformed in the frequency domain by applying a Fourier transform. The filter in time eliminates undesired reflection from a device in the system. For a measurement system like the one presented in this report, time-domain gating could be used to reduce the mismatch and, consequently, the multiple reflections present between the lenses [17]. This has the effect of smoothing the results since it removes the ripples.

However, network analysers with time-domain gating are expensive. Because our equipment was not equipped with such capabilities, other means had to be found in order

to eliminate the ripples. It was shown [25] that accurate results can be obtained without time-domain gating if the beam waist is fairly large compared to a wavelength. Since this is not our case (such highly collimated beams could only be obtained with much larger antennas at Ka band), some processing needs to be applied in order to reduce the ripples.

Knowing that time-domain gating has the effect of smoothing the result, a simple smoothing algorithm was adopted instead of time-domain gating in an attempt to improve the results. The smoothing was performed with Mathcad using a function that first calculates the median of n adjacent points, then its residual, and finally the residual is smoothed using the median technique. According to Mathsoft [34], this type of smoothing algorithm is one of the most robust as it is less affected by spurious data points, which can be present as shown in Figures 5.1 and 5.2.

Smoothed and unsmoothed data is presented in Figures 5.4 and 5.5 for a 0.508-mm sheet of GML 1000 with dielectric constant of 3.05. Comparison with theory reveals that the maximum magnitude difference is about 0.3 dB for the reflection coefficient and less than 0.1 dB for the transmission coefficient whereas the phase difference is less than 2° for the reflection coefficient and less than 0.5° for the transmission coefficient. This is a significant improvement compared to the unsmoothed results. Note that a comparison of smoothed results and results processed with time-domain gating would give a better idea of the performance of the two techniques, however this was not possible since our network analyser is not equipped with time-domain gating. Nevertheless, we conclude that such a smoothing is very efficient and much less expensive compared to time-domain gating.
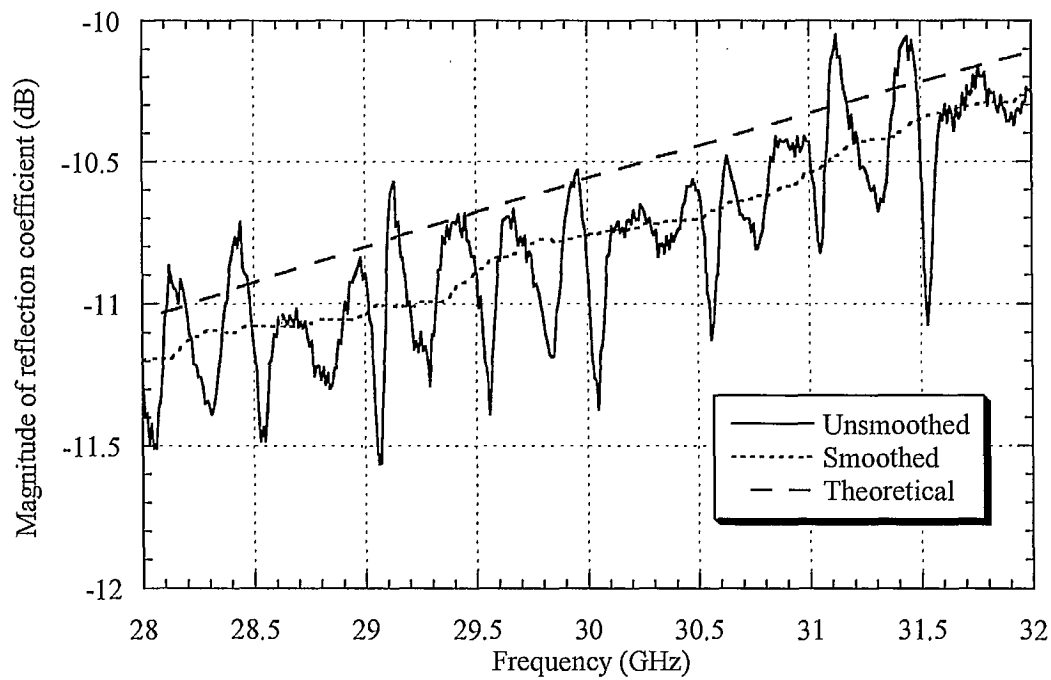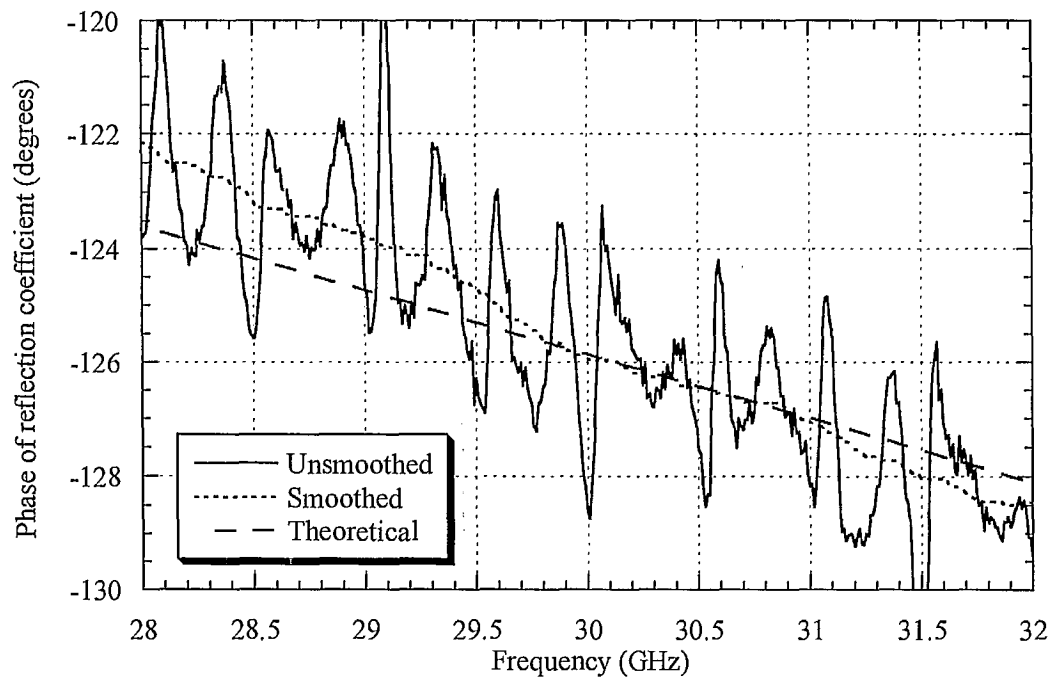
Figure 5.4: Comparison of smoothed and unsmoothed reflection coefficient for 0.508-mm GML 1000 (a) magnitude; (b) phase.
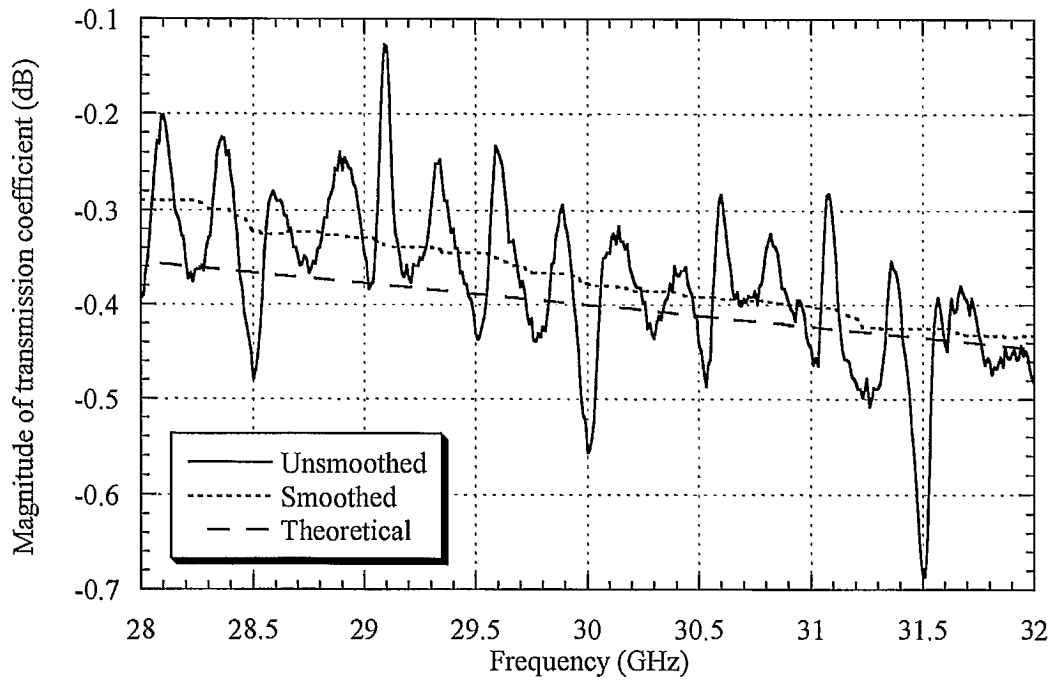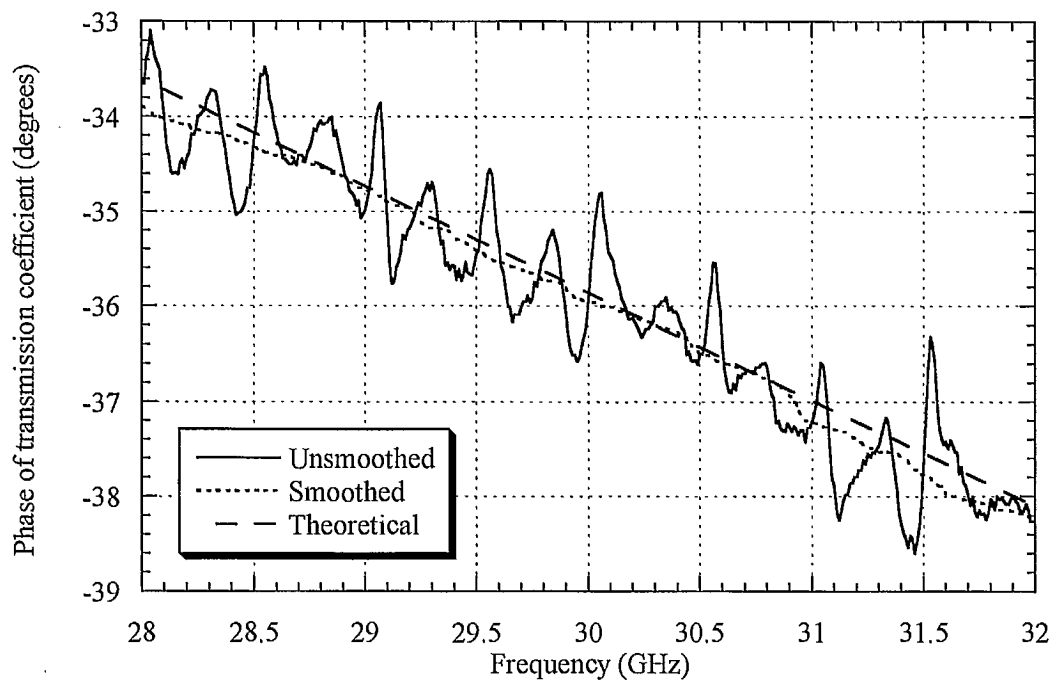
Figure 5.5: Comparison of smoothed and unsmoothed transmission coefficient for 0.508-mm GML 1000 (a) magnitude; (b) phase.

81

5.4.2 Sample Misplacement Correction

Errors due to misplacement of the sample in the quasi-optical test bench can easily arise, especially for a measurement system where the precision is of the order of a millimetre. Therefore, some investigation is required and a correction term accounting for this type of error must be developed.

5.4.2.1 Problem Statement

During the measurement process, the complete S-matrix is recorded, i.e. reflection coefficients (S_{11} and S_{22}) and transmission coefficients (S_{21} and S_{12}). Since the test bench is symmetrical, S_{11} should be equal to S_{22}, and S_{21} should be equal to S_{12}. However, in practice, this is not always the case.

The main problem occurs with the phase of the reflection coefficients. In the measurement setup used, the phase of S_{11} is usually different from the phase of S_{22}. The major reason to explain this discrepancy is that the sample may not be exactly at the reference plane (set by the calibration) or at an equal distance from the two feeding elements, i.e. at the output beam waist location.

In [38], some expressions accounting for the reference planes location in the case of waveguide measurement techniques are presented. These expressions require the knowledge of the thickness of the sample under test and its location or the distance of each reference plane. In the case of our free-space measurement system, this is a problem since the sample location is not perfectly known. However, by taking a similar approach, the problem can be solved differently without knowing the location of the sample. The result is a simple correction term.

5.4.2.2 Theory

If the sample is placed exactly at the reference plane as shown in Figure 5.3, the resulting matrix will be the same as (5-2). However, if the location of the reference plane is moved by a distance δ, as shown in Figure 5.6, the resulting S-matrix, S', is obtained by moving the reference plane [37] and is found to be

$$[S'] = \begin{bmatrix} \exp(+\gamma_0\delta) & 0 \\ 0 & \exp(-\gamma_0\delta) \end{bmatrix} [S] \begin{bmatrix} \exp(+\gamma_0\delta) & 0 \\ 0 & \exp(-\gamma_0\delta) \end{bmatrix};$$

$$[S'] = \begin{bmatrix} \exp(+\gamma_0\delta) & 0 \\ 0 & \exp(-\gamma_0\delta) \end{bmatrix} \begin{bmatrix} |\Gamma_s|\exp(j\phi_{\Gamma_s}) & |T_s|\exp(j\phi_{T_s}) \\ |T_s|\exp(j\phi_{T_s}) & |\Gamma_s|\exp(j\phi_{\Gamma_s}) \end{bmatrix} \begin{bmatrix} \exp(+\gamma_0\delta) & 0 \\ 0 & \exp(-\gamma_0\delta) \end{bmatrix};$$

$$[S'] = \begin{bmatrix} |\Gamma_s|\exp(j\phi_{\Gamma_s} + 2\gamma_0\delta) & |T_s|\exp(j\phi_{T_s}) \\ |T_s|\exp(j\phi_{T_s}) & |\Gamma_s|\exp(j\phi_{\Gamma_s} - 2\gamma_0\delta) \end{bmatrix}, \qquad (5\text{-}15)$$
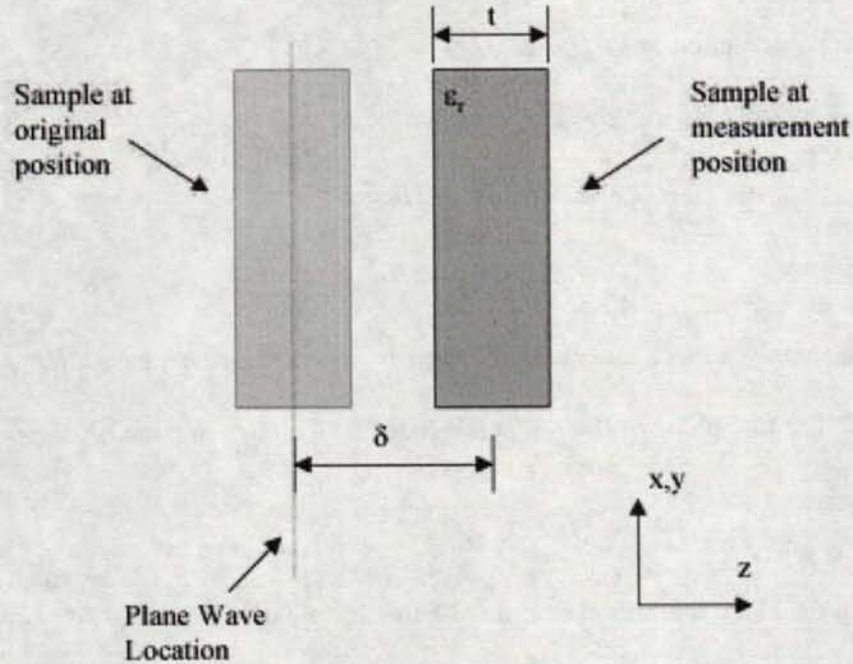
Figure 5.6: Side view of sample suffering from misplacement in direction of propagation.

where γ_0 is the propagation constant in free space:

$$\gamma_0 = \alpha_0 + j\beta_0 . \tag{5-16}$$

In (5-16), α_0 is the attenuation constant in free space and β_0 is the phase constant in free space. Knowing that α_0 is equal to zero, (5-15) can be rewritten as

$$[S'] = \begin{bmatrix} |\Gamma_S| \exp\left[j\left(\phi_{\Gamma_S} + 2\beta_0\delta\right)\right] & |T_S| \exp\left(j\phi_{T_S}\right) \\ |T_S| \exp\left(j\phi_{T_S}\right) & |\Gamma_S| \exp\left[j\left(\phi_{\Gamma_S} - 2\beta_0\delta\right)\right] \end{bmatrix} . \tag{5-17}$$

5.4.2.3 Correction

Comparing (5-17) with (5-2) reveals the following information:

— forward and reverse transmission coefficients of the slab, S_{21} and S_{12}, are not modified;

— the magnitudes of the reflection coefficients, S_{11} and S_{22}, are also unmodified;

— the phases of the reflection coefficients is modified, but the only difference is the addition or subtraction of a $2\beta_0\delta$ term.

Thus, from (5-17):

$$\angle S_{11}' = \phi_{\Gamma_S} + 2\beta_0\delta , \tag{5-18}$$

$$\angle S_{22}' = \phi_{\Gamma_S} - 2\beta_0\delta , \tag{5-19}$$

and one can simply cancel out the $2\beta_0\delta$ term by averaging the phase of the reflection coefficients. The true phase of the reflection coefficient is then obtained:

$$\phi_{\Gamma_S} = \frac{\angle S_{11}' + \angle S_{22}'}{2} . \tag{5-20}$$

We therefore conclude that the positioning of the sample along the axis of propagation is not very critical, as long as the sample remains close to the plane wave location. Otherwise, the wave might not be plane or nearly plane and there might be some error

introduced if a curved wave is incident on the sample. This misalignment becomes more critical as the frequency increases.

5.4.3 Calibration Process Correction

A second correction term is introduced to take into account the thickness of the sample, which is not included in the conventional TRM calibration. This correction assumes that the phase of the forward and reverse reflection coefficients were initially corrected using (5-20).

5.4.3.1 Problem Statement

Calibration of the free-space measurement system using a TRM process assigns a default value of zero for the phase of the transmission coefficient in the absence of a sample under test. Moreover, in the default configuration, the reflection coefficient has zero magnitude, therefore its phase is somehow undetermined.

Analysis should be performed to find if the phase values obtained after calibration of the system are accurate or not. A simple investigation would be to perform measurements on a virtual sample of air. Measuring a sample of air, or any medium that would be of permittivity equal to the ambient permittivity, basically means that no sample is being measured. In other words, the measurement system is unchanged and remains in its default configuration. Therefore, experimentally, the thickness of the virtual sample can be varied as desired without affecting the measured phase values. On the other hand, theoretical analysis reveals that the phase values should change with the thickness of the

sample. Thus, there is a contradiction between experimental and theoretical phase values. For that reason, a correction is needed to compensate for this inconsistency.

5.4.3.2 Theory

From (5-14), the reflection coefficient Γ of a sample of air is equal to zero because both relative permittivity and relative permeability are equal to unity. From (5-8):

$$\tau = \exp(-\gamma_0 t) = \exp(-j\beta_0 t) = \exp\left(-j\frac{2\pi}{\lambda_0}t\right), \qquad (5\text{-}21)$$

again for a sample of air. In (5-21), λ_0 corresponds to the free-space wavelength. Substituting these results for air in (5-5) and (5-6):

$$\Gamma_{S-air} = 0, \qquad (5\text{-}22)$$

$$T_{S-air} = \exp\left(-j\frac{2\pi}{\lambda_0}t\right), \qquad (5\text{-}23)$$

which proves that, for a sample of air, the phase of the transmission coefficient theoretically varies with the thickness.

Unfortunately, the phase of the reflection coefficient is undetermined in this case because its magnitude is zero. Nevertheless, the phase value can be found mathematically using (5-5) to (5-14) for any sample. Knowing that a lossless material has real values of ε_r and μ_r, it is easy to show that Γ is real and that τ has a magnitude equal to unity. Furthermore, in the case of a dielectric material, ε_r is greater than unity and μ_r is equal to one. From (5-14), this means Γ will be negative. Considering the reflection coefficient of the slab, (5-5) can be modified as follow:

$$\Gamma_s = \frac{-G\left\{1 - [\exp(j\sigma)]^2\right\}}{1 - G^2 [\exp(j\sigma)]^2} = \frac{-G[1 - \exp(j2\sigma)]}{1 - G^2 \exp(j2\sigma)} = \frac{-G[1 - \cos(2\sigma) - j\sin(2\sigma)]}{1 - G^2 \cos(2\sigma) - jG^2 \sin(2\sigma)}, \quad (5\text{-}24)$$

where G is the magnitude of Γ and σ is the phase of τ. We are interested in the phase of Γ_S:

$$\phi_{\Gamma_s} = \arctan\left(-\frac{\sin(2\sigma)}{1-\cos(2\sigma)}\right) - \arctan\left(-\frac{G^2 \sin(2\sigma)}{1-G^2 \cos(2\sigma)}\right),$$

$$\phi_{\Gamma_s} = \arctan\left(-\frac{\cos\sigma}{\sin\sigma}\right) + \arctan\left(\frac{G^2 \sin(2\sigma)}{1-G^2 \cos(2\sigma)}\right),$$

$$\phi_{\Gamma_s} = \begin{cases} \sigma + \arctan\left(\dfrac{G^2 \sin(2\sigma)}{1-G^2 \cos(2\sigma)}\right) + 90° \text{ if } 0° \le \sigma \le 180° \\ \sigma + \arctan\left(\dfrac{G^2 \sin(2\sigma)}{1-G^2 \cos(2\sigma)}\right) - 90° \text{ if } -180° \le \sigma \le 0° \end{cases} \quad (5\text{-}25)$$

Thus, the phase of the reflection coefficient is obtained.

The phase of the transmission coefficient can also be obtained mathematically. Considering the transmission coefficient of the slab, (5-6) can be modified as follows:

$$T_S = \frac{-[\exp(j\sigma)](1-G^2)}{1-G^2[\exp(j\sigma)]^2} = \frac{-[\cos(\sigma) + j\sin(\sigma)](1-G^2)}{1-G^2 \cos(2\sigma) - jG^2 \sin(2\sigma)}. \quad (5\text{-}26)$$

Once again, we are interested in the phase:

$$\phi_{T_S} = \arctan\left(\frac{\sin(\sigma)}{\cos(\sigma)}\right) - \arctan\left(-\frac{G^2 \sin(2\sigma)}{1-G^2 \cos(2\sigma)}\right),$$

$$\phi_{T_S} = \sigma + \arctan\left(\frac{G^2 \sin(2\sigma)}{1-G^2 \cos(2\sigma)}\right). \quad (5\text{-}27)$$

5.4.3.3 Correction

Comparison of (5-25) and (5-27) demonstrates that the phase difference between reflection and transmission coefficients of a slab is always ±90°. This is always true for lossless materials, however this is not the case for lossy materials since Γ is complex and τ has a magnitude less than unity. It is also observed that the phase of the reflection coefficient never takes values between −90° and +90°. This is shown by considering

87

(5-25): this equation is discontinuous as σ tends to $0°$ or $180°$. Taking the one-sided limits from the right and from the left at values of σ equal to $0°$ or $180°$ proves this statement. Hence, one will see that no value lies between $-90°$ and $+90°$. This is true for any value of G. The discontinuity in the phase of Γ_s is in fact due to the discontinuous nature of the inverse tangent.

Appendix C provides an alternative approach of understanding the behaviour of the reflection and transmission coefficients based on graphical approaches. From this point of view, it is observed that, for a dielectric constant of unity, the phase of the transmission coefficient of the slab varies with thickness, but tends to $0°$ as the thickness decreases. A similar comment can be formulated by considering the phase of the reflection coefficient of the slab, however in this case the phase tends to $-90°$. These observations are in agreement with (5-25) and (5-27). Therefore, for infinitely thin samples, the phase provided by the measurements with the TRM calibration applied would be accurate. This correction can then be seen as a compensation for the thickness of the sample, which is not taken into account by the TRM calibration. In other words, the phase measured is a relative phase rather than an absolute phase.

Once it is known that a relative phase value is measured, the appropriate correction can be developed. Knowing that the measured phase shift should be equal to the theoretical phase shift, or that the measured relative phase is equal to the theoretical relative phase, we simply state that:

$$\phi_{relative-measured} = \phi_{relative-theoretical} \cdot \qquad (5\text{-}28)$$

The relative phase means the difference between the phase of the sample of thickness t and the phase of a virtual sample of air of the same thickness t. Comparison is made with air

because it corresponds to the default configuration and it was shown from measurement that the phase is null, no matter what the thickness of the sample is. Thus:

$$\phi_{T_{S-measured}} - \phi_{T_{S-air-measured}} = \phi_{T_S} - \phi_{T_{S-air}}. \qquad (5\text{-}29)$$

In this case, the phase measured by the sample of air is zero, as demonstrated previously. Reorganising (5-29):

$$\phi_{T_S} = \phi_{T_{S-measured}} + \phi_{T_{S-air}}, \qquad (5\text{-}30)$$

where the phase of the transmission coefficient for a sample of air is obtained from (5-21):

$$\phi_{T_{S-air}} = -\frac{2\pi}{\lambda_0}t = -\frac{360°}{\lambda_0}t. \qquad (5\text{-}31)$$

The correlation between the phase of the reflection coefficient and the phase of the transmission coefficient means that the phase of the reflection coefficient must also be corrected by the same amount as the phase of the transmission coefficient. Therefore, since the resulting value may end up in the forbidden region, we may have to apply an additional 180° correction. Consequently, proceeding the same way as for the case of the transmission coefficient is possible. Similarly to (5-29):

$$\phi_{\Gamma_{S-measured}} - \phi_{\Gamma_{S-air-measured}} = \phi_{\Gamma_S} - \phi_{\Gamma_{S-air}}. \qquad (5\text{-}32)$$

Knowing that there is a ±90° phase shift between the measured phase of the reflection and transmission coefficients (see Appendix C) and that the measured phase of the transmission coefficient is equal to zero:

$$\phi_{\Gamma_{S-air-measured}} = \phi_{T_{S-air-measured}} \pm 90° = \pm 90°. \qquad (5\text{-}33)$$

Similarly, From (5-25) and (5-27):

$$\phi_{\Gamma_{S-air}} = \phi_{T_{S-air}} \pm 90°. \qquad (5\text{-}34)$$

Substituting (5-33) and (5-34) in (5-32) and considering only valid solutions for the phase of the reflection coefficient:

$$\phi_{\Gamma_S} = \begin{cases} \phi_{\Gamma_{S-measured}} + \phi_{T_{S-air}} \\ \phi_{\Gamma_{S-measured}} + \phi_{T_{S-air}} - 180° \end{cases}; \quad -180° \le \phi_{\Gamma_S} \le -90° \text{ or } 90° \le \phi_{\Gamma_S} \le 180°. \quad (5\text{-}35)$$

5.5 Dielectric Constant Extraction Techniques

Having applied the correction terms, the reflection and transmission coefficients of the sample can be used to extract the dielectric constant. Various techniques can be utilised for the extraction of the dielectric constant from the S-parameter measurements [19, 38]. These techniques can be separated into two main categories: algebraic techniques and numerical techniques.

5.5.1 Algebraic Techniques

Algebraic techniques are usually based on explicit expressions. If the dielectric constant of a sample is known, the reflection and transmission coefficients at the air-sample interface are easily obtained using (5-7) and (5-8). Then, the reflection and transmission coefficients of the slab are obtained using (5-5) and (5-6).

However, in problems where the dielectric constant must be determined, the measured parameters are the reflection and transmission coefficients of the sample. From these values, the reflection and transmission coefficients at the air-sample interface must be calculated, then the dielectric constant is found. In other words, it is the inverse problem compared to what is presented in section 5.3. By manipulation of (5-5) and (5-6),

the values of the reflection and transmission coefficients at the air-sample interface are obtained:

$$\Gamma = \kappa \pm \sqrt{\kappa^2 - 1}, \tag{5-36}$$

$$\tau = \frac{T_S}{1 - \Gamma_S \Gamma}, \tag{5-37}$$

where

$$\kappa = \frac{\Gamma_S^{\,2} - T_S^{\,2} + 1}{2\Gamma_S}. \tag{5-38}$$

Derivations of these equations are presented in Appendix D.

In (5-8), we see that τ is obtained from γ_S, the propagation constant in the sample under test. By proper manipulation and considering multiple solutions [19]:

$$\gamma_S = \frac{\ln\left(\left|\tau\right|^{-1}\right) + j(2\pi n - \angle\tau)}{t}, \tag{5-39}$$

where n is an integer. If the sample under test has a thickness less than half a guided wavelength in the slab, n is equal to zero. Otherwise, n must respect the following rule:

$$\left(n - \frac{1}{2}\right)\lambda_S \leq t \leq \left(n + \frac{1}{2}\right)\lambda_S, \tag{5-40}$$

where λ_S is the guided wavelength in the slab. The problem is the following: ε_r is unknown, hence λ_S is also unknown because of the relationship between the two parameters:

$$\lambda_S = \frac{\lambda_0}{\sqrt{\varepsilon_r}}. \tag{5-41}$$

Therefore, the accurate value of n, and consequently the accurate value of γ_S, remain to be found.

Assuming the propagation constant of the slab is known, the dielectric constant and the relative permeability can be found using the following equations [19]:

$$\varepsilon_r = \frac{\gamma_S}{\gamma_0}\left(\frac{1-\Gamma}{1+\Gamma}\right), \qquad (5\text{-}42)$$

$$\mu_r = \frac{\gamma_S}{\gamma_0}\left(\frac{1+\Gamma}{1-\Gamma}\right). \qquad (5\text{-}43)$$

For dielectric materials, it is known that the permeability is equal to unity. Therefore, a procedure based on the calculation of both dielectric constant and relative permeability is developed to accurately find the value of γ_S and hence the value of n. The accurate values are the ones for which the relative permeability is unity. Thus, the dielectric constant is calculated using the same values.

The algebraic method is straightforward and relatively simple to apply once the ambiguity of multiple solutions is eliminated. On the other hand, this method is found to be inaccurate for a certain range of sample thicknesses. It is observed that the magnitude of the reflection coefficient tends to zero when the thickness of the sample is close to multiples of half a guided wavelength in the sample [38] (see, for example, Figure C.1(a)):

$$t = n\frac{\lambda_S}{2} = \frac{n\lambda_0}{2\sqrt{\varepsilon_r}}. \qquad (5\text{-}44)$$

In this case, (5-36) and (5-38) become unstable. It is easy to determine if measurements are performed close to multiples of half a guided wavelength in the sample since this occurs when the magnitude of Γ_S is low. There are ways to overcome this problem, such as measuring at a different frequency or changing the thickness of the sample, but these modifications are not always desired or possible. Finally, we conclude that this extraction

technique, despite some obvious advantages, is unsuitable as a universal extraction solution, but can be used to aid in the convergence of numerical techniques.

5.5.2 Numerical Techniques

As an alternative, numerical techniques are considered. Numerical techniques cover a wide range of algorithms, such as root-finding algorithms, non-linear regression procedures, genetic algorithms, etc. These methods are usually more robust compared to algebraic techniques. We have selected two different numerical approaches to extract the dielectric constant: a root-finding algorithm and a genetic algorithm.

5.5.2.1 Root-Finding Algorithm

A root-finding algorithm (RFA) is used to extract the permittivity. The root-finding algorithm is embedded in Mathcad [34] and employs the secant and Mueller methods to find the root of an equation. The tolerance criterion has been reduced from its default value to improve convergence. The equation used is based on the determinant of the S-matrix [38]. From (5-2) to (5-6):

$$[S] = \begin{bmatrix} \Gamma_S & T_S \\ T_S & \Gamma_S \end{bmatrix} = \begin{bmatrix} \dfrac{\Gamma(1-\tau^2)}{1-\Gamma^2\tau^2} & \dfrac{\tau(1-\Gamma^2)}{1-\Gamma^2\tau^2} \\ \dfrac{\tau(1-\Gamma^2)}{1-\Gamma^2\tau^2} & \dfrac{\Gamma(1-\tau^2)}{1-\Gamma^2\tau^2} \end{bmatrix}. \tag{5-45}$$

Applying the determinant:

$$\det[S] = \Gamma_S{}^2 - T_S{}^2 = \left[\frac{\Gamma(1-\tau^2)}{1-\Gamma^2\tau^2}\right]^2 - \left[\frac{\tau(1-\Gamma^2)}{1-\Gamma^2\tau^2}\right]^2,$$

$$\Gamma_S{}^2 - T_S{}^2 = \frac{\Gamma^2(1-2\tau^2+\tau^4)}{(1-\Gamma^2\tau^2)^2} - \frac{\tau^2(1-2\Gamma^2+\Gamma^4)}{(1-\Gamma^2\tau^2)^2},$$

$$\Gamma_S^{\ 2} - T_S^{\ 2} = \frac{\left(\Gamma^2 - 2\Gamma^2\tau^2 + \Gamma^2\tau^4\right) - \left(\tau^2 - 2\Gamma^2\tau^2 + \Gamma^4\tau^2\right)}{\left(1 - \Gamma^2\tau^2\right)^2},$$

$$\Gamma_S^{\ 2} - T_S^{\ 2} = \frac{\left(\Gamma^2 + \Gamma^2\tau^4 - \tau^2 - \Gamma^4\tau^2\right)}{\left(1 - \Gamma^2\tau^2\right)^2},$$

$$\Gamma_S^{\ 2} - T_S^{\ 2} = \frac{\left(\Gamma^2 - \tau^2\right)\left(1 - \Gamma^2\tau^2\right)}{\left(1 - \Gamma^2\tau^2\right)^2},$$

$$\Gamma_S^{\ 2} - T_S^{\ 2} = \frac{\Gamma^2 - \tau^2}{1 - \Gamma^2\tau^2}. \tag{5-46}$$

In (5-46), Γ_S and T_S are the corrected reflection and transmission coefficients of the sample obtained from measurement. Moreover, both Γ and τ are a function of the dielectric constant, ε_r, which is the unknown to determine. Since the root-finding algorithm requires a guess value to initialise the process, the value of the permittivity found with the algebraic technique described in section 5.5.1 is used [38].

Equation (5-46) will remain stable if Γ or τ tend to zero. However, the determinant of the matrix must not be equal to zero. In this case:

$$\det[S] = \Gamma_S^{\ 2} - T_S^{\ 2} = 0 \Rightarrow \Gamma_S^{\ 2} = T_S^{\ 2}. \tag{5-47}$$

For (5-47) to be true:

$$|\Gamma_S| = |T_S|, \text{ and} \tag{5-48}$$

$$\angle\Gamma_S = \angle T_S \text{ or } \angle\Gamma_S = \angle T_S + 180° \tag{5-49}$$

From the observations made in Appendix C, the phase of the reflection coefficient of the slab is always $\pm90°$ the phase of the transmission coefficient of the slab for lossless materials. Therefore, the determinant of the S-matrix will never be equal to zero, at least

94

not for low-loss materials, and we can conclude that proceeding with the determinant equation will ensure stability.

Finally, it was found that trying to solve this problem with uncorrected reflection and transmission coefficients can make the root-finding algorithm unable to converge to a solution. This shows the importance of the correction terms reported previously.

5.5.2.2 Genetic Algorithm

A novel alternative to handle parameter extraction problems is the application of a genetic algorithm (GA). In this case, the material parameters are determined by the GA from a best fit of the corrected reflection and transmission coefficients.

The genetic algorithm used has been developed at the Communications Research Centre to be used for different optimisation problems [39]. In the parameter extraction problem, (5-5) to (5-14) are inserted into the genetic algorithm. Initially, a certain number of trial solutions of dielectric constant are generated randomly by the GA. These trial solutions are referred to as the population. Then, reflection and transmission coefficients are calculated for each trial solution and an error function is computed for each case. The error function consists of comparing the real and imaginary parts of the reflection and transmission coefficients of each trial solution with the corrected coefficients obtained from the measurement process:

$$error \equiv \left[\mathrm{Re}\left(\Gamma_S{}^{trial}\right) - \mathrm{Re}\left(\Gamma_S{}^{corrected}\right)\right]^2 + \left[\mathrm{Im}\left(\Gamma_S{}^{trial}\right) - \mathrm{Im}\left(\Gamma_S{}^{corrected}\right)\right]^2$$

$$+ \left[\mathrm{Re}\left(T_S{}^{trial}\right) - \mathrm{Re}\left(T_S{}^{corrected}\right)\right]^2 + \left[\mathrm{Im}\left(T_S{}^{trial}\right) - \mathrm{Im}\left(T_S{}^{corrected}\right)\right]^2. \qquad (5\text{-}50)$$

Then, only the entities with the best fitness, i.e. the entities that give a minimal error function, remain. The other entities are simply discarded. The number of entities to be

replaced depends on the replacement ratio of the population, which is initially specified. From the remaining entities, a new set of entities is obtained, which form a new population. The process of creating a new population from a previous one is called a generation. The procedure is repeated for a certain number of generations. Using a genetic algorithm, global optimisation is obtained for a predetermined range of values. This is a significant advantage over a root-finding algorithm because if the initial value is not close enough to the solution, the problem may converge to another solution. For more details on genetic algorithms, see [40, 41].

Some genetic algorithms allow the user to specify a convergence criterion, which stops the computation and ensures convergence for a certain minimal error. However, the algorithm used in this particular case does not support such a stopping criterion. Thus, the user must look at the value of the error function to conclude if convergence has occurred, in which case the problem has succeeded. If the error function is too high, the problem has to be recomputed with a larger population size or more generations.

The main problem with the genetic algorithm used is that a lot of time was required to find a solution. As a comparison, a root-finding algorithm can find a solution for a frequency range of about 400 frequency points in only a few seconds whereas the genetic algorithm requires almost an hour to converge with about 10 frequency points. Solving a 10-frequency point problem requires, in average, a population of about 5000 entities with a replacement ratio of 50% and around 500 generations. With similar results obtained with both RFA and GA, one should wonder if the genetic algorithm is useful for that type of problem. For low-loss materials with low value of dielectric constant, the advantage is limited, however for high-loss materials or materials with high dielectric constant, the

global optimisation nature of the genetic algorithm might be useful as root-finding algorithms may not be suited for these types of problems [42].

5.6 Measurement Results

Dielectric and semiconductor materials were measured using the quasi-optical measurement system. The dielectric constant for these materials varies between 2 and 12. The materials are common materials from circuit board manufacturers or silicon wafers providers: RO 3006, RO 4003, RT 5880 and TMM 10i from Rogers Corporation, GML 1000 from GIL Technologies and n-type high-resistivity 5000 ohm-cm silicon wafer from Silicon Quest International.

Published data on the materials are provided at a frequency of 10 GHz. Our measurements were performed in free space from 28 GHz to 32 GHz. Since the value of dielectric constant and loss tangent may vary with frequency, comparison of measurements over two different bands may not be appropriate, even though the permittivity is known not to vary much between these two frequencies with such materials.

To overcome this problem, the dielectric samples were sent for characterisation to the Radio-Frequency Technology Division at the National Institute of Standards and Technology (NIST). Measurements were performed over two different frequency bands, corresponding to the manufacturers' band and the band of the measurement system. This allows comparison of manufacturers specifications with NIST split-post technique and our measurements with NIST split-cylinder technique. Note that both techniques used at NIST are resonance techniques. Measurements performed over two different frequency bands allows to verify the variation of the dielectric constant over frequency.

Table 5.2 provides the results obtained from the manufacturers, NIST and the free-space measurement system. The results obtained with the free-space quasi-optical measurement system at 30 GHz are denoted *CRC* in Table 5.2. In order to present results over a frequency band rather than at a single frequency point, the extraction process has been applied to multiple frequency points. Dielectric constant and loss tangent for various materials are presented in Figures 5.7 to 5.14 from 28 GHz to 32 GHz: Figure 5.7 shows results for 0.7874-mm RT 5880; Figure 5.8 shows results for 0.508-mm GML 1000; Figure 5.9 shows results for 0.762-mm GML 1000; Figure 5.10 shows results for 0.508-mm RO 4003; Figure 5.11 shows results for 0.8128-mm RO 4003; Figure 5.12 shows results for 0.635-mm RO 3006; Figure 5.13 shows results for 0.508-mm TMM 10i and; Figure 5.14 shows results for 350-μm high-resistivity silicon. The root-finding algorithm (RFA) uses 401 points whereas the genetic algorithm (GA) uses only 9 points. The number of points for the genetic algorithm is much less than for the root-finding algorithm in order to limit the size of the problem and allow convergence in an acceptable time.

5.7 Discussion

Measurements taken at X-band show that comparison of both characterisation techniques gives a difference up to about 8% for the dielectric constant and a difference as high as ±0.001 for the loss tangent. Comparison of NIST measurements at both frequency bands shows that the dielectric constant varies by less than 2% from about 10 GHz to about 30 GHz and the loss tangent is relatively constant, except for 0.508-mm RO 4003 and the high-resistivity silicon wafer, where the loss tangent is quite different between the

Table 5.2: Measurement results for materials at two different frequency bands using different techniques.

Material		RT5880	GML1000	GML1000	RO4003	RO4003	RO3006	TMM10i	Silicon
Thickness (mm)		0.7874	0.508	0.762	0.508	0.8128	0.635	0.508	0.350
X-band measurements									
Manufacturers	Dielectric constant	2.20	3.05	3.20	3.38	3.38	6.15	9.80	11.70
(Stripline resonator)	Loss tangent	0.0009	0.004	0.004	0.0027	0.0027	0.0025	0.0020	0.0030
NIST	Dielectric constant	2.29	3.05	3.30	3.68	3.61	6.57	10.17	11.60
(Split-post)	Loss tangent	0.0010	0.0051	0.0051	0.0028	0.0027	0.0016	0.0018	0.0041
	Frequency (GHz)	9.944	9.946	9.854	9.896	9.815	9.607	9.474	9.593
K/Ka band measurements									
CRC	Dielectric constant	2.31	3.06	3.28	3.68	3.48	6.54	9.88	11.30
(T/R free-space, RFA)	Loss tangent	-0.0018	-0.0006	0.0056	0.0013	0.0031	0.0232	0.0158	0.0105
CRC	Dielectric constant	2.29	3.03	3.24	3.64	3.46	6.41	9.80	11.20
(T/R free-space, GA)	Loss tangent	-0.0016	-0.0005	0.0068	-0.0025	0.0013	0.0191	0.0109	0.0039
NIST	Dielectric constant	2.30	3.02	—	3.62	3.60	6.59	10.25	11.62
(Split-cylinder)	Loss tangent	0.0012	0.0047	—	0.0051	0.0028	0.0014	0.0022	0.0015
	Frequency (GHz)	29.531	29.943	—	28.569	26.425	22.746	20.969	22.621

Figure 5.7: Dielectric constant and loss tangent for 0.7874-mm RT 5880.

Figure 5.8: Dielectric constant and loss tangent for 0.508-mm GML 1000.

Figure 5.9: Dielectric constant and loss tangent for 0.762-mm GML 1000.

Figure 5.10: Dielectric constant and loss tangent for 0.508-mm RO 4003.

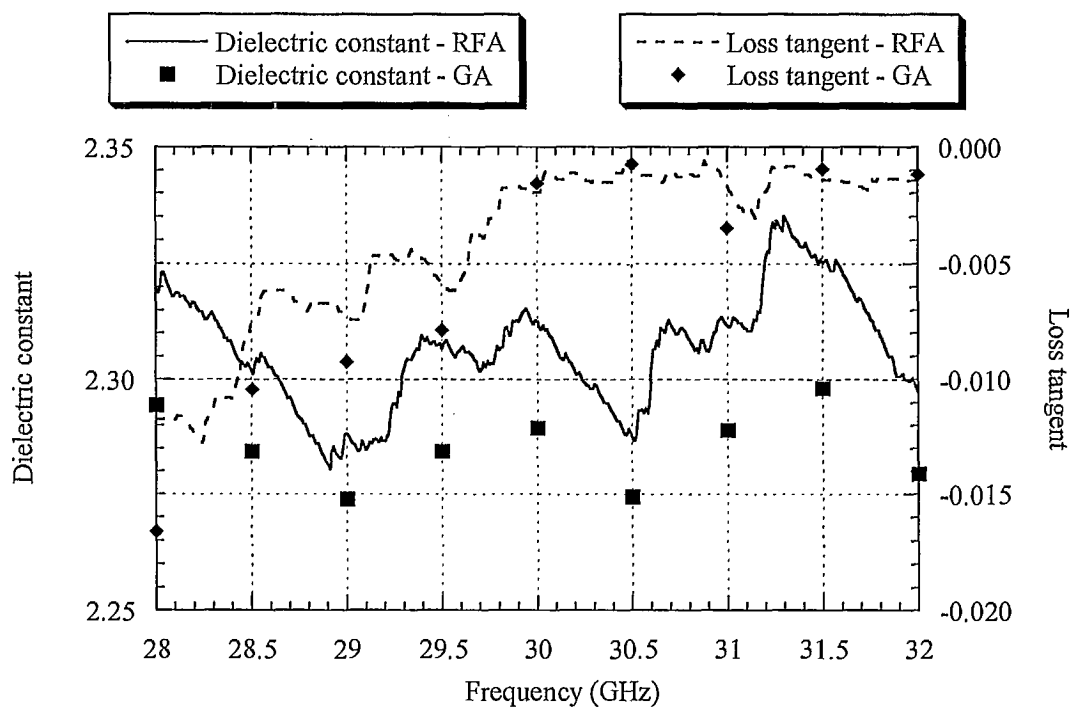**Figure 5.11: Dielectric constant and loss tangent for 0.8128-mm RO 4003.**

Figure 5.12: Dielectric constant and loss tangent for 0.635-mm RO 3006.

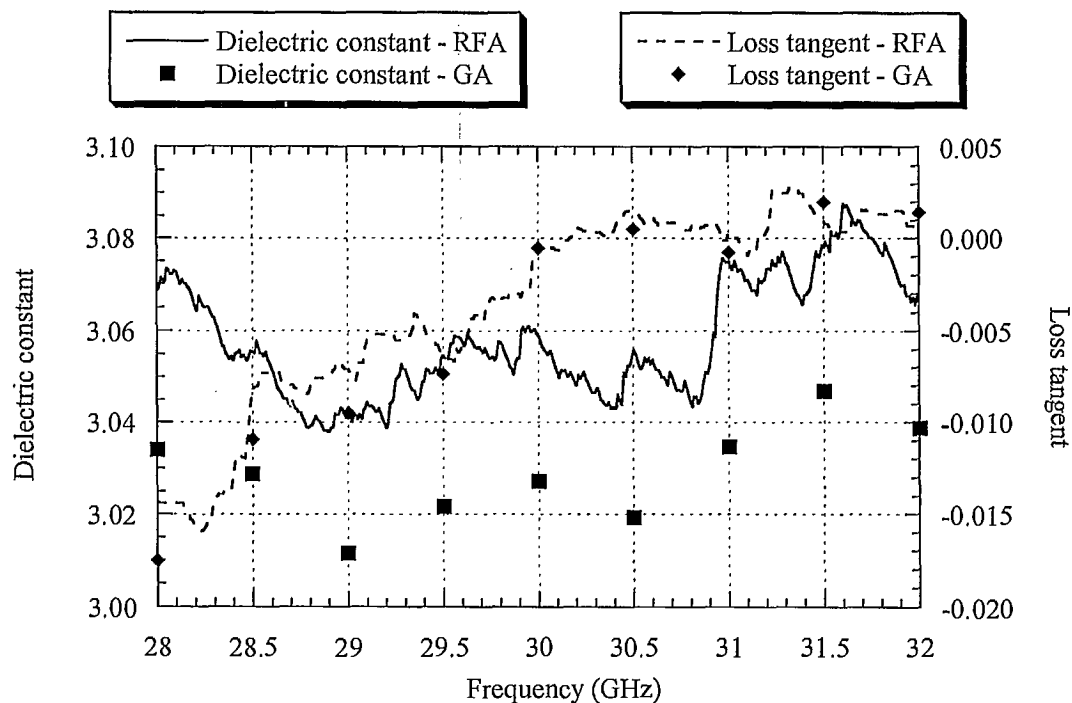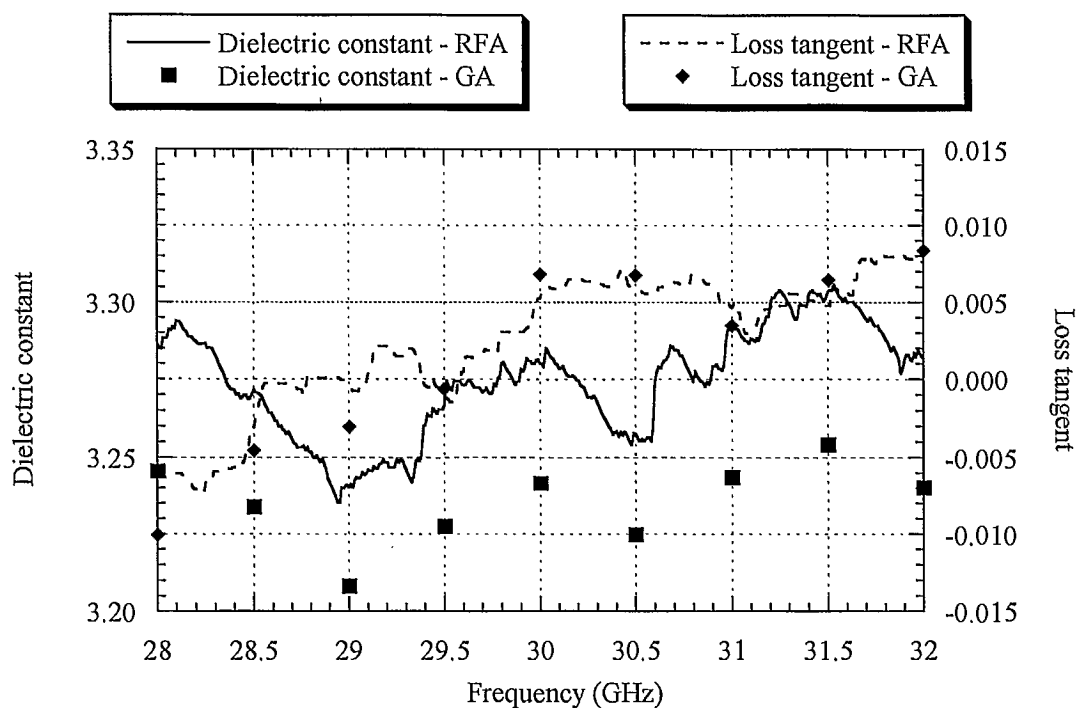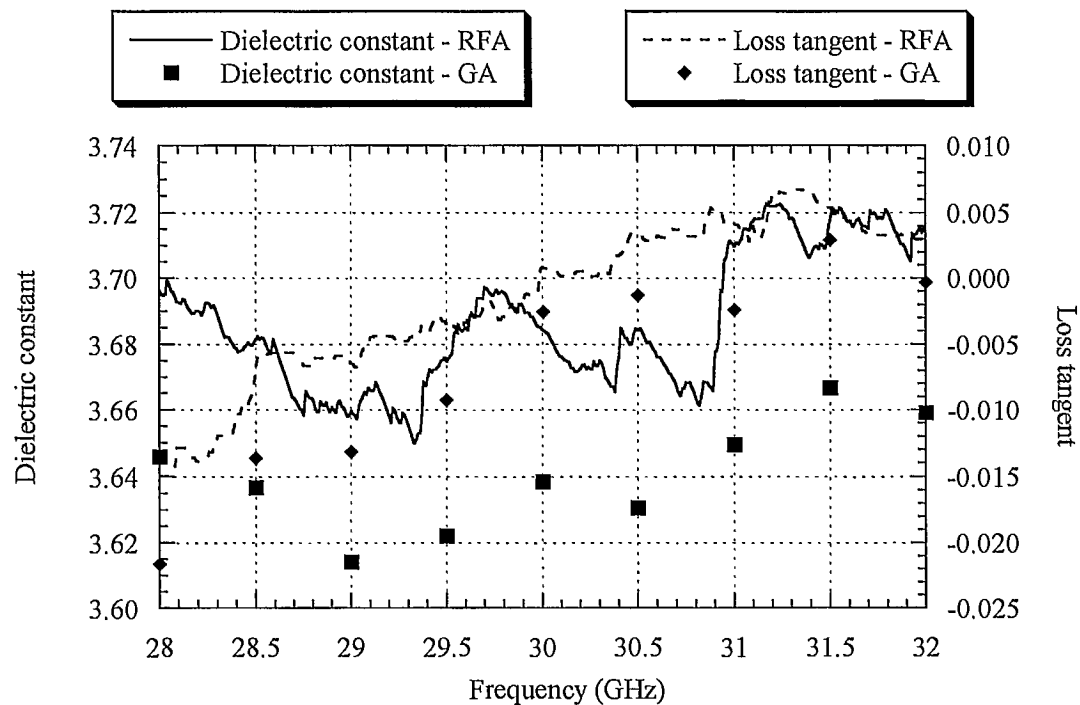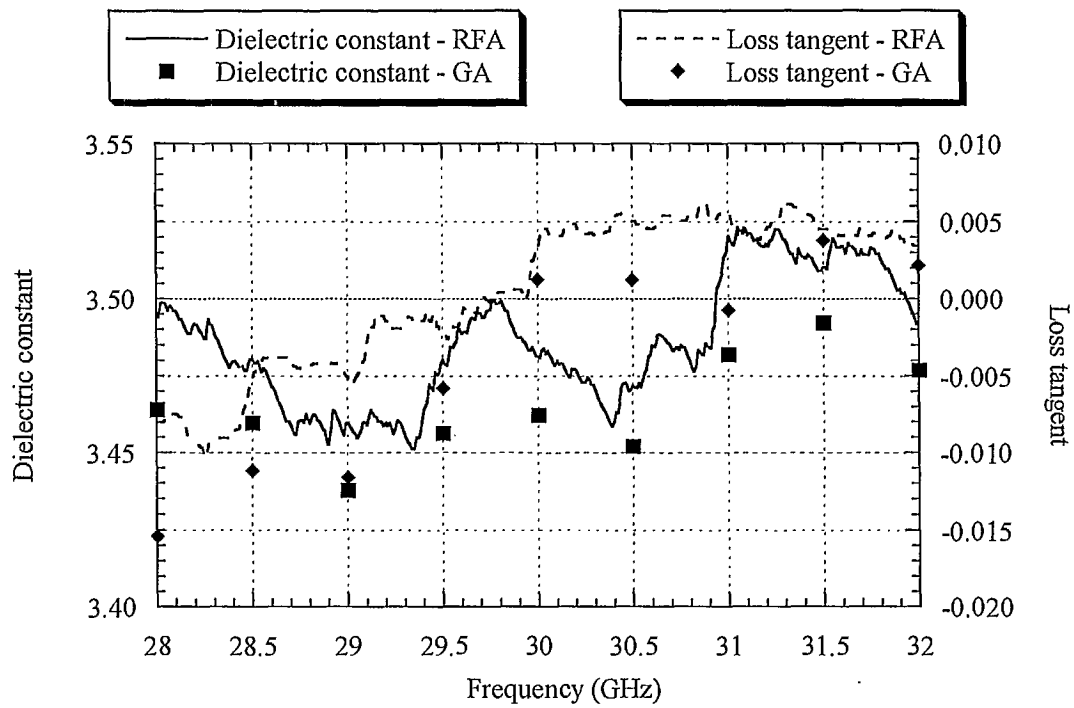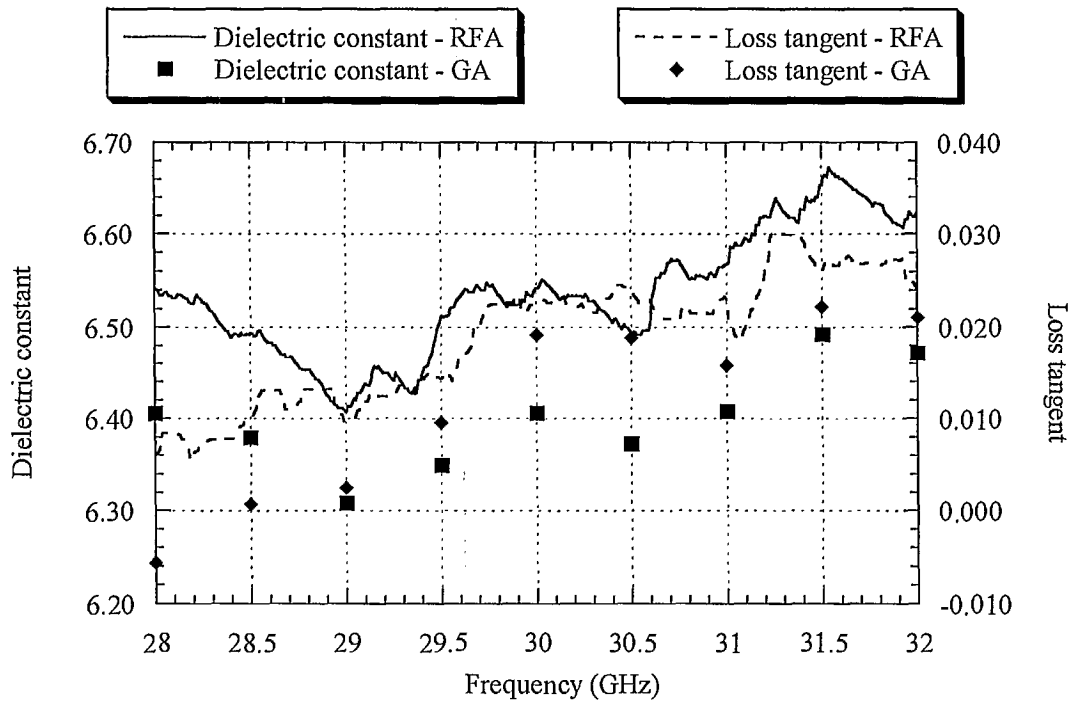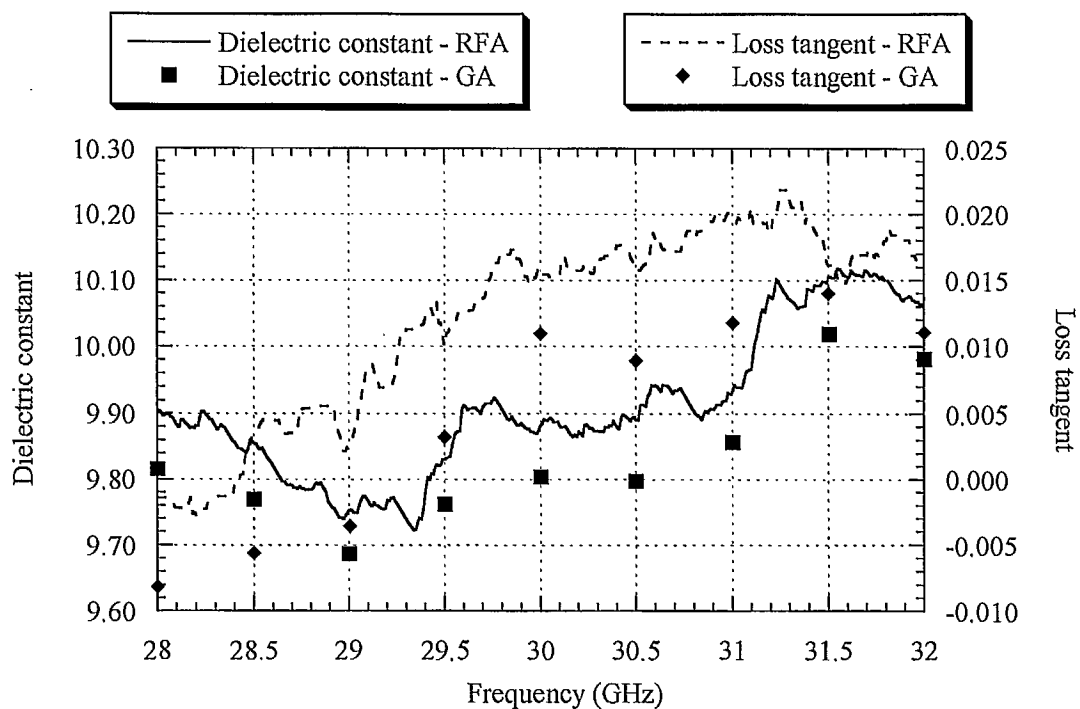**Figure 5.13: Dielectric constant and loss tangent for 0.508-mm TMM 10i.**
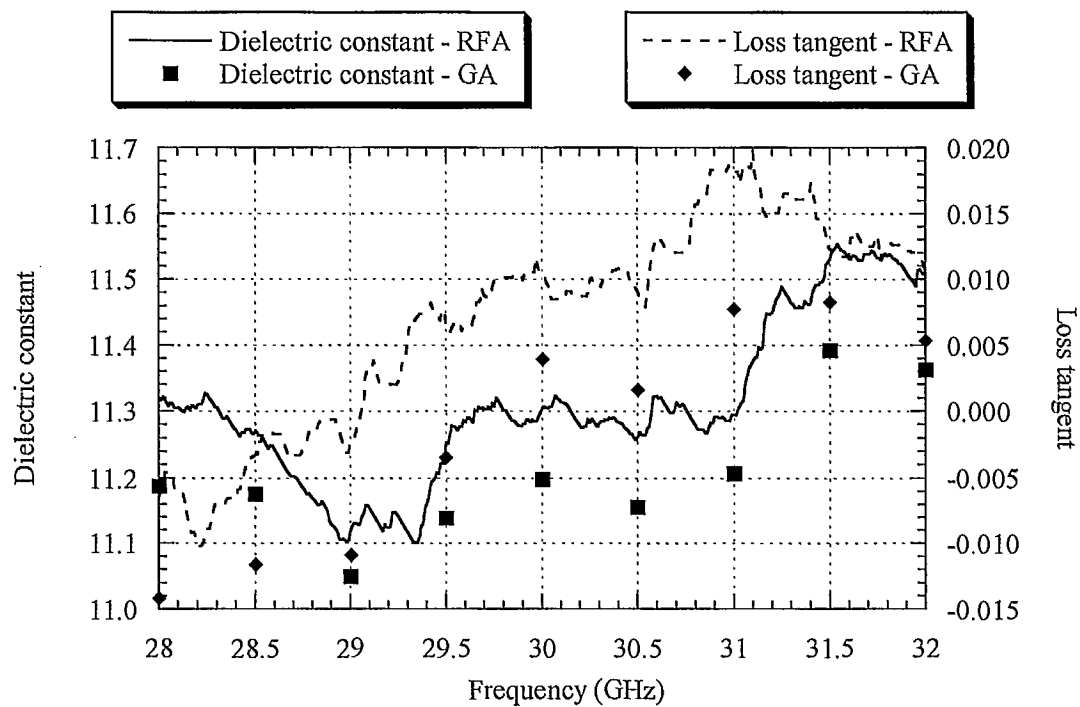

Figure 5.14: Dielectric constant and loss tangent for 350-μm high-resistivity silicon.

two bands. However, the loss tangent of silicon is very sensitive to frequency, therefore this type of behaviour was expected. Appendix E explains the conversion of surface resistivity to loss tangent for silicon materials.

Results obtained with the free-space quasi-optical measurement system reveal that the two different extraction techniques provide about the same results for the dielectric constant, where the difference is less than 2%. These results also agree with those from NIST, where the difference is less than 5%. Note that NIST resonance technique at high frequency was unable to find a solution for 0.762-mm GML 1000 material, which was apparently too lossy for the resonator to produce a clear resonance.

In the case of the loss tangent, results differ more. In fact, the transmission/reflection free-space technique seems to fail in some cases since negative values of loss tangent are obtained. This confirms the affirmation by Ghodgaonkar et al. [19], who state that loss tangent values less than 0.1 cannot be found accurately with a two-port free-space transmission/reflection measurement system.

Analysis of the broadband measurements reveals that the resulting values of dielectric constant and loss tangent are always less for the genetic algorithm compared to the root-finding algorithm. This difference may be the result of unequal convergence of the two extraction methods. Comparison of the error function in (5-50) using the root-finding algorithm and the genetic algorithm reveals that the genetic algorithm generally offers better convergence than the root-finding algorithm: typical values of error function for the genetic algorithm are between 0.00001 and 0.0005 whereas the error function is between 0.0001 and 0.0005 for the root-finding algorithm (it is observed that the error function varies depending on the material to determine). Nevertheless, it is expected that

adjustment of the convergence parameters of both extraction techniques would lead in identical results.

However, the difference in convergence may be explained by the fact that the equations to optimise in the two techniques are different: the root-finding algorithm makes use of (5-46) while the genetic algorithm exploits (5-5) and (5-6). Thus, since the root-finding algorithm uses an equation which does not describe directly the reflection and transmission coefficients of the sample, the convergence may not be as good as for the case of the genetic algorithm.

Finally, we note that the dielectric constant is relatively constant over the frequency range of observation, where the highest difference is found to be 4%. On the other hand, the loss tangent is found to vary more, which could be explain by the inaccuracy of the method for determining the loss tangent.

CHAPTER 6 Conclusions and Future Work

6.1 Summary

This thesis has described the design and study of a free-space quasi-optical measurement system to be used for material characterisation at Ka band. A study of misalignments was performed using a Gaussian beam coupling formulation. A method for determining the properties of dielectric materials, including correction terms due to the misplacement of the sample under test and to the calibration procedure, was presented. Extraction techniques based on a root-finding algorithm and on a genetic algorithm were proposed.

6.2 Conclusions

A contactless and non-destructive measurement system, allowing one to physically modify the sample under test, has been realised. The measurement system consists of a free-space quasi-optical test bench with a pair of colinear horn-fed lenses connected to a network analyser. The major accomplishments of this work are the following:

- the design, fabrication and study of the mechanical structure and RF components of the measurement system;

- the study of the effects of component misalignments by means of a Gaussian beam coupling formulation;

- the development of free-space calibration standards and procedure;

- the application of unique correction terms to correct for sample misplacement and calibration procedure;

– the use of up-to-date numerical extraction techniques, which include a root-finding algorithm and a novel genetic algorithm;

– the validation of the entire work by comparing our results with those obtained at the National Institute of Standards and Technology (NIST).

Furthermore, the measurement system developed herein is relatively low-cost compared to other free-space quasi-optical measurement systems because it employs pyramidal horns, millimetre-precision equipment and it does not make use of time-domain gating. Based on the above accomplishments and the specific features of this system, it will now be possible to undertake the advanced material characterisation and component testing required for optically-induced array antenna development, as described in the next section.

6.3 Future Work

This thesis reported the characterisation of dielectric materials with relative permittivity value below 12 and high-resistivity silicon. Many more types of materials could be measured with the quasi-optical measurement system, such as:

– dielectric materials with high value of dielectric constant;

– ferrite materials;

– artificial dielectrics;

– anisotropic materials;

– optically-induced semiconductors.

For the characterisation of some of these materials, the extraction techniques presented in this thesis would have to be modified and/or validated. Moreover, quasi-optical

components, such as filters, amplifiers and polarisers, could also be measured with this measurement system.

As mentioned in Chapter 1, the next step related to the development of the quasi-optical measurement system is to integrate optical illumination for the characterisation of semiconductor materials with different intensity of optical power. Such an apparatus will allow to conduct a study of the induced plasma at the semiconductor surface, then leading to optically-controlled antenna design. Moreover, the extraction techniques presented in this thesis will have to be verified for the induced plasma characterisation.

Improvements of the measurement system could also be performed. Some parts of the mechanical structure could be replaced to allow better confidence on the alignments. In addition, replacing the feed horns with narrower beam antennas or corrugated horns could improve the results, however such a change would require major modifications on the structure of the measurement system and more investments as such antennas are quite expensive. Furthermore, the lenses could be improved by incorporating a matching layer, which would reduce the mismatch at the surface of the lenses and should reduce considerably the standing wave amplitude and the ripples in the S-parameter measurements. On the other hand, this matching method would limit the broadband advantage of the transmission/reflection free-space measurement system since the matching layer is designed for a single frequency.

APPENDIX A Pyramidal Horn

A.1 Introduction

The study of the geometrical structure of the pyramidal horns used to launched the Gaussian beam is presented in this appendix. It basically consists of an analysis to obtain all the necessary dimensions from the pyramidal horn in order to find the location of the apex and the beam waist.

A.2 Theory

From the feed horn, only a few dimensions can be measured with accuracy: the internal size of the aperture, the internal size of the waveguide and the external extension length. All the other dimensions cannot be measured with precision, however they can be calculated from the measured ones. This section develops the necessary equations required to calculate unknown dimensions.

Figure A.1 represents the feed horn where some points were identified in order to find the missing dimensions. To simplify the analysis, the assumption is made that the external extension length is equal to the internal extension length. Table A.1 summarises the measured values of the rectangular feed horn. The first dimension to be found is the length of the horn, i.e. the size of the segment EE' (or FF', GG' and HH'). By projection of the waveguide onto the aperture plane, the length of every segment on the aperture plane can be found by simple trigonometry since the waveguide is centred with the horn.
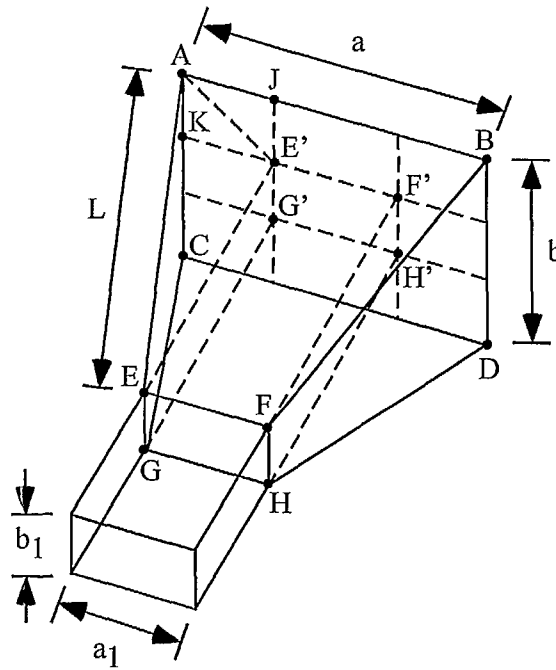
Figure A.1: Decomposition of a feed horn for structural study.

Considering point A and the surrounding points (E', J and K), the length of segment KE' is obtained as follows:

$$\overline{KE'} = \frac{\overline{AB} - \overline{E'F'}}{2}.$$ (A-1)

Similarly, the length of segment JE' is obtained:

$$\overline{JE'} = \frac{\overline{AC} - \overline{E'G'}}{2}.$$ (A-2)

Table A.1: Measured values of rectangular feed horn.

Dimension	Symbol	Segments	Value (mm)
Longest dimension of the aperture	a	AB, CD	35
Smallest dimension of the aperture	b	AC, BD	25
Extension length	L	AE, BF, CG, DH	77
Waveguide longest dimension	a_1	EF, GH (E'F', G'H')	7.112
Waveguide smallest dimension	b_1	EG, FH (E'G', F'H')	3.556

From (A-1) and (A-2), The length of segment AE' can be found with simple trigonometry:

$$\overline{JE'}^2 + \overline{KE'}^2 = \overline{AE'}^2.$$

(A-3)

Furthermore, since the extension length (segment AE) is known, the length of the horn (segment EE') can be found using trigonometry:

$$\overline{AE'}^2 + \overline{EE'}^2 = \overline{AE}^2.$$

(A-4)

Once the length of the horn is known, the apex-to-aperture distance can be found in both E-plane and H-plane. Figure A.2 shows side views of these two planes, in which C corresponds to the length of the horn (segment EE'), H corresponds to the extension height of the horn (segment JE') and W corresponds to the extension width of the horn (segment KE'). From C and H or W, the flare angle in each plane, α_e or α_h, can be found:

$$\tan \alpha_e = \frac{H}{C},$$

(A-5)

$$\tan \alpha_h = \frac{W}{C}.$$

(A-6)

Once the flare angle is known, the apex-to-aperture distance in each plane, p_e and p_h can be found as follow:

$$\tan \alpha_e = \frac{b}{2p_e},$$

(A-7)

$$\tan \alpha_h = \frac{a}{2p_h}.$$

(A-8)

Similarly, the slant length in each plane, ρ_e and ρ_h, can also be found:

$$\sin \alpha_e = \frac{b}{2\rho_e},$$

(A-9)

$$\sin \alpha_h = \frac{a}{2\rho_h}.$$

(A-10)

113
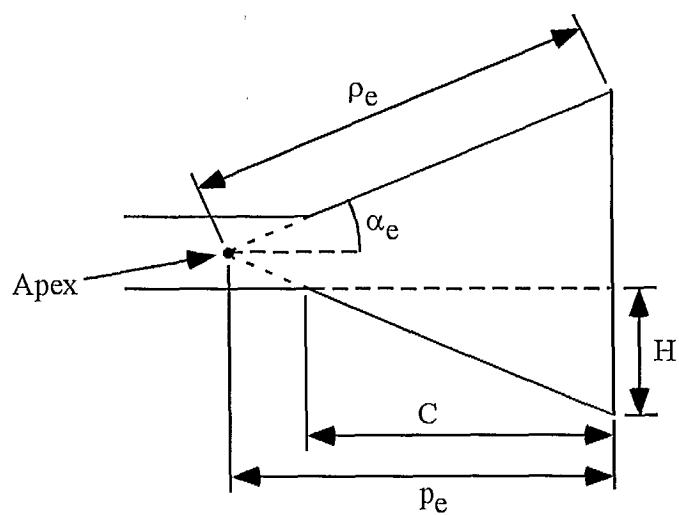
(a)
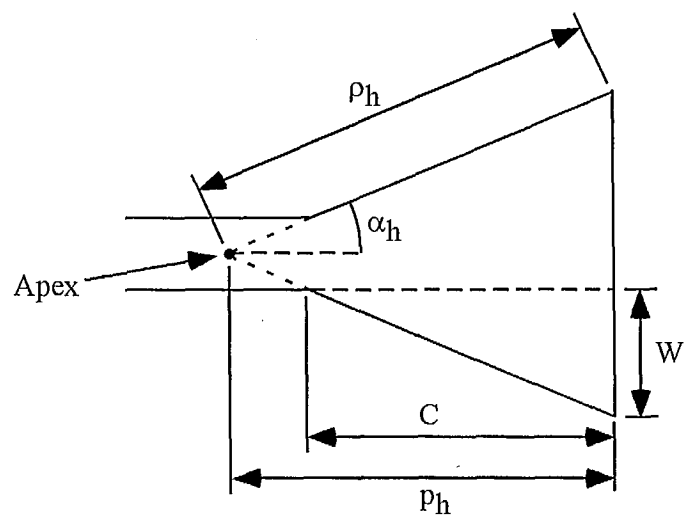
(b)

Figure A.2: Plane view of a horn (a) E-plane; (b) H-plane.

A.3 Calculation

In this section, the calculation of the unknown dimensions of the horn is performed.

From measured values in Table A.1 and using (A-1), the length of segment KE' is

$$W = \overline{KE'} = \frac{35mm - 7.112mm}{2} = 13.944mm. \tag{A-11}$$

Using (A-2), the length of segment JE' is

$$H = \overline{JE'} = \frac{25mm - 3.556mm}{2} = 10.722mm. \tag{A-12}$$

The length of segment AE' is obtained by manipulation of (A-3):

$$\overline{AE'} = \sqrt{\overline{JE'}^2 + \overline{KE'}^2} = \sqrt{(10.722mm)^2 + (13.944mm)^2} = 17.590mm. \tag{A-13}$$

The length of the horn is calculated from (A-4):

$$C = \overline{EE'} = \sqrt{\overline{AE}^2 - \overline{AE'}^2} = \sqrt{(77mm)^2 - (17.59mm)^2} = 74.96mm. \tag{A-14}$$

By manipulating (A-5) and (A-6), the flare angle is obtained in both E-plane and H-plane:

$$\alpha_e = \arctan\left(\frac{H}{C}\right) = \arctan\left(\frac{10.722mm}{74.96mm}\right) = 8.14°, \tag{A-15}$$

$$\alpha_h = \arctan\left(\frac{W}{C}\right) = \arctan\left(\frac{13.944mm}{74.96mm}\right) = 10.54°. \tag{A-16}$$

Using the result of (A-15), (A-7) can be rearranged so that the apex-to-aperture distance in the E-plane is obtained:

$$p_e = \frac{b}{2\tan\alpha_e} = \frac{25mm}{2\tan(8.14°)} = 87.39mm. \tag{A-17}$$

Similarly for the apex-to-aperture distance in the H-plane:

$$p_h = \frac{a}{2\tan\alpha_h} = \frac{35mm}{2\tan(10.54°)} = 94.08mm. \tag{A-18}$$

The slant length of each plane are obtained from (A-9) and (A-10):

$$\rho_e = \frac{b}{2\sin\alpha_e} = \frac{25mm}{2\sin(8.14°)} = 88.28mm, \tag{A-19}$$

$$\rho_h = \frac{a}{2\sin\alpha_h} = \frac{35mm}{2\sin(10.54°)} = 95.69mm. \qquad\qquad \text{(A-20)}$$

Table A.2 summarises the calculated dimensions to be used in the calculation of the beam waist location of the horn.

Table A.2: Calculated dimensions of rectangular feed horn.

Dimension	Symbol	Value (mm)
Apex-to-aperture distance in the E-plane	p_e	87.39
Apex-to-aperture distance in the H-plane	p_h	94.08
Slant length in the E-plane	ρ_e	88.28
Slant length in the H-plane	ρ_h	95.69

APPENDIX B Tivar Lenses

B.1 Introduction

To improve the performance of the measurement system, the Plexiglas lenses were replaced with Tivar 1000 lenses. Tivar 1000 has a dielectric constant lower than Plexiglas, therefore the wave impedance mismatch at the surface of the lens is reduced and the S-parameters are more accurate since the ripples have lower magnitude. This appendix presents the design of these lenses.

B.2 Lens Design

The Tivar 1000 lenses were introduced to replace the existing Plexiglas lenses. Therefore, the new lenses should have similar parameters as the previous lenses, i.e. similar focal length, edge taper and diameter.

The misalignment study performed in Chapter 4 using the original Plexiglas lenses revealed that the input and output beam waist radii had to be corrected. Therefore, in the new design, the corrected value of input beam waist radius was chosen, i.e. a value of 13 mm.

As mentioned in Chapter 3, 98.89% of the power is intercepted if the radius of the sample is 1.5 times larger than the output beam waist radius or 99.97% of the power is intercepted if it is 2 times larger. Knowing that the radius of the sample is 37.5 mm, an output beam radius of about this size is desired, which would give a value between 18.75 mm and 25 mm. In order to intercept a little more power, the focal length was slightly reduced compared to the previous lenses, i.e. a value of 90 mm was chosen compared to

93 mm for the previous design. From (4-10), for an input beam waist radius of 13 mm at 30 GHz, the output beam waist radius is

$$w_{out} \cong \frac{\lambda_0 f}{\pi w_{in}} = \frac{(10mm)(90mm)}{\pi(13mm)} \approx 22mm. \tag{B-1}$$

Knowing the approximate value of the output beam waist radius, the approximate fraction of the power intercepted is given by (2-28):

$$F_e = 1 - \exp\left[-2\left(\frac{r_e}{w}\right)^2\right] = 1 - \exp\left[-2\left(\frac{37.5mm}{22mm}\right)^2\right] = 99.7\%. \tag{B-2}$$

The diameter of the lens is one of the critical parameter. In order to choose it correctly, the beam radius must be known at the input surface of the lens, which is determined using (2-10):

$$w(z = f) = w_0\left[1 + \left(\frac{\lambda_0 f}{\pi w_0^2}\right)^2\right]^{0.5} = 13mm\left[1 + \left(\frac{(10mm)(90mm)}{\pi(13mm)^2}\right)^2\right]^{0.5} = 25.59mm. \tag{B-3}$$

The diameter is then found using (2-27). In this case, an edge taper of 20 dB is chosen, which corresponds to a fractional power of 99%. From (2-27):

$$D = 0.3393(2w)(Te(dB))^{0.5} = 0.3393(2(25.59mm))(20)^{0.5} = 77.65mm. \tag{B-4}$$

The dielectric material used for the lens is Tivar 1000. This material has a dielectric constant of 2.3. A low value of dielectric constant was chosen so that less reflection occurs at the surface of the lens. However, in this case the lens is thicker. Finally, the shape of the lens is hyperbolic and follows (2-29). With the values of f and ε_r known, the equation of the lens dimensions is:

$$x^2 + y^2 = 1.3z^2 + (92.984mm)z. \tag{B-5}$$

Table B.1: Parameters of the Tivar lens.

Parameter	Symbol	Value (mm)
Focal length	f	90.00
Diameter	D	77.65
Thickness	T	13.62
Dielectric constant	ε_r	2.3

The thickness of the lens is found to be 13.62 mm using (2-30). Figure B.1 shows the focusing lens. Table B.1 summarises the parameters of the lens.

B.3 Lens Analysis

As for the Plexiglas lenses, we are interested in knowing the width of the beam intercepted by the lens. The intercepted angle is calculated from Figure 3.3:

$$\theta = \arctan\left(\frac{D/2}{f+T}\right) = \arctan\left(\frac{77.65mm}{2(90.00mm+13.62mm)}\right) = 20.54°. \qquad (B-6)$$

This value is close enough to the the estimated value of 20°, and therefore the beam intercepted by the focusing lens is fairly Gaussian.

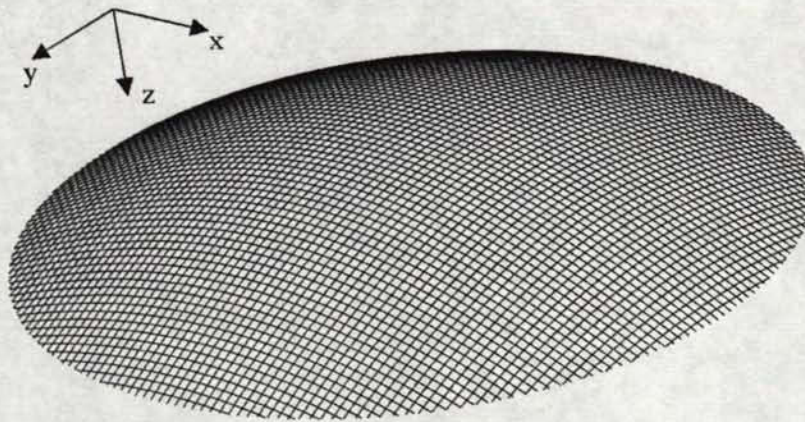**Figure B.1: Representation of the shape of the Tivar lens used in the quasi-optical test bench.**

APPENDIX C Representation of Reflection and Transmission Coefficients of a Dielectric Slab

C.1 Introduction

The goal of this appendix is to provide an alternative approach based on the graphical representation to the problem of reflection and transmission coefficients of a dielectric sample. It may provide a better understanding of the behaviour of the reflection and transmission coefficients of a dielectric slab compared to the mathematical derivations presented in Chapter 5.
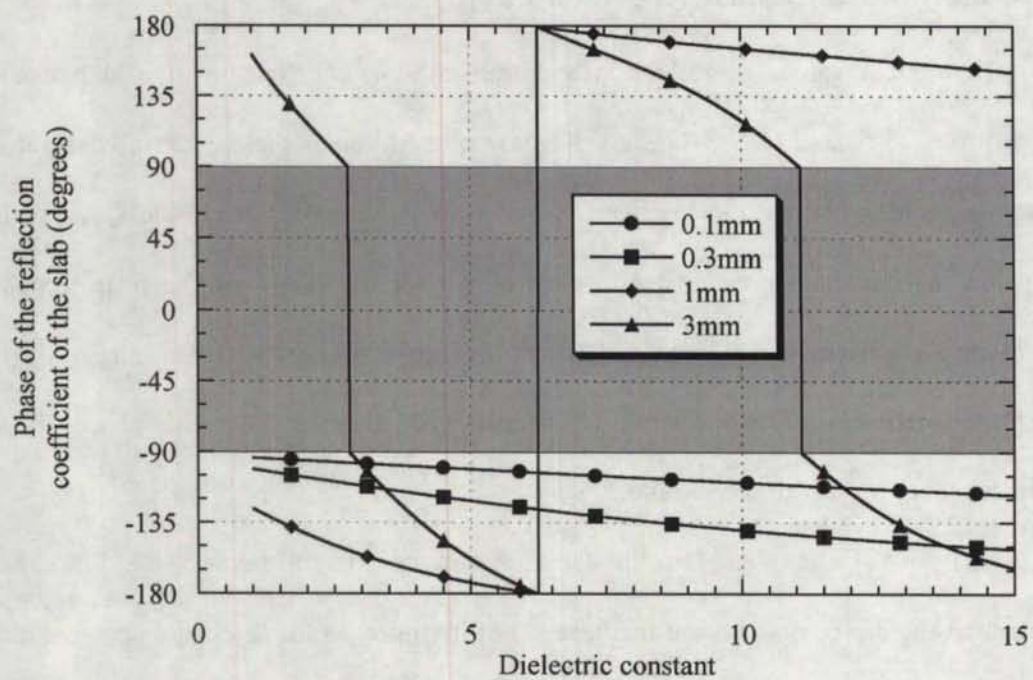
C.2 Magnitude and Phase Representation

Theoretical values of reflection and transmission coefficients of a slab can be obtained from (5-5) and (5-6). These values are plotted versus the dielectric constant for different sample thicknesses in Figures C.1 and C.2. All samples are lossless, i.e. with a real value for the dielectric constant. Comparison of the phase of the reflection and transmission coefficients (Figures C.1(b) and C.2(b)) reveals that the phase of the reflection coefficient of the sample is always ±90° compared to the phase of the transmission coefficient of the sample.

Analysis of the phase of the transmission coefficient reveals that the phase decreases as the dielectric constant increases. Furthermore, as the thickness decreases, the phase tends to zero for the case where the dielectric constant is unity. Similar observations
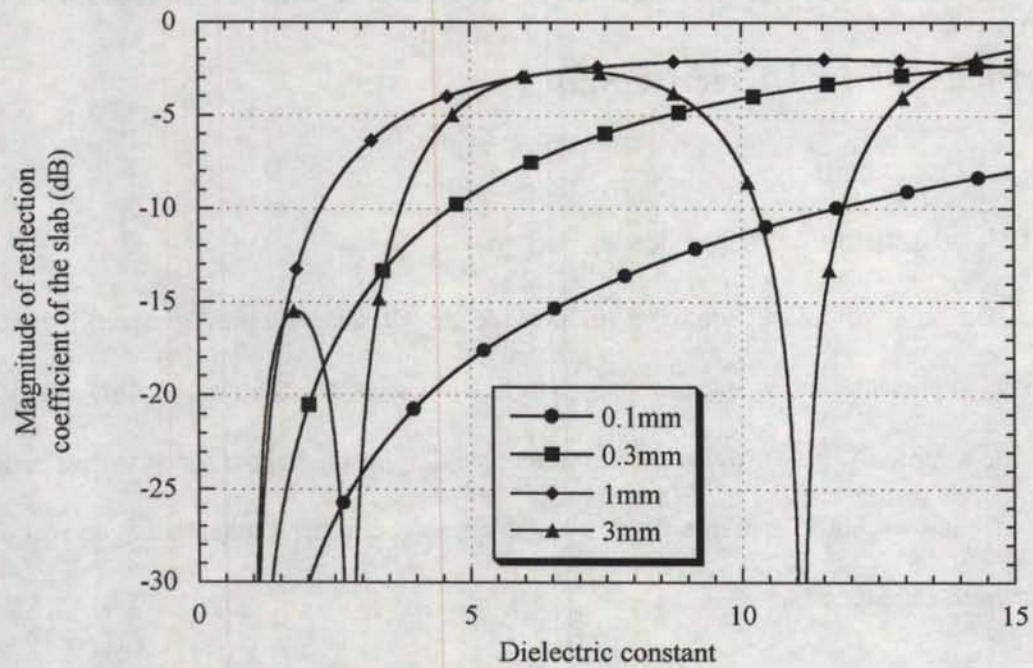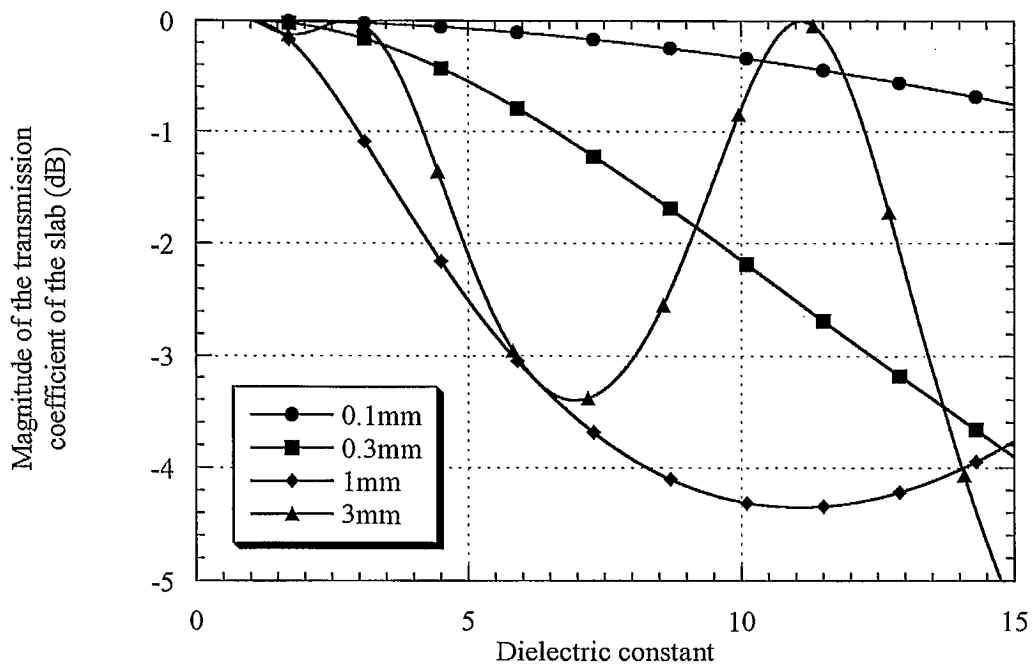
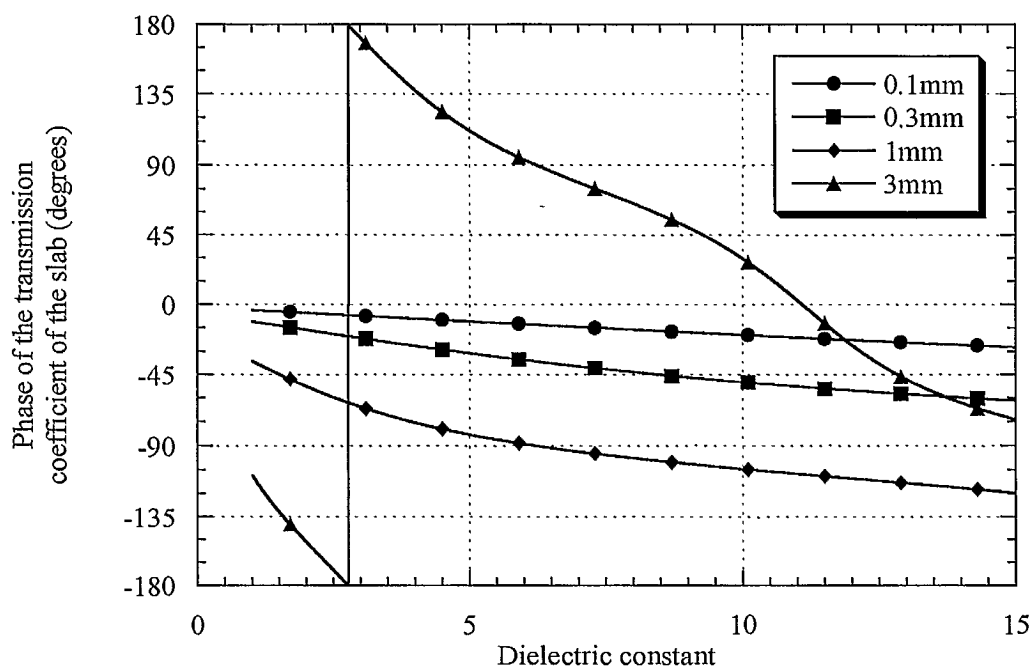Figure C.1: Magnitude and phase of reflection coefficient of the slab vs dielectric constant at 30 GHz.

(a)

(b)

Figure C.2: Magnitude and phase of transmission coefficient of the slab vs dielectric constant at 30 GHz.

can be made for the phase of the reflection coefficient (Figure C.2(b)), however in that case the phase does not tend to zero, but rather to $-90°$. In other words, changing the thickness of a sample of air will lead to different values of phase for both reflection and transmission coefficients of the sample. However, the phase provided by the TRM calibration is valid for infinitely thin samples, therefore we can conclude that the calibration process does not take into account the thickness of the sample.

As found mathematically in Chapter 5, the phase of the reflection coefficient never takes values between $-90°$ and $+90°$. This was also observed in Figure C.1(b), as shown by the grey shading.

C.3 Smith Chart Representation of Lossless Materials

Another way of representing the reflection and transmission coefficients is using a Smith chart. Such a representation gives a better explanation why the phase of the reflection coefficient never takes values between $-90°$ and $+90°$. Reflection and transmission coefficients obtained with the sample thicknesses presented in Figures C.1 and C.2 are shown in Figures C.3 to C.6 using a Smith chart: Figure C.3 presents results for a sample thickness of 0.1 mm; Figure C.4 presents results for a sample thickness of 0.3 mm; Figure C.5 presents results for a sample thickness of 1 mm and; Figure C.6 presents results for a sample thickness of 3 mm. It is found that the reflection coefficient is constrained within the left side of the imaginary axis, which corresponds to angle values from $+90°$ to $+270°$ (or $-90°$). This is true for any dielectric material, even if lossy.

Figure C.3: Reflection and transmission coefficients of a 0.1-mm sample vs dielectric constant at 30 GHz.

Figure C.4: Reflection and transmission coefficients of a 0.3-mm sample vs dielectric constant at 30 GHz.
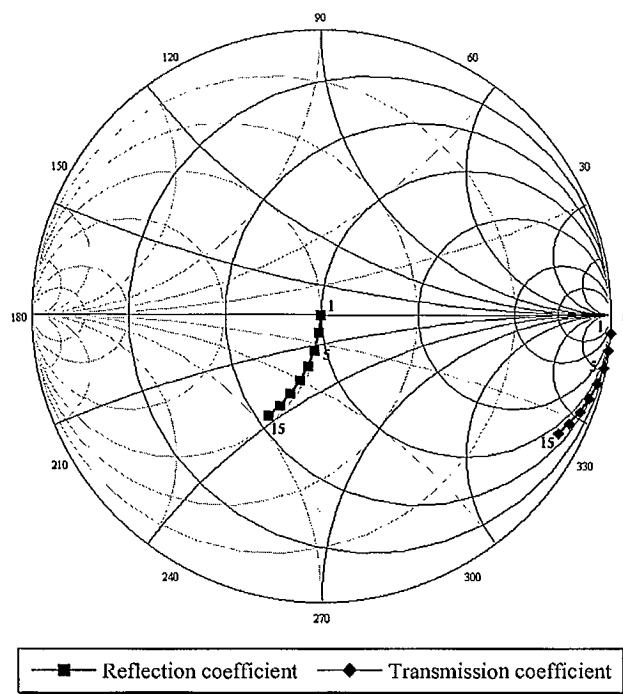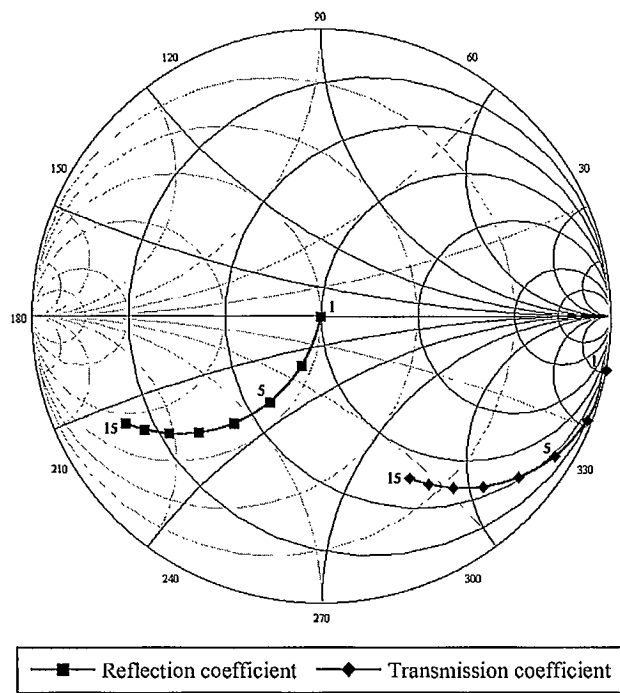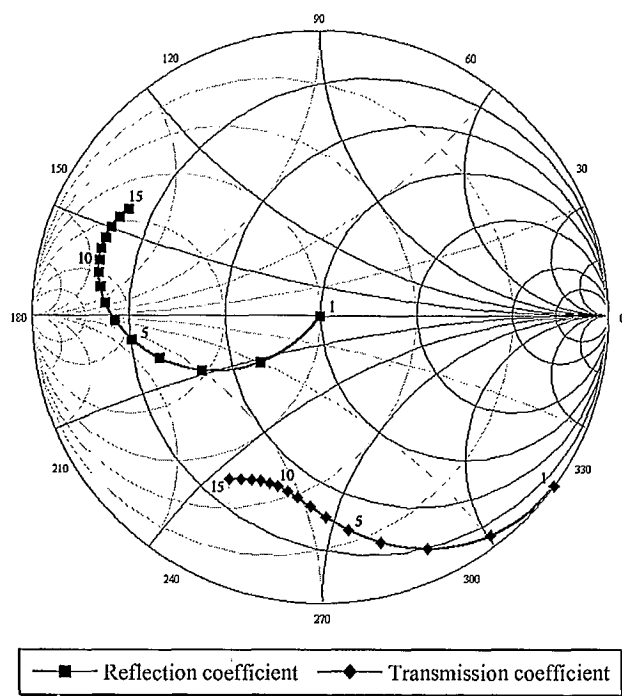
Figure C.5: Reflection and transmission coefficients of a 1-mm sample vs dielectric constant at 30 GHz.
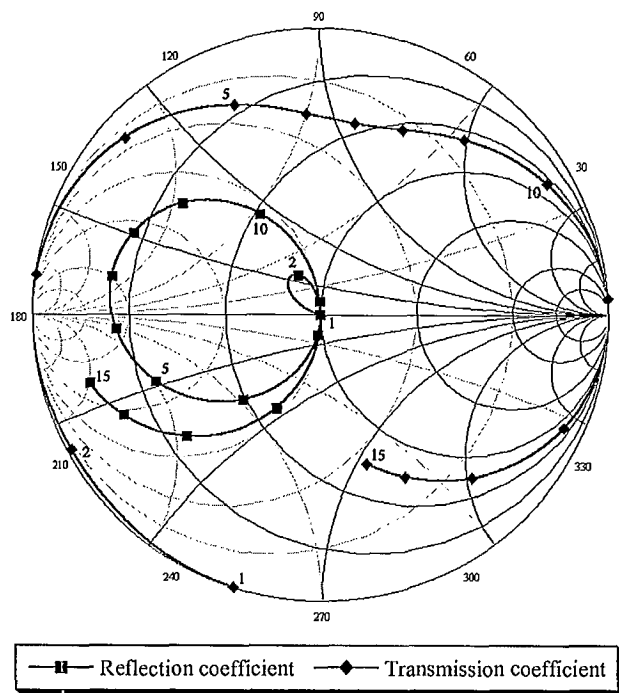

Figure C.6: Reflection and transmission coefficients of a 3-mm sample vs dielectric constant at 30 GHz.

126

Moreover, the reflection coefficient is constrained within the circle of normalised conductance equal to 1, and the transmission coefficient lies outside the circle of normalised conductance equal to 1 and the circle of normalised resistance equal to 1. This is true for lossless dielectric materials. This observation is even more evident if the range of dielectric constant values is extended.

Figure C.7 presents results for an extended range of dielectric constant values. This helps to understand the correlation between the magnitude and phase. For the reflection coefficient, angle values close to $\pm 90°$ corresponds to a low magnitude. On the Smith chart, it corresponds to the centre point, where the phase shifts since the slope of the curve tends to infinity. Furthermore, angles close to $180°$ corresponds to high values of magnitude of reflection coefficient. Similarly, for the transmission coefficient, when the phase is close to $\pm 90°$ the magnitude is low and when the phase reaches $0°$ or $180°$ the magnitude is high.

C.4 Smith Chart Representation of Lossy Materials

With the observations made in the previous section, it would be interesting to examine the behaviour of lossy materials. Figures C.7 to C.10 present the results for different values of loss tangent: Figure C.7 shows results for a lossless sample; Figure C.8 shows results for a loss tangent of 0.001; Figure C.9 shows results for a loss tangent of 0.01 and; Figure C.10 shows results for a loss tangent of 0.1. It is found that, as the loss tangent increases, the magnitude of the reflection coefficient increases and its angle tends to take values around $180°$. On the other hand, the transmission coefficient becomes no

127
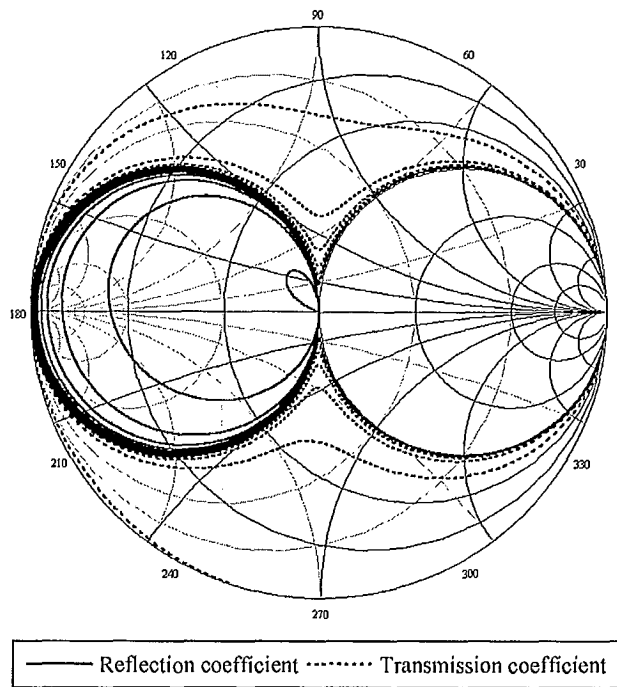
Figure C.7: Reflection and transmission coefficients of a lossless 3-mm sample vs dielectric constant from 1 to 600 at 30 GHz.
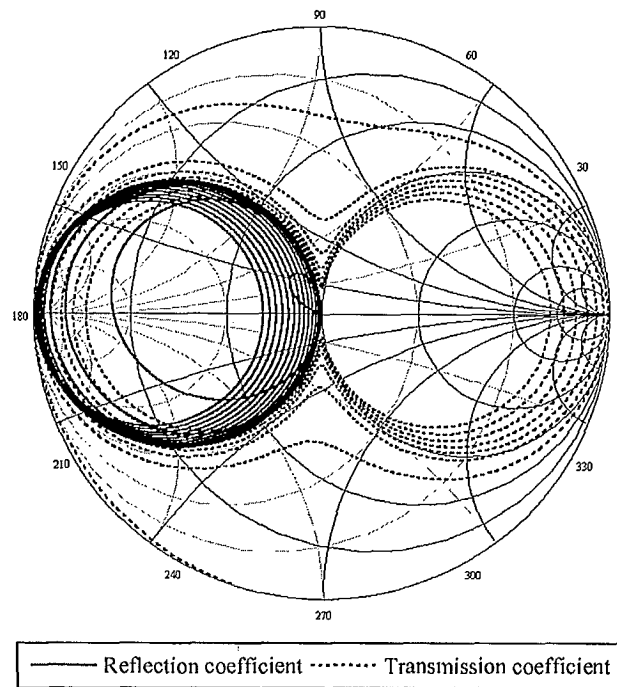
Figure C.8: Reflection and transmission coefficients of a 3-mm sample with loss tangent 0.001 vs dielectric constant from 1 to 600 at 30 GHz.

128
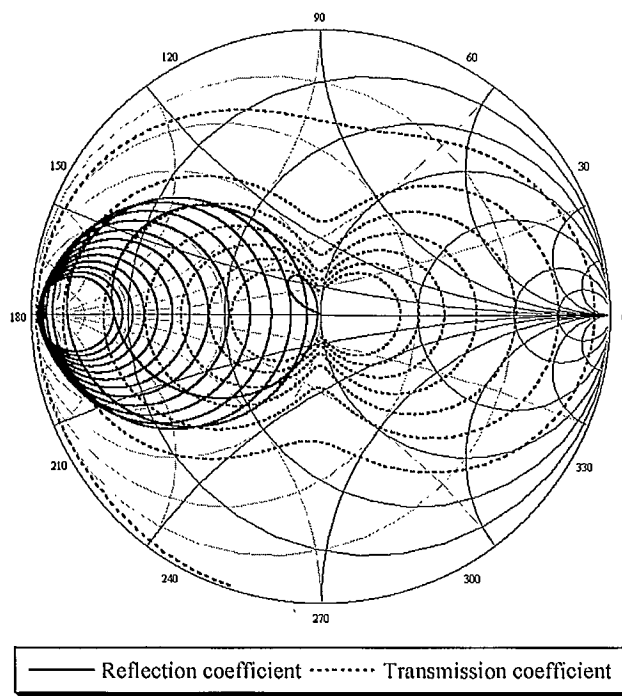
Figure C.9: Reflection and transmission coefficients of a 3-mm sample with loss tangent 0.01 vs dielectric constant from 1 to 600 at 30 GHz.
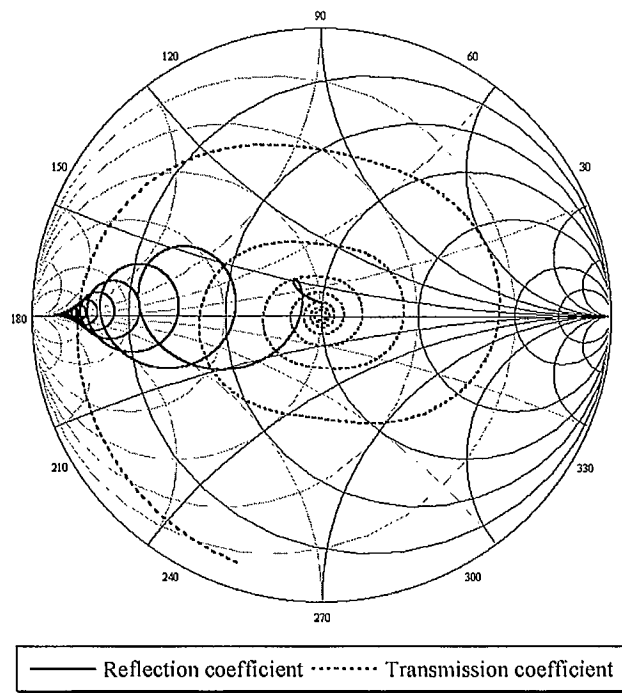
Figure C.10: Reflection and transmission coefficients of a 3-mm sample with loss tangent 0.1 vs dielectric constant from 1 to 600 at 30 GHz.

longer constrained outside the circle of normalised conductance equal to 1 and the circle of normalised resistance equal to 1, but there is still a forbidden region similar to the shape of the two circles. However, this region tends to becomes smaller as the dielectric constant or loss tangent increase. For extremely high values of loss tangent, the material looks more like a conductive material rather than a dielectric material, and the transmission coefficient lies in the centre point of the Smith chart, whereas the reflection coefficient tends to left-end side of the Smith chart (magnitude of 1 with phase of 180°).

Finally, it is important to mention that the phase difference between the reflection and transmission coefficients will no longer be ±90° for lossy materials. It is found that the phase difference becomes more different from ±90° as the loss tangent increases.

APPENDIX D Derivation of Reflection and Transmission Coefficients of the Air-Sample Interface from the Reflection and Transmission Coefficients of the Slab

D.1 Introduction

This appendix presents the derivation of the air-slab interface parameters from the slab parameters, which are used to analytically find the dielectric constant.

D.2 Reflection Coefficient Derivation

The equations of the reflection and transmission coefficients of the slab, respectively Γ_S and T_S, as a function of the reflection and transmission coefficients at the air-slab interface, respectively Γ and τ, are given in Chapter 5:

$$\Gamma_S = \frac{\Gamma\left(1 - \tau^2\right)}{1 - \Gamma^2 \tau^2} \, , \tag{D-1}$$

$$T_S = \frac{\tau\left(1 - \Gamma^2\right)}{1 - \Gamma^2 \tau^2} \, . \tag{D-2}$$

The goal is to obtain equations for Γ and τ as a function of Γ_S and T_S. Isolating τ^2 in (D-1):

$$\Gamma_S\left(1 - \Gamma^2 \tau^2\right) = \Gamma\left(1 - \tau^2\right),$$

$$\Gamma_S - \Gamma_S \Gamma^2 \tau^2 = \Gamma - \Gamma \tau^2,$$

$$\Gamma_S - \Gamma = \left(\Gamma_S \Gamma^2 - \Gamma\right)\tau^2,$$

$$\tau^2 = \frac{\Gamma_S - \Gamma}{\Gamma\left(\Gamma_S \Gamma - 1\right)}. \tag{D-3}$$

The square root of (D-3) gives a solution for τ:

$$\tau = \sqrt{\frac{\Gamma - \Gamma_S}{\Gamma - \Gamma_S \Gamma^2}} \; . \tag{D-4}$$

Substituting (D-4) in (D-2):

$$T_S = \frac{\sqrt{\dfrac{\Gamma - \Gamma_S}{\Gamma - \Gamma_S \Gamma^2}}\left(1 - \Gamma^2\right)}{1 - \Gamma^2 \left(\sqrt{\dfrac{\Gamma - \Gamma_S}{\Gamma - \Gamma_S \Gamma^2}}\right)^2} \; . \tag{D-5}$$

Simplifying (D-5):

$$T_S = \frac{\sqrt{\dfrac{\Gamma - \Gamma_S}{\Gamma - \Gamma_S \Gamma^2}}\left(1 - \Gamma^2\right)}{1 - \Gamma^2 \dfrac{\Gamma - \Gamma_S}{\Gamma - \Gamma_S \Gamma^2}} \; ,$$

$$T_S = \frac{\sqrt{\dfrac{\Gamma - \Gamma_S}{\Gamma(1 - \Gamma_S \Gamma)}}\left(1 - \Gamma^2\right)\left(1 - \Gamma_S \Gamma\right)}{1 - \Gamma_S \Gamma - \Gamma^2 + \Gamma_S \Gamma} \; ,$$

$$T_S = \sqrt{\frac{\Gamma - \Gamma_S}{\Gamma(1 - \Gamma_S \Gamma)}}\left(1 - \Gamma_S \Gamma\right),$$

$$T_S{}^2 = \frac{\Gamma - \Gamma_S}{\Gamma(1 - \Gamma_S \Gamma)}\left(1 - \Gamma_S \Gamma\right)^2,$$

$$Ts^2 = \frac{(\Gamma - \Gamma_S)(1 - \Gamma_S \Gamma)}{\Gamma} \; ,$$

$$\Gamma T_S{}^2 = \Gamma - \Gamma^2 \Gamma_S - \Gamma_S + \Gamma \Gamma_S{}^2 \; ,$$

$$\Gamma^2 \Gamma_S - \Gamma\left(\Gamma_S{}^2 - T_S{}^2 + 1\right) + \Gamma_S = 0 \; ,$$

$$\Gamma^2 - 2\Gamma\left(\frac{\Gamma_S - T_S + 1}{2\Gamma_S}\right) + 1 = 0 \; , \tag{D-6}$$

in which a new variable is substituted as follow:

$$\kappa = \frac{\Gamma_s{}^2 - T_s{}^2 + 1}{2\Gamma_s}. \tag{D-7}$$

Equation (D-6) can then be simplified:

$$\Gamma^2 - 2\Gamma\kappa + 1 = 0. \tag{D-8}$$

Equation (D-8) is a quadratic equation, therefore solving for Γ leads to the following result:

$$\Gamma = \frac{2\kappa \pm \sqrt{4\kappa^2 - 4}}{2},$$

$$\Gamma = \kappa \pm \sqrt{\kappa^2 - 1}. \tag{D-9}$$

Equation (D-9) is the same equation as the one obtained in [19]. There are two possible solutions, however there will always be a solution of magnitude greater than unity, which has to be rejected.

D.3 Transmission Coefficient Derivation

The transmission coefficient τ can be derived using the same procedure as for the reflection coefficient, however this method provides two solutions and there is no easy way to determine which solution is the valid one. Therefore, another approach is used, in which τ is isolated using (D-1) and (D-2). First, τ^2 is obtained in (D-3). However applying the square root will provide two solutions, which does not solve the problem. Therefore, (D-2) is used instead of (D-1), in which τ is isolated:

$$\tau = \frac{T_s\left(1 - \Gamma^2\tau^2\right)}{1 - \Gamma^2}. \tag{D-10}$$

Then, (D-3) is substituted in (D-10):

$$\tau = \frac{T_s\left(1-\Gamma^2\,\dfrac{\Gamma_s-\Gamma}{\Gamma(\Gamma_s\Gamma-1)}\right)}{1-\Gamma^2},$$

$$\tau = \frac{T_s\left(1-\dfrac{\Gamma_s\Gamma-\Gamma^2}{\Gamma_s\Gamma-1}\right)}{1-\Gamma^2},$$

$$\tau = \frac{T_s\left[(\Gamma_s\Gamma-1)-(\Gamma_s\Gamma-\Gamma^2)\right]}{(1-\Gamma^2)(\Gamma_s\Gamma-1)},$$

$$\tau = \frac{T_s(\Gamma^2-1)}{(1-\Gamma^2)(\Gamma_s\Gamma-1)},$$

$$\tau = \frac{T_s}{1-\Gamma_s\Gamma}. \tag{D-11}$$

This value of τ provides no ambiguity since only one solution is possible.

APPENDIX E Conversion from Surface Resistivity to Loss Tangent for n-Type and p-Type Silicon

E.1 Introduction

This appendix provides guidelines to perform conversion from surface resistivity to loss tangent for both n-type and p-type silicon.

E.2 Resistivity and Dopant Density

In converting between surface resistivity and loss tangent, the first conversion to be performed is between resistivity and dopant density, N. In this case, we assume that n-type silicon is doped with phosphorus and p-type silicon is doped with boron. This conversion can easily be performed from ASTM Standard F 723-97 curves, tables or equations [43]. Typical curves are presented in Figure E.1.

E.3 Dopant Density and Complex Permittivity

The Debye model for dielectric constant is generally defined for photoinduced holes and electrons [44]. However, in this particular case, we are only interested by the intrinsic permittivity. For n-type silicon,

$$\varepsilon_r = \varepsilon_p - \frac{Nq^2\tau_e^2}{m_e\varepsilon_0\left(1+\omega^2\tau_e^2\right)}\left(1+j\frac{1}{\omega\tau_e}\right),\qquad \text{(E-1)}$$

where

$$\tau_e = \frac{\mu_e m_e}{q}. \tag{E-2}$$

Similarly for p-type silicon:

$$\varepsilon_r = \varepsilon_p - \frac{Nq^2 \tau_p^{\ 2}}{m_p \varepsilon_0 \left(1 + \omega^2 \tau_p^{\ 2}\right)} \left(1 + j \frac{1}{\omega \tau_p}\right), \tag{E-3}$$

where

$$\tau_h = \frac{\mu_h m_p}{q}. \tag{E-4}$$

The loss tangent is then obtained from the complex relative permittivity ε_r. Constant values used in this calculation can be found in Appendix F.
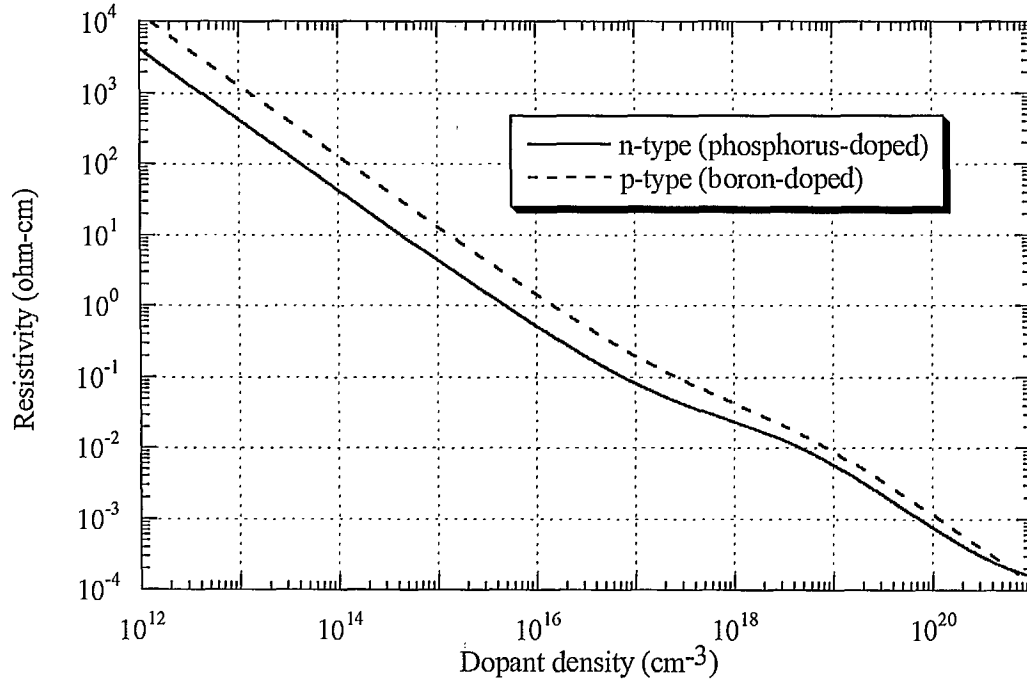
Figure E.1: Conversion between resistivity and dopant density (curves generated from equations in [43]).

E.4 Conclusion

It is observed that the complex relative permittivity, and consequently the loss tangent, vary with frequency. Therefore, the loss tangent will not be the same depending on the frequency, as was observed in Chapter 5. Furthermore, the dielectric constant, or the real part of the relative permittivity, can also vary with frequency, but for high-resistivity silicon at microwave frequencies, the variation is insignificant.
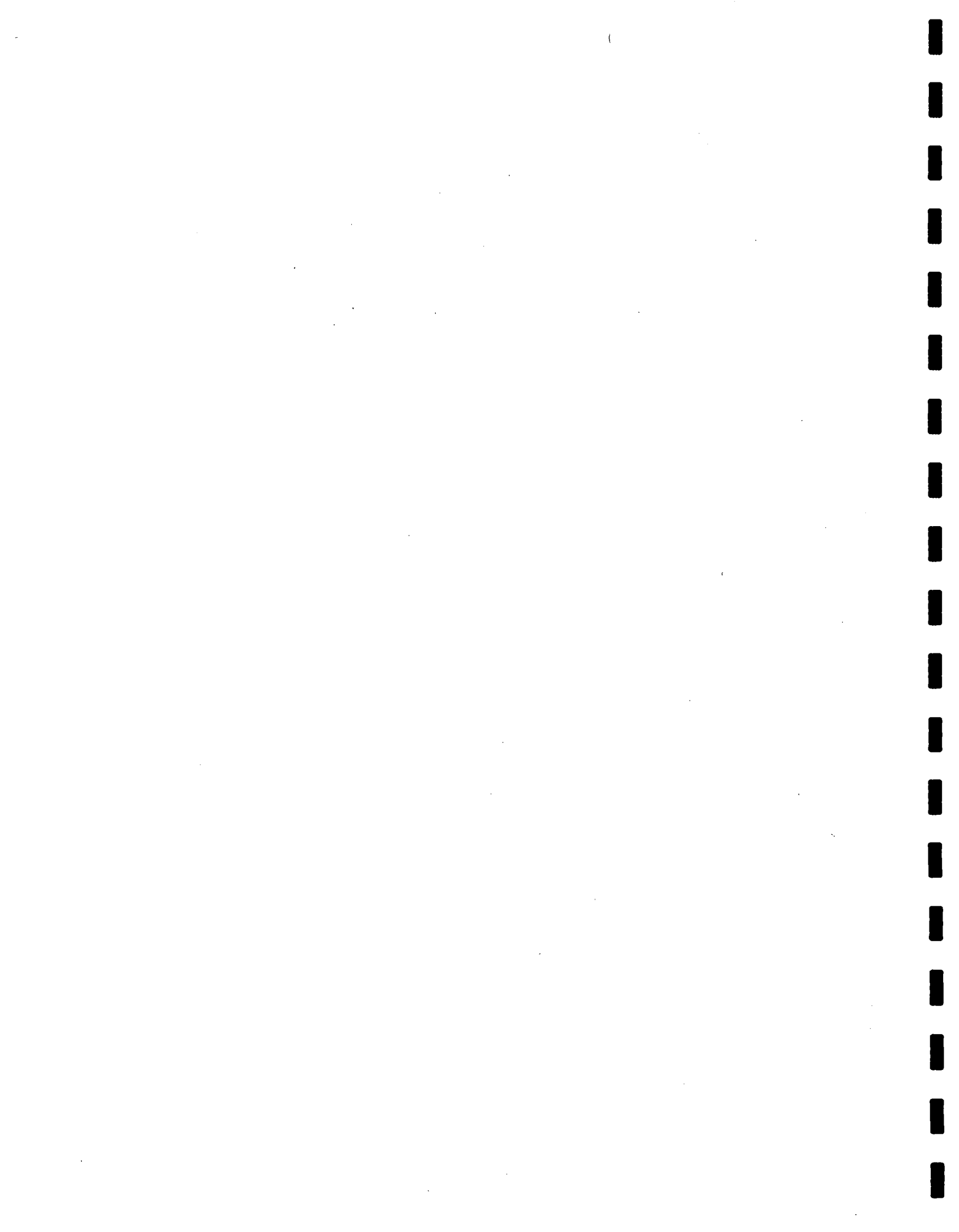
APPENDIX F Physical Constants

F.1 Free-Space Constants

Table F.1: Free-space constants.

Constant	Symbol	Value
Permittivity	ε_0	8.854×10^{-12} F/m
Permeability	μ_0	1.257×10^{-6} H/m

F.2 Physical Constants of Electrons

Table F.2: Physical constants of electrons and holes.

Constant	Symbol	Value
Free-electron mass	m_0	9.109×10^{-31} kg
Electronic charge	q	1.602×10^{-19} C

F.3 Silicon Parameters

Table F.3: Silicon parameters.

Parameter	Symbol	Value
Unperturbed relative permittivity	ε_p	11.7
Electron mass	m_e	$0.259m_0$
Hole mass	m_p	$0.38m_0$
Electron mobility	μ_e	1500 cm^2/(V·s)
Hole mobility	μ_h	600 cm^2/(V·s)

REFERENCES

[1]   R. J. Douville, "RF Technology for Broadband Ka-Band Communication Systems," in *Proc. 2nd Can. Conf. Broadband Research (CCBR)*, Ottawa, Ontario, pp. 1-11, June 1998.

[2]   G. Heftman, "LMDS Set to Challenge for Last-Mile Supremacy," *Microwave and RF*, vol. 38, no. 4, pp. 30-38, April 1999.

[3]   S. Y. Seidel and H. W. Arnold, "28 GHz Multipoint Distribution Service (LMDS): Strengths and Chalenges", in *Wireless Personal Communications: The Evolution of Personal Communications Systems*, T. S. Rappaport, B. D. Woerner and J. H. Reed, Eds., Kluwer, Boston, MA, 1996, pp. 7-17.

[4]   J. V. Evans, "Communication Satellite Systems for High-Speed Internet Access," *IEEE Antennas Propagat. Mag.*, vol. 43, no. 5, pp. 11-22, October 2001.

[5]   M. L. VanBlaricum, "Photonic Antenna Reconfiguration: A Status Survey," in *Proc. SPIE, Photonics and Radio Frequency II*, vol. 3463, San Diego, CA, pp. 180-189, July 1998.

[6]   G. F. Brand, "Remote Millimeter-Wave Beam Control by the Illumination of a Semiconductor," *IEEE Trans. Microwave Theory Tech.*, vol. 48, no. 5, pp. 855-857, May 2000.

[7]   V. A. Manasson, L. S. Sadovnik, P. I. Shnitser, R. Mino and J. S. Kruger, "Millimeter-Wave Optically Scanning Antenna Based on Photoinduced Plasma Grating," *Opt. Eng.*, vol. 35, no. 2, pp. 357-361, February 1996.

[8]   P. F. Goldsmith, *Quasioptical Systems*, IEEE Press, New York, 1998.

[9]   P. F. Goldsmith, "Quasi-Optical Techniques," *Proc. IEEE*, vol. 80, no. 11, pp. 1729-1747, November 1992.

[10] P. F. Goldsmith, T. Itoh and K. D. Stephan, "Quasi-Optical Techniques", Chapter 7 in *Handbook of Microwave and Optical Components*, vol. 1, K. Chang, Ed., Wiley, New York, 1989.

[11] D. K. Cheng, *Fundamentals of Engineering Electromagnetics*, Addison-Wesley, Reading, MA, 1993.

[12] G. P. Agrawal and M. Lax, "Free-space Wave Propagation Beyond the Paraxial Approximation," *Phys. Rev. A*, vol. 27, no. 3, pp. 1693-1695, March 1983.

[13] J. Tuovinen, "Accuracy of a Gaussian Beam," *IEEE Trans. Antennas Propagat.*, vol. 40, no. 4, pp. 391-398, April 1992.

[14] D. H. Martin and J. W. Bowen, "Long-Wave Optics," *IEEE Trans. Microwave Theory Tech.*, vol. 41, no. 10, pp. 1676-1690, October 1993.

[15] J. Tuovinen, T. M. Hirvonen and A. V. Räisänen, "Near-Field Analysis of a Thick Lens and Horn Combination: Theory and Measurements," *IEEE Trans. Antennas Propagat.*, vol. 40, no. 6, pp. 613-619, June 1992.

[16] G. D. M. Peeler, "Lens Antennas", Chapter 16 in *Antenna Engineering Handbook*, 2nd ed., R.C. Johnson and H. Jasik, Eds., McGraw-Hill, New York, 1984.

[17] D. K. Ghodgaonkar, V. V. Varadan and V. K. Varadan, "A Free-Space Method for Measurement of Dielectric Constants and Loss Tangents at Microwave Frequencies," *IEEE Trans. Instrum. Meas.*, vol. 37, no. 3, pp. 789-793, June 1989.

[18] D. R. Gagnon, "Highly Sensitive Measurements with a Lens-Focused Reflectometer," *IEEE Trans. Microwave Theory Tech.*, vol. 39, no. 12, pp. 2237-2240, December 1991.

[19] D. K. Ghodgaonkar, V. V. Varadan, and V. K. Varadan, "Free-Space Measurement of Complex Permittivity and Complex Permeability of Magnetic Materials at Microwave Frequencies," *IEEE Trans. Instrum. Meas.*, vol. 39, no. 2, pp. 387-394, April 1990.

[20] J. L. Le Bras, M. Le Goff, B. Deschamps, A. Péden, D. Bourreau and S. Toutain, "Quasi-Optical Circuit Measurement Method in W band," in *Proc. ESA Workshop Millimetre Wave Tech. and Applicat.*, Espoo, Finland, pp. 453-457, May 1998.

[21] J. Baker-Jarvis, R. G. Geyer, J. H. Grosvenor Jr., M. D. Janezic, C. A. Jones, B. Riddle, C. M. Weil and J. Krupka, "Dielectric Characterization of Low-Loss Materials: A Comparison of Techniques," *IEEE Trans. Dielect. Elec. Insulation*, vol. 5, no. 4, pp. 571-577, August 1998.

[22] G. R. Traut, "Electric Performance of Microwave Boards," *IEEE Trans. Comp., Packag., Manufact. Technol. B*, vol. 18, no. 1, pp.106-111, February 1995.

[23] Hewlett-Packard, *Material Measurement Basics*, Note 5091-3300E, July 1999.

[24] M. Le Goff, J. L. Le Bras, B. Deschamps, D. Rozuel, D. Bourreau and A. Péden, "Ka Band Quasi Optical Test Bench Using Focusing Horns," in *Proc. 29th Europ. Microwave Conf. (EuMC)*, Munich, Germany, vol. 2, pp. 240-243, October 1999.

[25] M. Le Goff, J. L. Le Bras, B. Deschamps, D. Bourreau, A. Péden and S. Toutain, "Focusing Horn Design for Wide Band Quasi Optical Circuit Measurements Without Time-Gating," in *Proc. ESA Workshop Millimetre Wave Tech. and Applicat.*, Espoo, Finland, May 1998.

[26] A. Davidson, E. Strid and K. Jones, "Achieving Greater On-Wafer S-Parameter Accuracy with the LRM Calibration Technique," in *34th Automat. RF Tech. Group Conf. Dig. (ARFTG)*, Ft. Lauderdale, FL, pp. 61-66, December 1989.

[27] Hewlett-Packard, *Applying the HP 8510 TRL Calibration for Non-Coaxial Measurements*, Product Note 8510-8A, October 1987.

[28] H. Heuermann and B. Schiek, "Robust Algorithms for Txx Network Analyzer Self-Calibration Procedures," *IEEE Trans. Instrum. Meas.*, vol. 43, no. 1, pp. 18-23, February 1994.

[29]   Agilent, *In-Fixture Measurements Using Vector Network Analyzers*, Application Note 1287-9, August 2000.

[30]   Anritsu, *Model 371XXA Vector Network Analyzer Operation Manual*, Product Note 10900-00327, February 2001.

[31]   N. Gagnon, J. Shaker, P. Berini and L. Roy, "Study of Gaussian Beam Misalignments in Quasi-Optical Test Bench," in *Proc. 8th Int. Symp. Microwave Opt. Tech. (ISMOT)*, Montréal, Canada, pp. 447-450, June 2001.

[32]   H. Kogelnik, "Coupling and Conversion Coefficients for Optical Modes," in *Proc. Symp. Quasi-Optics*, Polytechnic Institute of Brooklyn, New York, pp. 333-347, 1964.

[33]   W. B. Joyce and B. C. DeLoach, "Alignment of Gaussian Beams," *Applied Optics*, vol. 23, no. 23, pp. 4187-4196, December 1984.

[34]   Mathsoft, *Mathcad 2001 Professional User's Guide with Reference Manual*, Cambridge, MA, November 2000.

[35]   B. Scannell, C. Nightingale, G. O'Connors and A. Philpott, "Gaussian Beam and Radiation Pattern Measurement of a Quasi-optical Radiometer," in *Proc. 6th Int. Conf. Antennas Propagat.*, Coventry, U.K., pp. 383-389, April 1989.

[36]   N. Gagnon, J. Shaker, P. Berini, L. Roy and A. Petosa, "Material Characterization Using a Quasi-Optical Measurement System," in *Conf. Prec. Electromagn. Meas. Dig. (CPEM)*, Ottawa, Canada, pp. 104-105, June 2002.

[37]   P. Berini, "Wave transmission Media," ELG 4103 Course Notes, University of Ottawa, 1996.

[38]   J. Baker-Jarvis, E. J. Vanzura and W. A. Kissick, "Improved Technique for Determining Complex Permittivity with the Transmission/Reflection Method," *IEEE Trans. Microwave Theory Tech.*, vol. 38, no. 8, pp. 1096-1103, August 1990.

[39] G. Hayes, "Genetic Algorithms," CRC Report no. CRC-RP-2000-12, Communications Research Centre Canada, Ottawa, Ontario, 2000.

[40] R. L. Haupt, "An Introduction to Genetic Algorithms for Electromagnetics," *IEEE Antennas Propagat. Mag.*, vol. 37, no. 2, pp. 7-15, April 1995.

[41] J. M. Johnson and Y. Rahmat-Samii, "Genetic Algorithms in Engineering Electromagnetics," *IEEE Antennas Propagat. Mag.*, vol. 39, no. 4, pp. 7-21, August 1997.

[42] J. Baker-Jarvis, R. G. Geyer and P. D. Domich, "A Nonlinear Least-Square Solution with Causality Constraints Applied to Transmission Line Permittivity and Permeability Determination," *IEEE Trans. Instrum. Meas.*, vol. 41, no. 5, pp. 646-652, October 1992.

[43] American Society for Testing and Materials, *Standard Practice for Conversion Between Resistivity and Dopant Density for Boron-Doped, Phosphorus-doped and Arsenic-Doped Silicon*, ASTM Standard F 723-97, 1997.

[44] C. H. Lee, O. S. Mak and A. P. DeFonzo, "Optical Control of Millimeter-Wave Propagation in Dielectric Waveguides," *IEEE J. Quantum Electron.*, vol. 16, no. 3, pp. 277-288, March 1980.